SINGLE-IMAGE BAYESIAN RESTORATION AND MULTI-IMAGE SUPER-RESOLUTION RESTORATION FOR B-MODE ULTRASOUND IMAGES USING AN ACCURATE SYSTEM MODEL

A THESIS SUBMITTED TO

THE GRADUATE SCHOOL OF INFORMATICS OF

MIDDLE EAST TECHNICAL UNIVERSITY

BY

MİNE CÜNEYİTOĞLU ÖZKUL

IN PARTIAL FULFILLMENT OF THE REQUIREMENTS FOR THE DEGREE OF

DOCTOR OF PHILOSOPHY

IN

MEDICAL INFORMATICS

JULY 2019

Approval of the thesis:

SINGLE-IMAGE BAYESIAN RESTORATION AND MULTI-IMAGE SUPER-RESOLUTION RESTORATION FOR B-MODE ULTRASOUND IMAGES USING AN ACCURATE SYSTEM MODEL

Submitted by MİNE CÜNEYİTOĞLU ÖZKUL in partial fulfillment of the requirements for the degree of **Doctor of Philosophy in Health Informatics Department, Middle East Technical University** by,

Prof. Dr. Deniz Zeyrek Bozşahin
Dean, **Graduate School of Informatics**   ————————————

Assoc. Prof. Dr. Yeşim Aydın Son
Head of Department, **Health Informatics, METU**   ————————————

Prof. Dr. Ünal Erkan Mumcuoğlu
Supervisor, **Health Informatics, METU**   ————————————

Examining Committee Members:

Prof. Dr. İbrahim Tanzer Sancak
Radiology Dept., TOBB-ETÜ   ————————————

Prof. Dr. Ünal Erkan Mumcuoğlu
Medical Informatics, METU   ————————————

Assist. Prof. Dr. Aybar Can Acar
Medical Informatics, METU   ————————————

Assist. Prof. Dr. Görkem Saygılı
Biomedical Engineering Dept., Ankara University   ————————————

Assoc. Prof. Dr. Yeşim Aydın Son
Medical Informatics, METU   ————————————

                                        Date: _24.07.2019_

I hereby declare that all information in this document has been obtained and presented in accordance with academic rules and ethical conduct. I also declare that, as required by these rules and conduct, I have fully cited and referenced all material and results that are not original to this work.

Name, Last name :   Mine Cüneyitoğlu Özkul

Signature   :   _____

ABSTRACT

SINGLE-IMAGE BAYESIAN RESTORATION AND MULTI-IMAGE SUPER-RESOLUTION RESTORATION FOR B-MODE ULTRASOUND IMAGES USING AN ACCURATE SYSTEM MODEL

Cüneyitoğlu Özkul, Mine

Ph.D, Department of Health Informatics

Supervisor: Prof. Dr. Ünal Erkan Mumcuoğlu

24.07.2019, 100 pages

Medical imaging is an essential part of diagnosis and intervention/surgery planning in modern medicine. Compared to other medical imaging modalities, ultrasound provides a variety of diagnostic advantages. The imaging equipment is less expensive and more portable. There is no known harm to human tissue, therefore, it is applicable in almost any medical field safely. However, ultrasound image quality is usually poorer compared to other modalities. If the image quality of medical ultrasound is improved, it will be beneficial for clinical usage. This makes the research on this subject an increasingly important field, both academically and commercially. In this thesis, image quality improvement was aimed. Both single and multi-frame, in-plane, freehand, 2D, B-mode ultrasound scan data was used for this purpose. Non-rigid image registration, Bayesian image restoration and super-resolution methods, along with a detailed study on statistical modelling of the speckle was employed. Tissue-mimicking resolution phantoms were used to characterize the clinical imaging system. The methods were then tested on a tissue-mimicking breast phantom and on various superficial tissue images collected from volunteers. The methods developed were compared to the well-known image restoration and filtering methods in the literature. Relevant objective image quality evaluation metrics were used to measure overall improvements. Additionally, expert opinions were obtained and evaluated using visual grading analysis. The proposed methods have the drawback of increased computation time. However, the prominent contribution of this study is the improvement in image quality according to the results of objective evaluation and opinions of experts. If high-end image processing hardware is used to reduce implementation time, the proposed methods may be useful for clinical applications.

Keywords: Ultrasound, Image Restoration, Super-Resolution, Speckle Suppression

ÖZ

B-MOD ULTRASON GÖRÜNTÜLERİ ÜZERİNDE HASSAS SİSTEM MODELİ KULLANARAK TEK-GÖRÜNTÜLÜ BAYESÇİ ONARMA VE ÇOK-GÖRÜNTÜLÜ ÇÖZÜNÜRLÜK-ÜSTÜ ONARMA

Cüneyitoğlu Özkul, Mine

Doktora, Sağlık Bilişimi Bölümü

Tez Yöneticisi: Prof. Dr. Ünal Erkan Mumcuoğlu

24.07.2019, 100 sayfa

Tıbbi görüntüleme, modern tıp kapsamında, tanı ve girişimsel müdahale planlamanın önemli bir parçası haline gelmiştir. Tıbbi ultrasonografi, diğer görüntüleme yöntemlerine kıyasla, önemli klinik avantajlara sahiptir. Tarama için gereken ekipman daha düşük maliyetli ve kolay taşınabilir özelliktedir. Yöntemin görüntüleme yapılan kişiye bilinen bir zararı yoktur; yöntem hemen her alanda güvenle uygulanabilmektedir. Ancak tıbbi ultrasonografi ile elde edilen görüntü kalitesi, diğer görüntüleme yöntemleri ile elde edilen görüntülere kıyasla genellikle daha düşük kalitededir. Görüntü kalitesinde artış, klinik kullanımda fayda sağlayacaktır. Bu sebeple, tıbbi ultrasonografide görüntü kalitesinin arttırılması konusu, gün geçtikçe, hem akademik, hem de ticari açıdan önemli bir araştırma alanı haline gelmektedir. Bu tez kapsamında, ultrason görüntü kalitesi artırımı hedeflenmiştir. Bu amaçla, hem tek hem de kesit-içi, serbest-elle toplanan çoklu 2B, B-mod görüntüler kullanılmıştır. Katı olmayan görüntü çakıştırma ve tek-görüntülü Bayesçi ve çok-görüntülü çözünürlük-üstü onarma yöntemleri, benek örüntüsü üzerine detaylı istatistiksel bir çalışma ile birleştirilmiştir. Görüntüleme sistemi karakterizasyonunda gerçekçi doku fantomundan veri toplanmıştır. Önerilen yöntemler, gerçekçi meme fantomlarında ve gönüllülerden toplanan yüzeyel doku görüntülerinde test edilmiştir. Önerilen yöntemler, literatürdeki yaygın görüntü onarma ve filtreleme yöntemleri ile kıyaslanmıştır. İyileşme miktarının değerlendirilmesinde, uygun nesnel ölçütler kullanılmıştır. Buna ek olarak, uzman görüşlerinin değerlendirilmesinde görsel puanlama çözümlemesi uygulanmıştır. Önerilen yöntemler, hesaplama süresi açısından dezavantajlıdır. Ancak çalışmanın öne çıkan katkısı, görüntü kalitesinde nesnel ölçütler ve uzman görüşüne göre artış sağlanmış olmasıdır. Yüksek kapasiteli görüntü işleme donanımı kullanılarak hesaplama süresi azaltılırsa, önerilen yöntemler klinik uygulamalarda kullanışlı hale gelebilir.

Anahtar Sözcükler: Tıbbi Ultrasonografi, Görüntü Onarma, Çözünürlük-Üstü, Benek Gürültüsü Azaltılması

To My Mother Emine Cüneyitoğlu,

ACKNOWLEDGMENTS

TABLE OF CONTENTS

LIST OF TABLES

LIST OF FIGURES

LIST OF ABBREVIATIONS

2D	Two-Dimensional
3D	Three-Dimensional
AD	Anisotropic Diffusion
BR	Bayesian Restoration
BF	Bilateral Filter
BSRR	Bayesian super-resolution restoration
CG	Correlated Gaussian
CNR	Contrast to Noise Ratio
CT	Computerized Tomography
GPU	Graphical Processing Unit
HR	High Resolution
IBP	Iterative Back Projection
IQ	In-Phase and Quadrature Components
IID	Independent and Identically Distributed
LR	Low Resolution
MAP	Maximum A-Posteriori
ML	Maximum Likelihood
MMSE	Minimized Mean-Squared Error
MRF	Markov Random Field
MRI	Magnetic Resonance Imaging
MSE	Mean Square Error
NID	Normalized Information Density
PET	Positron Emission Tomography
POCS	Projection Onto Convex Sets
PSF	Point Spread Function
PSNR	Peak Signal to Noise Ratio
ROI	Region of Interest
UG	Uncorrelated Gaussian
US	Ultrasound
WF	Wiener Filter

CHAPTER 1

1. INTRODUCTION

1.1. Motivation

From clinical applications to intervention/surgery planning, medical imaging is an essential part of medical practice. Compared to other modalities such as MRI, CT, PET, medical ultrasound provides many benefits. The equipment is less expensive, there is no harm known to human tissue, such that ultrasound can even be used safely in obstetrics. This makes image quality improvement in medical ultrasound research very important, in both academic and commercial context.

Ultrasound imaging research has been going on for several decades. However, in ultrasound literature and research, there are various subjects that are not covered entirely. One such example is the spatial correlation of speckle in clinical ultrasound images which is an interesting area that is not quite examined except in a limited number of works. Ultrasound speckle occurs due to imaging physics when tissue is examined. This phenomenon degrades image quality significantly.

Image restoration aims to improve image quality, given an image formation model. Super-resolution, which is a powerful image restoration method, was proposed for recovering spatial frequencies that are beyond diffraction limit that is determined by imaging physics. Multi-image super-resolution is one way to apply this by observing a scene from many different views and making use of data obtained. This is another research area that is not quite covered for clinical ultrasound images. Bayesian approach allows the statistics to be incorporated in the system model, which, in several cases, leads to improved accuracy. The potential of super-resolution in ultrasound had been examined in a few works and some improvement in image quality was presented in those examples which seemed promising for further applications.

Availability of high-end electronic equipment (i.e. Graphical Processing Units - GPUs) make implementation of some image processing algorithms possible. In this thesis, improvement of diagnostic image quality of 2D images is aimed, implementing above-mentioned techniques using computational power of GPU when necessary. The motivation was to provide output that has significant clinical value and help to define potential applications in medicine.

1.2 Physics of Ultrasound

Medical ultrasound is an imaging technique that utilizes longitudinal, high frequency sound waves that are able to penetrate through live tissue. Sound waves travel with a varying speed (1400-1600 m/s, Shung et.al, 1992) in structures that form live tissue, such as fat, muscle, cartilage and so on. Speed of sound *(c)* is related to frequency *(f)* and wavelength *(λ)* through the well-known wave equation:

$$c = \lambda f \qquad (1)$$

In case of liver tissue as an example, the speed of sound is 1570 m/s (Shung et.al., 1992). A sound wave with 1 MHz central frequency is supposed to have 1570/1000000 = 1.57 mm wavelength, which, in theory, enables imaging with that resolution.
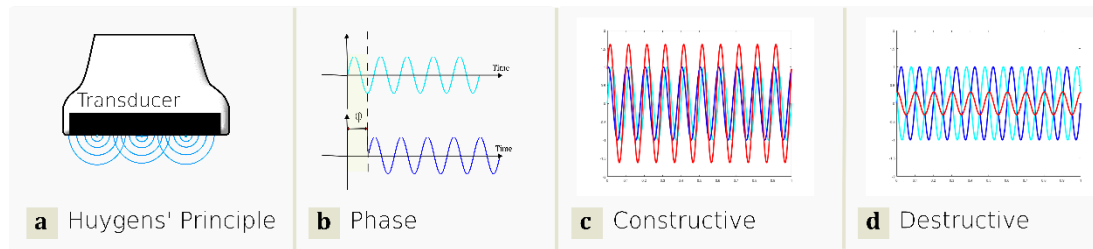
Figure 1: Huygens' principle, illustration of phase, constructive and destructive interference of waves. Figures were previously published in (Cüneyitoğlu Özkul & Mumcuoğlu, 2018).

Huygens' principle states that, pressure emitted from an aperture of finite size is, in fact, the superposition of infinitesimal sources on its surface, as illustrated in Figure 1a. (Shung et.al, 1992). Interference is summation of waves. Related to their phase ϕ, the summation of waves forms constructive or destructive interference, as illustrated in Figure 1b,1c,1d). The sum of two blue waves of different phases is shown as the red wave. The amplitude of the red wave is higher than blue waves in the first case and lower in the second case. This is called diffraction phenomenon, which describes the shape of the beam emitted from an aperture as well (Szabo, 2004). All emitted 3D spherical waves from the transducer surface interfere with each other and an acoustic radiation pattern of pressure (in Pascal units), as illustrated in Figure 2, is formed. This figure is formed using Field II simulator, (Jensen & Svendsen, 1992; Jensen, 1996) with 4 MHz center frequency and 32 transducer elements, single focus at 60 mm. All of these parameters are explained in the following paragraphs.

2
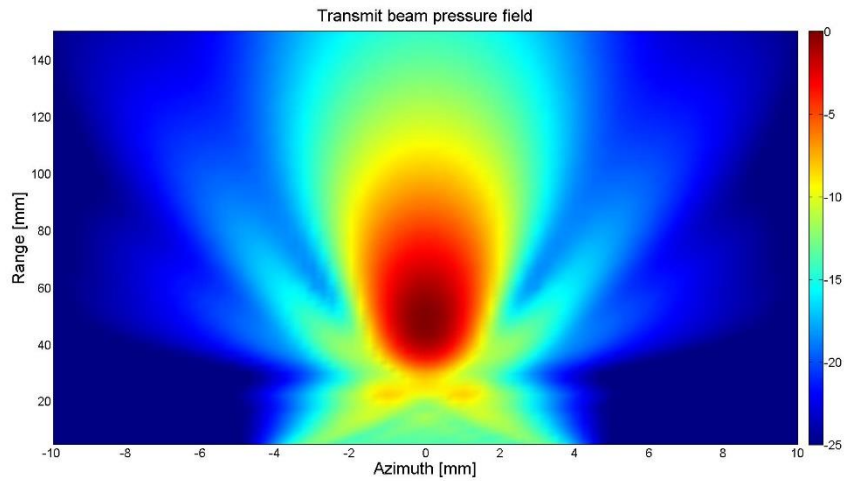
Figure 2: Acoustic radiation pattern of transmitted pressure formed using Field II simulator (Jensen and Svendsen, 1992; Jensen, 1996) in dB scale. The pressure is calculated for each point on a grid on x-z axis on 30x145 mm area. The grid starts at -10 mm and ends in +10 mm in lateral axis divided by 0.25 mm intervals and starts at +5 mm and ends at +150 mm depth divided by 2.45 mm intervals. Single focus is placed at 60 mm depth. Figure was previously published in (Cüneyitoğlu Özkul & Mumcuoğlu, 2018).

The sound beam transmitter through finite aperture can be *reflected*, *refracted*, *absorbed* and *scattered* (Figure 3). Among those, the *reflected* signals from tissue interfaces (where tissue properties vary) are utilized in medical ultrasound imaging. However, all of these cases that sound beam faces should be considered and examined in case of image formation.
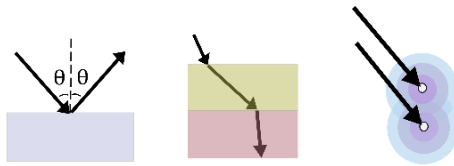
Reflection, refraction and scattering

Figure 3: Types of interaction of sound beam with the tissue. Figures were previously published in (Cüneyitoğlu Özkul & Mumcuoğlu, 2018).

The most important type of reflection is the specular reflection, which occurs when the beam is reflected through the same angle as the surface normal. Refraction of sound is similar to the refraction phenomenon in optics; it occurs when there is difference between characteristic impedance of two tissues (Shung et.al, 1993). The *characteristic impedance (Z)* is defined as follows:

$$Z = \rho c \tag{2}$$

where density *(ρ)* and speed of sound *(c)* is involved. As the sound beam is refracted through tissue, its angle varies with respect to surface normal, depending on the characteristic impedance values of the tissue layers. The elements that convert one form of energy to other is called *transducers*. Ultrasonography gel is applied to surface that is intended to be imaged. The transducer is a rigid body and the gel fills the gaps and allows no air. This prevents undesired reflections and high impedance difference between transducer surface and the tissue.

The above model assumes tissue as layers with varying characteristic impedance and the sound beam interaction occur in tissue interfaces. In reality, the small structures that form layers of tissue may not have homogenous characteristic impedance. This inhomogeneity of tissue results in scattering. The sound beam hits structures smaller than wavelength and make random reflections. This also enables the inner structures within layers of tissue to be imaged.

In ultrasound images of tissue, a large number of scattering structures result in random constructive and destructive interference of sound waves. It results in a granular texture with random bright and dark spots called speckle (Burckhardt, 1978). As observed in Figure 4, speckle exists all over the ultrasound images. On homogenous areas, the signal level is expected to be constant and the granular pattern is considered as speckle noise. A sample area that is assumed to be homogenous is zoomed in for a tissue-mimicking ultrasound phantom image. In Figure 4b, the cross section from human thyroid is presented. Again, the granular pattern is observed, and the anatomical structures are overlaid with this pattern.

Understanding the mechanism behind speckle formation is an essential part of ultrasound imaging. For this reason, there is detailed information presented in a subsection devoted to this subject.

Sound beam is eventually absorbed within tissue as it travels deeper. The sound energy first transferred to kinetic energy and causes the tissue molecules to vibrate. Then, it is converted into heat energy and this heat is dissipated in tissue. If the tissue is exposed to high levels of sound energy, the heat generation may be detrimental to health of tissue cells. Therefore, power of sound energy in terms of (Watt/cm2) should be controlled (Shung et.al, 1992). Moreover, the mechanical waves travelling through the tissue cause compression and rarefaction. This results in formation of bubbles. When the formed

bubbles burst, the tissue is harmed. This effect is called *cavitation*. In order to avoid this phenomenon, the power of sound energy must be considered carefully.

A pulse with short duration is sent from a transducer that transmits an electrical signal into mechanical vibration. As this pulse travels into depth of the tissue, a portion of it is reflected back from scattering surfaces. These reflected echoes are then collected using transducers (usually the same transducers that have converted the electrical signal into mechanical vibration), that, this time, convert pressure changes on the tissue surface due to reflected waves back to electrical signals. The backscatter amplitude measured as electrical signal is directly related to the pressure fluctuations in the transducer interface. After that, envelope detection is implemented on the acquired signal and the output is log compressed for human visual range. This is called pulse-echo imaging. A thin strip into depth of the tissue is formed which is called an A-line, shown in Figure 5a. This signal holds information regarding the tissue reflectivity along a single line.

The absorption phenomenon results in reduced signal levels from deeper tissue and therefore, the image becomes darker. Although compensated as much as possible in image acquisition setup, this effect appears distinctly on US images.
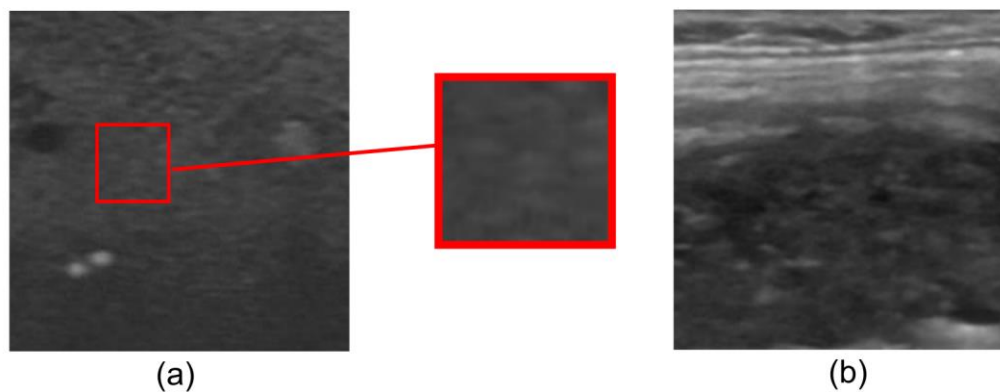
Figure 4: Sample ultrasound images to observe speckle phenomenon (a) Sample region extracted from a tissue-mimicking resolution phantom; (b) Human thyroid image.

The reflective property of targets inside tissue is called *echogenicity*. If the signal amplitude received from a specified region is higher than a reference value is called *hyperechoic* region and if the amplitude is lower, it is called *hypoechoic* region. If there is no echo signal from the area, it is called *anechoic* region. Samples of targets with varying echogenicity is presented in Figure 5b, 5c.
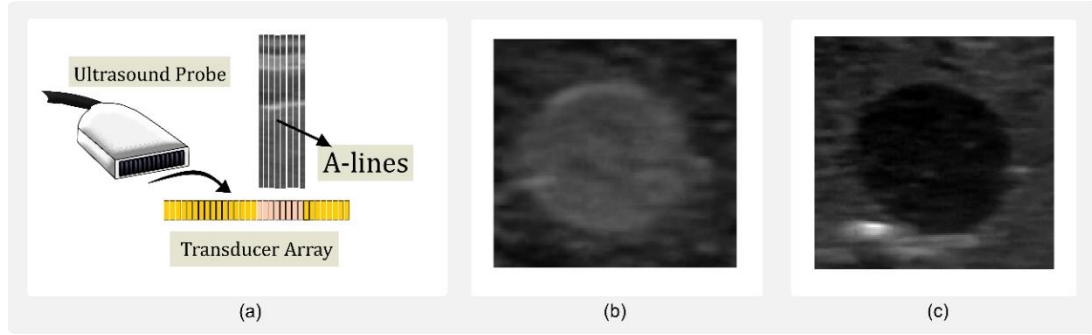
Figure 5: (a) Illustration of A-Lines, Samples of varying echogenicity from tissue-mimicking breast phantom. Figure was previously published in (Cüneyitoğlu Özkul & Mumcuoğlu, 2018); (b) Hyperechoic (breast mass) target; (c) Hypoechoic (cyst) target.

1.3.   Ultrasound Image Model and Resolution

When the angular frequency ω_0 and the wave number k is defined with respect to a single frequency f_0,

$$\omega_0 = 2\pi f_0 \tag{3}$$

$$k = \frac{2\pi}{\lambda} \quad \text{or} \quad k = \frac{\omega_0}{c} \tag{4}$$

the pressure radiation pattern by a point at the center of the aperture can be modeled as follows, (O'Donnell, 1999),

$$p(R, \theta) = \frac{e^{ikR}}{R} cos\theta \tag{5}$$

where θ is the angle from the normal to the radiating surface, R is the distance, illustrated in Figure 6. As R increases, the pressure decreases. Note that the complex frequency equation $Re\{e^{ikR}\} = cos(kR)$ is preferred here to model the physical system with single frequency.

The cosine term is for the angle of deviation from the normal to the aperture surface. This term can be omitted by only considering the θ angles that are normal to the aperture surface.

For a point source on the active transducer aperture, the distance from every point (R, θ) can be written as:

$$d(x) = \sqrt{(x - R\sin\theta)^2 + R^2\cos^2\theta} \qquad (6)$$

and this relation is simplified to

$$d(x) = R\sqrt{1 - \frac{2x}{R}\sin\theta + \frac{x^2}{R^2}} . \qquad (7)$$

In order to reduce mathematical complexity for further operations, a Taylor series expansion up to second order is applied to Equation (7). In Figure 6, let the total aperture size $D=2a$ (from $-a$ to a), if the ratio $f\# = \frac{Range}{Aperture\ Diameter}$ is larger than 2, *Fresnel approximation* can be made (O'Donnell, 1999), (Szabo, 2004).
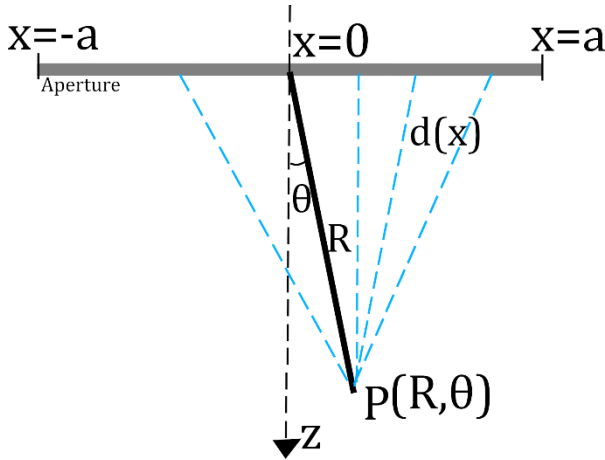
Figure 6: Distance function from a point to transducer surface is defined. Figure was previously published in (Cüneyitoğlu Özkul & Mumcuoğlu, 2018).

Fresnel approximation allows higher order terms including the third order term to be omitted (Szabo, 2004). Finally, the distance function takes the following form:

$$d(x) = R - x\sin\theta + \frac{x^2\cos^2\theta}{2R} . \qquad (8)$$

7

The net pressure $P(R,\theta)$ at (R,θ) for the full aperture can be obtained by placing $R=d(x)$ in Equation (5) and integrating in the $[-a,a]$ interval:

$$p(R,\theta) = \int_{-a}^{a} \frac{e^{ikd(x)}}{d(x)} dx = \int_{-a}^{a} \frac{e^{ik(R-x\,sin\theta+\frac{x^2 cos^2\theta}{2R})}}{(R-x\,sin\theta+\frac{x^2 cos^2\theta}{2R})} dx \; . \tag{9}$$

By considering only the near normal angles, the $cos\theta$ term in Equation (5) can be omitted. For the terms in the denominator, R term is dominant, hence, the other terms can be neglected (This is not possible the denominator, since x term is significant in the phase term). The net pressure can be written as (O'Donnell, 1999):

$$p(R,\theta) = \frac{e^{ikR}}{R} \int_{-a}^{a} e^{\frac{ikx^2}{2R}} e^{-ikx\,sin\theta} \; dx \; . \tag{10}$$

There are three dimensions contributing to the image, as shown in Figure 7. The resolution in these directions are called lateral, axial and elevational. The factors that determine resolution in these directions are examined in the following paragraphs. The resolution is related the to *point spread function* (PSF) of an imaging system. This is a function that measures the ability to resolve point targets (Szabo, 2004). *Full-width-half-maximum* (FWHM) for ultrasound is defined as the length where the reduction of 6 dB in height of the pulse to peak value. In 3D, it becomes a spherical region and called as *resolution cell*.

1.3.1. Lateral Resolution. We define $k'= k\,sin\;\theta$ and a rectangular aperture function, including the phase term related to distance as $A(x) = e^{\frac{ikx^2}{2R}} rect(\frac{x}{a})$. Inserting the aperture function to Equation (10) (O'Donnell, 1999):

$$p(R,\theta) = \frac{e^{ikR}}{R} \int_{-\infty}^{\infty} A(x)e^{-ik'x}dx = \frac{e^{ikR}}{R} B_R(k'). \tag{11}$$

In Equation (11), k' term represents angular effect (since for small angles $sin\;\theta = \theta$). In that case, the overall pressure at point (R,θ) expressed as $B_R(k')$, the angular spectrum (Fourier Transform, $\Im\{A(x)\}$) of the aperture function times the pressure of a point source at the center. The term $e^{\frac{ikx^2}{2R}}$ is called *focusing term* and its undesired effect is removed via focusing. The details on focusing is explained in the following paragraphs. Note that as the aperture size increases (i.e. a gets larger) pressure distribution along θ gets narrower.

Also, as f_0 increases, beam pattern gets narrower. The lateral resolution of the system depends on two factors; center frequency f_0 and apodization, *A(x)*.
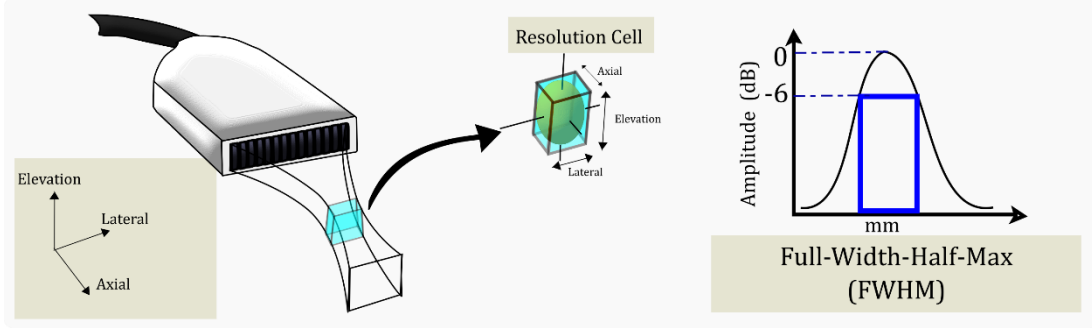
Figure 7: Ultrasound image axes, resolution cell and full-width-half-maximum (FWHM). Figures were previously published in (Cüneyitoğlu Özkul & Mumcuoğlu, 2018).

A generalization of Equation (11) can be made by weighting the aperture with a function $\widetilde{W}(x)$ ($\Im$ is the Fourier transform)**:**

$$\tilde{A}(x) = \widetilde{W}(x)rect(\frac{x}{a}) \ \to B_R(k') = \Im_{k'}[\tilde{A}(x)]. \tag{12}$$

At this point, it should be noticed that the radiation pattern is the product of point source positioned at the center of the aperture and the anguar spectrum $B_R(k')$. This means that both the radiation pattern and the lateral PSF is controlled by the aperture function, (O'Donnell, 1999).

The pulse-echo imaging can be modeled simply with a transmit aperture function with angular spectrum $B_R{}^t(k')$, a receive aperture function with angular spectrum $B_R{}^r(k')$ and a scattering distribution for acoustic source, $\eta_R(k')$. The pressure pattern is convolved with scattering distribution and then detected by the receive pattern, $p(R,\theta)=(e^{ikR}/R)\,B_R{}^r(k')$. All these are combined into the following model, where * is the convolution operator:

$$S_R = \frac{e^{2ikR}}{R^2}[B_R^t(k') * \eta_R(k')]B_R^r(k'). \tag{13}$$

In here, S_R is the pulse-echo response at range for transmit and receive apertures R, (O'Donnell, 1999). This expression can be rearranged,

$$S_R = \frac{e^{2ikR}}{R^2}[B_R^t(k')B_R^r(k')] * \eta_R(k'). \tag{14}$$

9

using the reciprocity as convolution is a linear operation. The angular spectrum of transmit aperture function $B_R{}^t(k')$ and angular spectrum of receive aperture function $B_R{}^r(k')$ is combined into $B_R(k')$,

$$S_R = \frac{e^{i2kR}}{R^2}[B_R(k') * \eta_R(k')]$$ (15)

and $B_R(k')$ is expressed as:

$$B_R(k') = B_R^t(k')B_R^r(k') = \Im[\tilde{A}(x)] = \Im[\tilde{A}_t(x) * \tilde{A}_r(x)].$$ (16)

In here, $\tilde{A}(x)$ is called the equivalent aperture function for the pulse-echo system, which is a convolution of transmit and receive aperture functions, (O'Donnell, 1999).

Since the lateral PSF is related to transmit and receive aperture functions, these functions can be adjusted for better resolution. The goals for enhancing the lateral resolution are:

1- $B_R(k') = \delta(k')$

2- $S_R \rightarrow S_R(k_0) = \delta(k' - k_0)\eta_R(k_0)$

where $\delta(.)$ is the dirac delta function.

First goal is to have an equivalent aperture function, as close to delta-function as much as possible. In that case, the output signal is going to simply be proportional to the scattering function. The second goal is to satisfy this proportionality still, if the beam is moved normal to primary beam direction. There is the parabolic phase term, $kx^2/2R$, in the aperture functions that would hinder these goals. However, since this is a range dependent term, applying the above mentioned focusing scheme with phased arrays is effective to avoid this issue (O'Donnell, 1999).

The beam plots with selected aperture functions are illustrated in Figure 8 for clarifying these statements. The figure is formed for a 4 MHz beam, 10 mm width aperture sampled with 128 elements, 30 mm transmit and receive focus and imaging at 30 mm depth. The transmit and receive aperture functions are selected to be the same apodization functions; rectangular, Hamming and cosine. In the figure, it is observed that the rectangular apodization yields the most narrow angle, however, it results in high side lobes which produce spurious signals that produce artifacts in the image (Shung et.al., 1992). On the other hand, the beam plot with Hamming window shows reduced side lobes but a wider main lobe. There is a tradeoff between having a sharp beam and low side lobes. A midway between these can be the cosine window, as shown in Figure 8. Beamplots at several depths for the same aperture are inserted into imaging range of an example transducer in

Figure 9. The lateral resolution defined by -6dB reduction is illustrated as the yellow region in the figure.
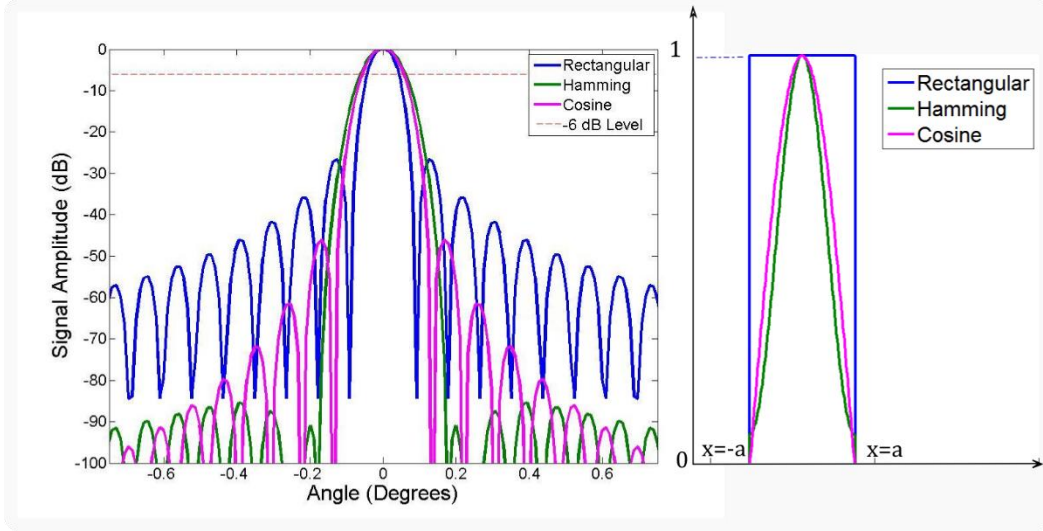
Figure 8: The beam plot for the selected transmit and receive aperture function and the apodization. Figures were previously published in (Cüneyitoğlu Özkul & Mumcuoğlu, 2018).

1.3.2.   Axial Resolution. When *R* is the total distance travelled by a pressure wave, *c* is the average speed of sound in the medium and *t* is the total time passed between the firing and return of the wave back to transducer, then, there is a simple relationship between these variables:

$$t = \frac{2R}{c}$$ (17)

Axial resolution or range resolution depends on spatial extent of the transmitted pulse τc where τ is the pulse width and *c* is the speed of sound in the medium. Pulse width is multiplication of wavelength ω_0 and number of cycles in the pulse. The ultrasound waves attenuate as they penetrate into depth of the tissue. High frequencies penetrate more than low frequencies, therefore, there is a tradeoff between resolution and depth penetration.

1.3.3.   Resolution in Elevation. Focusing in elevation depends on transducer thickness. In 1D arrays, there is a constant lens attached to the transducer surface. This leads to mechanical focusing at a single depth and elevational resolution gets worse outside that single focal depth, as illustrated in Figure 10a. For this reason, depending on the depth of the region of interest, probes with different types of mechanical focus in elevation are designed and used.

11

1.3.4. Linear Pulse Echo Model for US. When all the scatterers are assumed to lie on the same plane, the linear pulse-echo model of the imaging system can be formed as follows, (O'Donnell, 1999; Jensen, 2002):

$$S(t, k'_m) = \frac{1}{R^2} \int \int \eta(R, k') \left[A\left(t - \frac{2R}{c}\right) e^{i\omega_0\left(t - \frac{2R}{c}\right)} B_R(k'_m - k') \right] dR \, dk' \tag{18}$$

where $\eta(R,k')$ is a 2D scattering function, $S(t,k'_m)$ is the time samples at beam pointed in direction defined by k'_m, $A\left(t - \frac{2R}{c}\right)$ is the apodization function and $\frac{1}{R^2}$ is the range dependent gain compensation term. Referring to equations (3) and (4), as f_0 is increased, k increases.
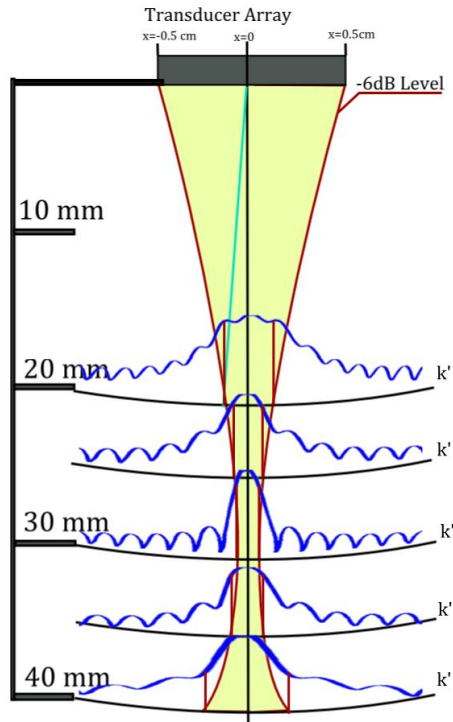
Figure 9: Beam plots at several depths form the curve that defines overall lateral resolution (yellow area) for a single focus placed at 30 mm. Figure was previously published in (Cüneyitoğlu Özkul & Mumcuoğlu, 2018).
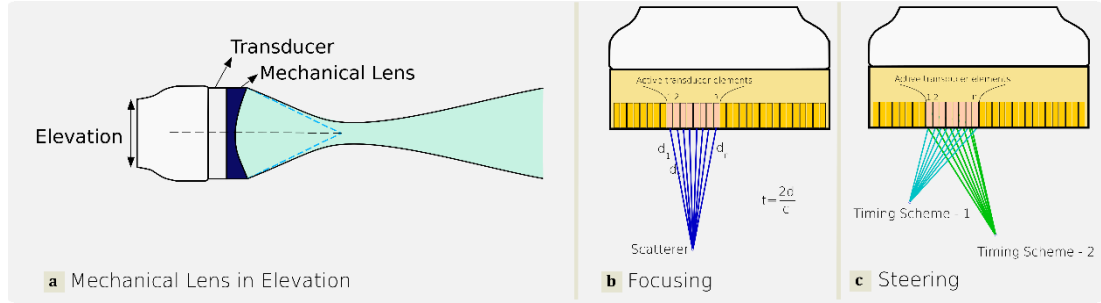
Figure 10: (a) Mechanical focusing in elevation; (b) Focusing; (c) Steering. Figure was previously published in (Cüneyitoğlu Özkul & Mumcuoğlu, 2018).

1.4.   Focusing and B-Mode Image Formation

In modern ultrasonic imaging systems, the aperture is formed by many transducer elements in array form, as shown in Figure 5a, Figure 10b, 10c, Figure 11. The distance between centers of the transducer elements is called *pitch* and the gap between elements is called *kerf*, as illustrated in Figure 11. This allows the active aperture to be adjusted flexibly; the elements can be fired in desired groups such that the aperture size can be changed, an apodization function and beamforming can be introduced.
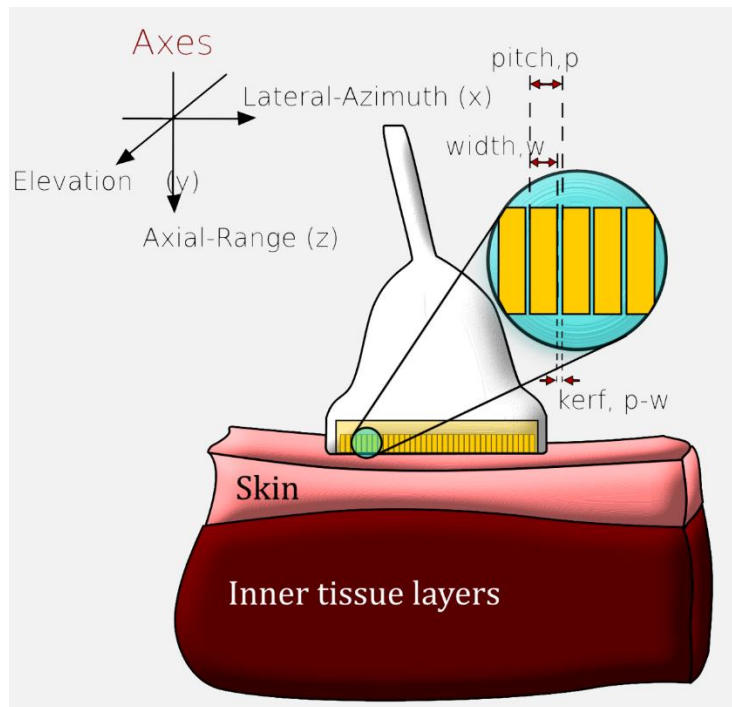
Figure 11: Array of transducers and other essential parts and dimensions in an ultrasound probe. Figure was previously published in (Cüneyitoğlu Özkul & Mumcuoğlu, 2018).

Assuming a scatterer at depth *d*, there is a slight difference in the total distance between the array elements' interface and the scatterer as illustrated in Figure 10b. This results in delayed arrival of reflected waves to different elements in the transducer surface. *Focusing* is available by adjustment of time delay schemes, while transmitting and receiving the pulse, such that there can be focus inserted on a specific point. The emitted acoustic pressure field shown in Figure 3 is calculated for a focused beam at 60 mm depth. Moreover, the delays for the array elements can be adjusted such that the *steering* of the emitted beam is controlled to view a specific region of interest in any place in range, as shown in Figure 10c.

In modern ultrasound systems, the desired transmit beam shape is formed by the time delays, however, the receive focus is dynamically swept. This scheme called *dynamic receive focusing*, allows catching the reflections from any depth instantly (Shung et.al., 1992). To sum up, by manipulating the time delays, focusing on a specific area can be achieved by an array of transducers, as illustrated in Figure 10b and 10c as different timing schemes. Combining the A-lines obtained, a B-mode ultrasound image is formed. B stands for the "brightness", the gray level intensities in the scan converted image. All of these operations are available in real-time, in today's technology.

Steps of B-Mode image formation is given in Figure 12 as schematics. As stated above, formation of every A-line requires at least one transmit-receive operation (There is multiple transmit-receive required in case of multiple focusing, this imporves lateral resolution while reducing time resolution, since additional transmit-receive operations cost time). Apodization is applied to each channel by amplitude modulated pulses and beamforming is applied to the specified depth. After transmitting the signal, each transducer is switched to receive mode. As stated in previous paragraphs, sound waves are absorbed within tissue, therefore, the signal amplitude of the signals that are received from depth is reduced. In order to comply with this situation, echo signals are amplified according to their assumed depth. The signals from deeper tissues are amplified more; this operation is called *time-gain compensation*. After receive beamforming (dynamic receive focusing), demodulation, envelope detection of in-phase and quadrature (IQ) data and harmonics filtering steps, a high dynamic range analytic signal is obtained. This signal is then log-compressed for human visual range and scan conversion (which involves interpolation to convert the A-lines to the rectangular screen pixels) is applied to fit into display screen properly. The output is a gray level image where the intensity is nonlinearly mapped to echogenicity of targets. Modern ultrasound devices often make these mapping adjustments available and customizable based on user preference. This basically results in changes in image contrast.
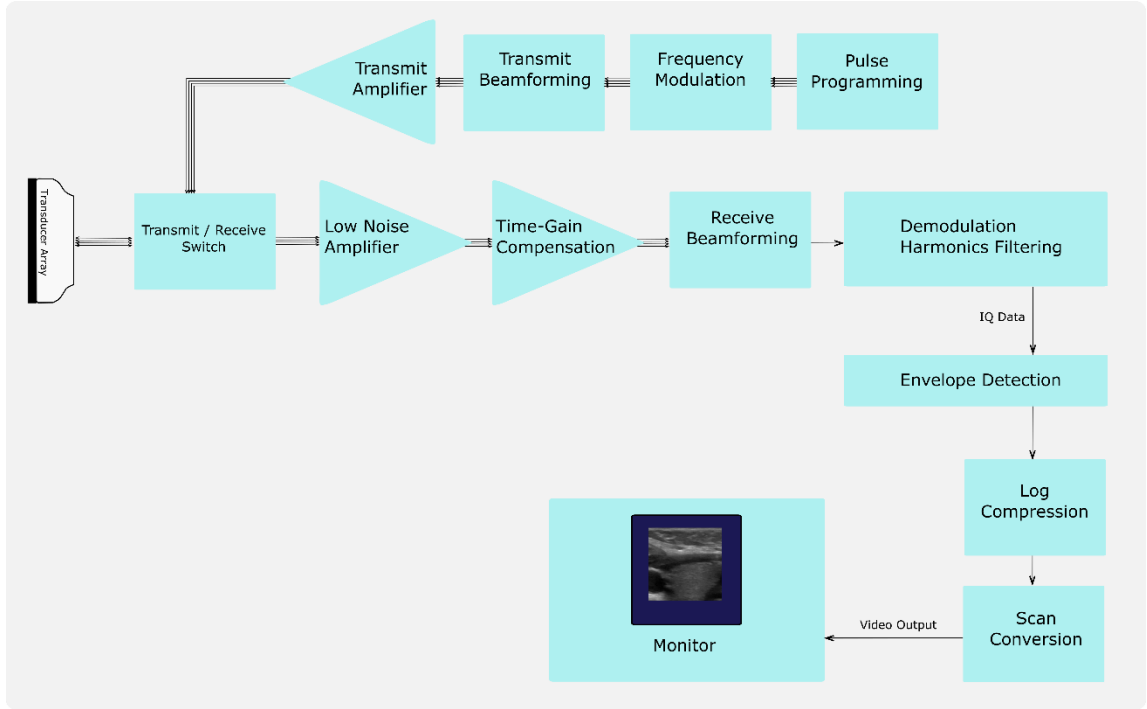
Figure 12: Steps of B-Mode image formation. Figure was previously published in (Cüneyitoğlu Özkul & Mumcuoğlu, 2018).

1.5.   Image Model for B-Mode Images

Equation (18) is a widely accepted model for IQ data (Chen & Parker, 2017). When $\vec{x}$ is assumed to be the envelope-detected signal before log-compression step, the echo signal can be modelled as follows, (Wagner et. al., 1983; Tay et. al., 2010):

$$\vec{y} = (\vec{h} * \vec{x})\vec{n}_m \tag{19}$$

In here, $\vec{y}$ stands for the recorded signal, $\vec{h}$ is the point spread function of the imaging system, '*' symbol is the convolution operation and $\vec{n}_m$ is the multiplicative noise term (speckle). After envelope detection, the echo signal becomes absolute valued, therefore, the log-compression step is applicable.

When the envelope detection and log-compression is applied to Equation (19), the following expression is obtained:

$$\log(\overrightarrow{|y|}) = \log(|\vec{h} * \overrightarrow{x|}) + \log(|\vec{n}_m|). \tag{20}$$

Ideally, the deconvolution and the restoration operations are better performed on IQ data, but this was not available for this study. The data is acquired from the clinical ultrasound device as the B-mode video stream only. In literature, modelling the displayed B-mode image as a linear degradation model as the following is a common practice (Tay et. al., 2010; Yang et. al., 2007; Yang et. al., 2009; Wang et. al., 2009; Dai et. al., 2009; Jensen et. al., 1993):

$$\vec{y} = \vec{h} * \vec{x} + \vec{n} \qquad (21)$$

for some additive noise, $\vec{n}$. In $\vec{y}$, the effect of speckle and electronic noise is also included. In this work, the linear degradation model in Equation (21) is used for restoration of B-mode images.

1.6. Ultrasound Speckle and Correlation

As briefly mentioned above, as a result of scattering, the granular pattern observed in ultrasound images is called speckle. Speckle phenomenon occurs due to wave interactions. In addition to medical imaging, speckle phenomenon is observed in several other forms of imaging such as astronomy, synthetic aperture radar (SAR) and laser illuminated surfaces where there is coherence of sound or light waves. Speckle in astronomical imaging occurs due to observing through the inhomogeneous atmosphere, whereas the source of speckle in SAR and medical imaging is the scatterers that are much smaller than one wavelength (Goodman, 2007). In medical ultrasonography, the source of speckle is considered as the inhomogeneities in the different types of tissues such as the changes in density, compressibility due to underlying cell structure, (Jensen, 2002). A grainy pattern is formed due to constructive and destructive interference of sound waves (see Figure 1c, 1d) scattering from subresolution scatterers within these structures as the individual signals with scatter are superpositioned (Goodman, 1996) to form the ultrasound image.

Speckle phenomena differs from typical random noise with some of its intriguing properties. First of all, it is a part of the signal and although mostly considered as noise, some useful information about the physical properties of the underlying tissue may be derived from its appearance. There is plenty of research conducted (Bharti et. al., 2017), where the texture of speckle is examined for tissue characterization purpose. Statistical properties of speckle are utilized in another area called *speckle tracking*, described in section 1.7 in detail.

1.6.1. Statistics of Speckle. Coherence is a physical phenomenon related to waves. Ideal coherence of waves occurs when their wavelength is equal but phases are different, which can be illustrated as in Figure 1b. In other words, monochromatic waves of any phase can be stated as an example of this phenomenon (Goodman, 1996). A random walk is defined as a set of discrete steps in different directions, in which magnitude of every step takes a non-negative value, (Barlett, 1955). Putting these two definitions together, the speckle in

polarized monochromatic light is described as a random walk in the complex plane and the literature is mostly based upon this fundamental explanation, (Goodman, 2007).

The waves can be expressed as waves in phasor notation, where a_i is the amplitude and θ_i is the phase of the ith wave. When summed, A is the resultant phasor, A is the total amplitude, θ is the resulting phase and N is the number of scatterers (Goodman, 2007):

$$\boldsymbol{A} = Ae^{j\theta} = \frac{1}{\sqrt{N}}\sum_{i=1}^{N}\boldsymbol{a_i} = \frac{1}{\sqrt{N}}\sum_{i=1}^{N}a_i e^{j\theta_i} \tag{22}$$

Under the assumption that there are a very large number of scatterers, the Central Limit Theorem is applicable (Goodman, 2007). In here, the phasor amplitudes and the phases are random in the interval $[-\pi,\pi]$. In addition to that, amplitude and the phase are statistically independent from each other. The real and the imaginary parts of the resultant phasor is expressed and their relationship to A, θ is defined. The standard deviations for the real and imaginary parts are assumed to be equal and joint probability density function for the resultant phasor is written. For the mathematical details, the work of Goodman (2007) can be viewed.

Integrating in the $[-\pi, \pi]$ interval, the marginal statistics of A can be obtained. These are known as Rayleigh statistics, when is A treated as a random variable and σ being a scale parameter of the distribution (Wagner et. al., 1983; Goodman, 2007):

$$P_A(A) = \int_{-\pi}^{\pi} P_{A,\theta}(A, \theta)\mathrm{d}\theta = \frac{A}{\sigma^2}e^{-\frac{A^2}{2\sigma^2}} \quad \text{s.t.}\, A \in \mathbb{R}^+ \tag{23}$$

As mentioned with reasons in the above paragraphs, the Rayleigh distribution requires large number of scatterers per resolution cell (Burckhardt, 1978; Wagner et. al., 1983). In Wagner et.al. (1983), scatterer size of 20-150 µm and number of particles per resolution cell 10-200-500 is studied.

Speckle observed with Rayleigh statistics is named *fully developed speckle* in the literature (Wagner et. al., 1983). However, there are some factors that can cause deviations from Rayleigh statistics, which are stated by Tuthill et.al., (1988), Klein (2012) as:

- Fewer number of scatterers per resolution cell
- The necessity for a limitation of signal bandwidth
- Envelope detection operation
- Log compression, scan conversion (interpolations etc.) operations
- Application of speckle reduction algorithms on B-mode images
- Presence of a coherent component

As the number of scatterers decrease, there are deviations from Rayleigh statistics, which is usually the case with real tissue as stated in Tuthill et.al. (1988). In Tuthill's work, the distribution, the amplitude and periodicity of scatterers and their effect on B-mode statistics is examined in detail (Dutt, 1995). The existence of a coherent component may

occur due to periodicity of the scatters or specular scattering from surfaces like bones (Dutt, 1995). This adds periodic components to the random phasor model explained above. This case can be modeled as the addition of a constant real component to the resultant phasor.

The Rayleigh distribution is, in fact, a specialization of a broader set of distributions called Rician distibutions (Goodman, 2007). With a constant coherent component, the speckle yields a Rician distribution. Jakeman and Pusey (1978) proposed the K-distribution model for scattering. In the work of Dutt (1995), the K-distribution is examined in detail as a distribution parameter can directly be related to the underlying speckle distribution. Another distribution, named Homodyned-K, can be applied to the case where there is both sparse number of scatterers per resolution cell and a constant phasor term. Nakagami model proposed by Nakagami (1960) was shown to be specifically more powerful for the RF data (Klein, 2012). Furthermore, by modifying the parameters of this distribution, all of the previously described scatter models can be obtained.

Rician of Inverse Gaussian (RiIG) distribution suggested by Eltoft (2005) was shown to model the ultrasound amplitude statistics effectively. This model is claimed to consist of terms that roughly correspond to the phenomena named as "diffuse" and "coherent" scattering. Diffuse scattering is considered the pure random part of scattering, which is the result of the convolution of a point spread function with itself (Wagner et.al., 1983) and coherent scattering is due to strong and periodic reflectors which result in a Rician distribution (Goodman, 2007). RiIG distribution is a compound distribution. A compound distribution is a probability distribution of a random variable with variance set to another random variable with another probability distribution. Making use of this concept, RiIG models the diffuse scattering with an inverse Gaussian distribution and the coherent scattering with a Rician distribution.

Although being a rather complex probability distribution, RiIG is more flexible with three parameters and it appears to be the best fitting distribution to the ultrasound amplitude among all in literature. Referring to Eltoft (2005), the coherent scattering is not covered by Rayleigh or K distribution. Rician distribution does not have enough parameters to model the dispersion. In the work by Eltoft (2006), it is also compared to Nakagami distribution. In this work, it is also claimed to be successful in the estimation of parameters more accurately with a few samples, which is another benefit of this model.

As stated above, speckle pattern significantly reduces the performance of ultrasonic imaging. In order to obtain a better signal to noise ratio, contrast to noise ratio or improved boundaries of distinctive objects such as tumors, there are several methods applied as real-time or post-processing to acquired ultrasound frames such as compounding and speckle filtering. The above-mentioned statistical models can be utilized for designing of efficient filters. A selected set of these are mentioned in the following paragraphs.

1.6.2. *Speckle Filtering.* Filtering of the speckle pattern has widely been applied, since the emergence of the modern ultrasound. Median filtering (Loupas et. al., 1989), several

variations of anisotropic filtering (Perona & Malik, 1990), wavelet-based filtering (see the review paper by Sudarshan et. al. (2016)), Wiener filtering (WF) (Achim et. al., 2001; Pižurica et.al., 2003), variations of bilateral filtering (BF) (Tomasi & Manduchi 1998) are popular as filtering approaches. Commercial systems have ultrasound machines with speckle reduction applied in real time such as SRI (Speckle Reduction Imaging) system by General Electric (Garra, 2005). Filtering approach, however, may have a side effect of too much smoothing which may result in loss in details of boundaries and edges as illustrated in Figure 13.

| (a) | (b) | (c) |
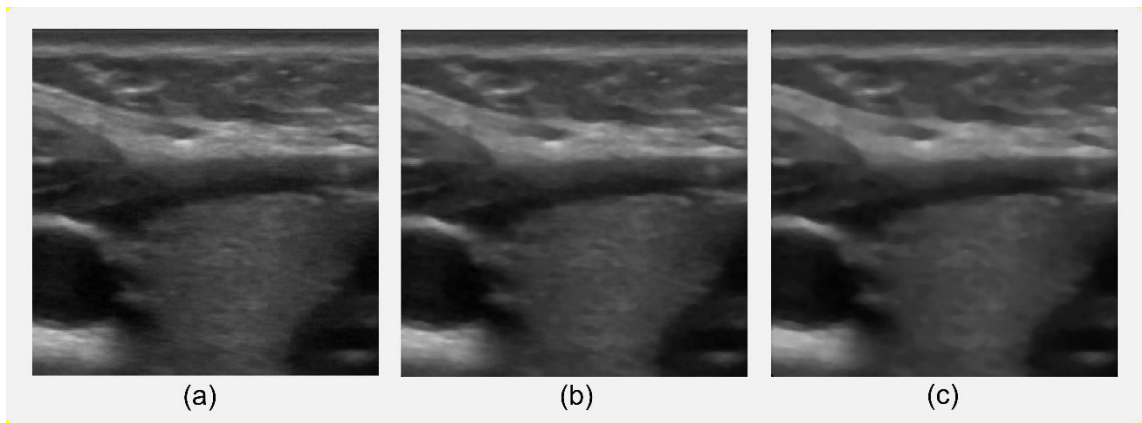
Figure 13: (a) Original human thyroid image; (b) 3x3 Kernel median filtered image; (c) 5x5 Kernel median filtered image. Some anatomical details are lost due to undesired smoothing of edges as a result of filtering operation. Figures were previously published in (Cüneyitoğlu Özkul & Mumcuoğlu, 2018).

| (a) | (b) | (c) |
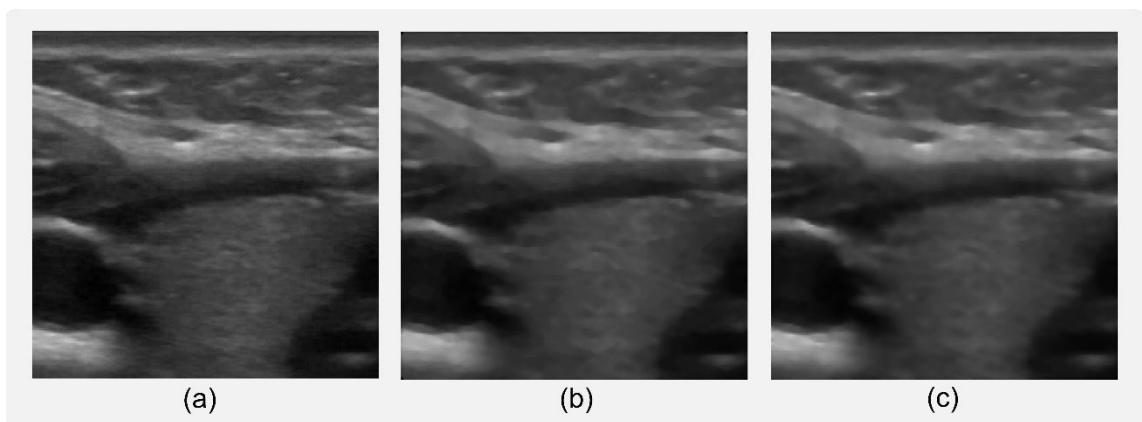
Figure 14: (a) Original human thyroid image; (b) 3x3 Kernel adaptive Lee filtered image; (c) 5x5 Kernel adaptive Lee filtered image. Some anatomical details are lost due to undesired smoothing of edges as a result of filtering operation. Figures were previously published in (Cüneyitoğlu Özkul & Mumcuoğlu, 2018).

Based on the well-known work of Perona & Malik (1990), speckle reducing anisotropic diffusion yields successful results in terms of speckle suppression while preserving edges (Yu and Acton, 2002; Aja-Fernandez and Alberola-Lopez, 2006). It is a technique based on modelling the image formation as a diffusion process. Defining a diffusion equation that is related to direction (anisotropic) and some conduction coefficient, the best estimate that is updated for each iteration is to be found. In the original paper, two different estimations of the gradient magnitude with different edge response characteristics are proposed. One option favors high contrast edges over low contrast ones, whereas the other option favors wide regions over smaller ones (Perona & Malik, 1990).

Another well-known noise suppression method for ultrasound images is the BF. The filter weights are defined depending upon the Euclidean distance of pixels. In addition to that, BF involves non-local properties such as the intensity difference of the pixels. This results in a good edge response as well as an efficient noise suppression scheme (Tomasi & Manduchi 1998; Vanithamani & Umamaheswari, 2014). In (Afsham et. al., 2015), non-local means filter is applied for denoising ultrasound images in a probabilistic manner, making use of RiIG distribution, mentioned in the above paragraphs.

Mean square error between the degraded ideal image and the observed image can be minimized. It can be expressed as an estimator in the following form (Gonzalez & Woods, 2001):

$$\vec{n}^2 = E[(\vec{y} - h * \vec{x})^2] \tag{24}$$

As adaptive filtering schemes, there are also Lee filter (Lee, 1980) and Kuan filter (Kuan et. al., 1985). These filters assume the signal and noise as uncorrelated Gaussian distributions. For an $[m \: x \: n]$ pixel area, each image pixel i, j, a local sample mean μ_l, local sample variance σ_l^2 is calculated. The pixel values $x_{i,j}^n$ are iteratively updated for n^{th} iteration with the following scheme (Kuan et. al., 1985):

$$x_{i,j}^n = \mu_l + \frac{\sigma_n^2 + \sigma_l^2}{\sigma_n^2} x_{i,j} \tag{25}$$

using the previous pixel value $x_{i,j}$ and including the noise variance σ_n^2. In Figure 14, sample images using $[3x3]$ and $[5x5]$ windows. As window size gets larger, the sample mean and variances are more accurate, however, this time, the edges are suppressed too much.

WF is also based on the minimum mean square estimator. When images are transferred to frequency domain, the following filter can be derived (Gonzalez & Woods, 2001):

$$\hat{X}(u,v) = \frac{1}{H(u,v)} \frac{H(u,v)^2}{H(u,v)^2 + \frac{N(u,v)^2}{X(u,v)^2}} Y(u,v) \tag{26}$$

In here, $H(u,v)$ is the blur function, $Y(u,v)$ is the observed image, $N(u,v)$ is the noise spectrum estimate in frequency domain. Although WF is quite fast since it is applied in frequency domain as a set of matrix multiplication operations, estimation of noise spectrum $N(u,v)$ can be challenging, depending on the noise characteristics.

1.6.3. Compounding. Making use of multiple looks to the same scene is quite common in applications suffering from speckle such as synthetic aperture radar (Soergel, 2010). Being a powerful compounding procedure, speckle pattern's decorrelation occurs with a change of viewing angle and summing the signals in these slightly changing scenes. This is due to cancellation of random walk phasor sums as the number of looks increased. In (Burckhardt, 1978), it is stated that the decorrelation between two looks occur when the transducer is moved by half of its width. The improvement of SNR is stated to be expected as sqrt(N) where N is the number of looks (Burckhardt, 1978) and to demonstrate that, an open shutter technique and a summation of amplitudes is made use of for the experiments and the increase in SNR is tabulated for multiple looks at the scene.

Making use of multiple decorrelated frames belonging to the same scene have become a commercially adopted approach as well like *GE Cross Beam technology* (Garra, 2005). In (Krucker et. al., 2002), spatial compounding of several images is applied for speckle reduction. Motion based spatial compounding is also proven useful; in (Yoshikawa et.al., 2006), it is combined with non-rigid warping estimation implemented in real time and added to consequent frames as a weighting factor. The speckle can also be eliminated by sampling at different frequencies. Wu et. al., (2014) employ frequency compounding to 8,10,12,13 MHz images, compared to actual strain measurements in a porcine tendon and a breast phantom. The work by Yoon et. al., (2013) frequency equalized compounding was implemented to enhance the contrast. Both spatial and frequency compounding is applied in the work of Tsakalakis, (2015). Split spectrum processing is applied in (Tsakalakis, 2015; Taxt & Jirik, 2004) which is another frequency compounding method from constructing images by using various close frequencies existing in the received echo.

1.6.4. Correlation of Speckle. Spatial correlation is evident in speckle images. However, the number of papers on this subject is quite limited. In (Tsuzurugi & Okada, 2002) a Bayesian scheme was implemented. In (Tilley et. al., 2015; Zheng et. al., 2018), blur in x-ray detectors were considered. In (Mellor & Brady, 2005), spatial correlation of speckle was involved in registration scheme while estimating the displacement of the noise field in the Demons algorithm mentioned in Section 1.8.

In (Baselice et. al., 2015a), WF (Equation (24)), was used with a correlated noise spectrum estimate on ultrasound images. In (Baselice et. al., 2015b), iterative WF was applied to synthetic aperture radar images.

21

1.7. Volumetric Ultrasound

Ultrasound volume data can be obtained either by a 2D probe (Shekhar & Zagrodsky, 2002; Mercier et. al., 2013) or with a sensor integration to a standard 2D system using a 1D probe (Ijaz et. al., 2010).

1.7.1. Freehand Imaging in Ultrasound. The term freehand ultrasound usually refers to a tracked probe with a sensor with tracking with making use of speckle pattern decorrelation without sensors, or a combination of both (Gee et. al., 2003; Blackall et. al., 2003; Afsham et. al., 2014) and reconstructing a volume for better visualization and resolution improvement in elevation.

Out-of-plane motion can be stated as translation in elevation, tilt around lateral and yaw around axial, as illustrated in Figure 15. Managing the out-of-plane transform can either be done with an external position sensor or in a sensorless manner. In (Treece et. al., 2002), an optical tracker is used to estimate the out of plane motion for guaranteeing the accuracy of position data in a large scale. The sensorless approach, usually named speckle tracking utilizes the decorrelation of speckle patterns. In the work of Ijaz et.al. (2010), a hybrid approach (including both inertial sensors and speckle decorrelation) is adopted with rigid registration and speckle tracking, similar to techniques in Gee et.al. (2003).

In integrating a sensor to a standard 2D system, the selected sensors vary; all solutions have various advantages and disadvantages. The works in earlier literature make use of electromagnetic trackers (Rohling et. al., 1998; Gee et. al., 2003; Huang et. al., 2005; Huang & Zheng, 2008). Optical tracking is another option for obtaining probe orientations (Blackall et. al., 2005; Treece et. al., 2002). However, optical tracking systems and infrared trackers have the disadvantage of being in the line of sight with the operation, they are still a popular option in more recent works (Hartov et. al., 2010; Laporte & Arbel, 2011; Solberg et. al., 2011). Although electromagnetic trackers do not have the disadvantage of being in line of sight, these types of sensors are reported to be affected from metal equipment that is commonly used in surgery.

In the work of Hossack et. al. (2002), a specially designed probe head with extra transducers for tracking is used, which is another interesting approach to the tracking problem. This type of systems requires a larger probe area which may lead to contact problems to the tissue.

Precise mechanical systems with optical encoders are another alternative for motion tracking (Huang et. al., 2013; Toonkum, 2011; Laporte & Arbel, 2011). The work of Harris et. al. (2010), employ a hybrid approach of IR sensor, orientation and position sensor altogether. Recently, with the technological development of inertial measurement units mounted on a regular 2D probe is of interest as well (Ijaz et. al., 2010). Inertial measurement units include accelerometers for measurement of translations, gyroscopes for measurement of rotations and magnetometers for correction. The position information is derived from an accelerometer via double integration, in which small errors in

measurement collects into a significant cumulative error called *drift,* as time increases. This can be corrected with magnetometers with a process called augmentation. All three type of sensors can be packed into a small micro electromechanical (MEMS) device for convenient usage.

1.7.2. Speckle Tracking. First presented in the paper of Chen et. al. (1997), speckle tracking is an interesting method that utilizes the speckle phenomenon, which in fact turns an undesired situation into an advantage. The amount of correlation is related to separation distance for consecutive frames. This correlation can be found by the Normalized Cross-Correlation (NCC) or Pearson Correlation Coefficient, which is in fact covariance of two data sets, normalized by sample standard deviations (Papoulis, 2002):

$$NCC = \frac{E[(I_1-\mu_1)(I_2-\mu_2)]}{\sigma_1\sigma_2} = \frac{1}{M}\frac{1}{N}\sum_{i=1}^{M}\sum_{j=1}^{N}\frac{(I_1(i,j)-\mu_1)(I_2(i,j)-\mu_2)}{\sigma_1\sigma_2} \qquad (27)$$

In here, I_1 and I_2 stand for the observed images. The mean and standard deviations of consecutive frames are denoted by the usual symbols $\mu_1, \mu_2, \sigma_1, \sigma_2$ and subscripts for the corresponding images with numbers. Speckle tracking scheme was implemented in this study for checking the in-plane assumption in freehand scan.

Mostly used for determining the separation in elevation, there is also correlation available for lateral and axial distance, reported in (Gee et.al., 2006). Since correlation fades away within large intervals, slight movements can be handled only, which is usually 2 mm in elevation direction. The speckle tracking procedure is illustrated in Figure 16. This figure also gives a hint about how pitch and yaw angle of the probe can be estimated; the image is divided into patches. Then, a line is fit via regression methods such as least squares for estimating the distance.

1.7.3. Volume Reconstruction. When each frame obtained is registered into its proper location, a global volume can be constructed for the related anatomy, in a uniform grid of proper size. Since the data is obtained freehand, there would be missing voxels due to irregular hand motion. These gaps can be filled with various reconstruction methods listed in Solberg et.al. (2011), such as Voxel Nearest Neighbor (VNN), where the nearest intensity value is assigned to missing voxel value or interpolating between 2D slice values. More sophisticated reconstruction procedure can be applied such as elliptical 3D kernels related to resolution cell of the system, (Solberg et.al., 2011) for smoother and more realistic transitions.

The output of reconstruction using speckle tracking is illustrated in Figure 15b. The volume is visualized in MITK, Medical Imaging Interaction Toolkit developed by German Cancer Research Association, (2019) environment. The ROI is healthy human thyroid.

1.8. In-Plane Registration of Ultrasound Images

The image registration is usually formulated as a target (anchor, reference) image that is to be kept still and a source image that is to be registered onto the target, according to selected techniques. The affine transform of an image includes translation, rotation, scaling and shear. Rigid transform can be stated as a subset of affine transforms which include only translation and rotation. Scaling and shearing include a deformation of volume, such that the model and optimization are more complex for a complete affine transform compared to rigid only motion. In affine transforms, parallel lines remain straight after transform. However, a subset of non-rigid transforms generally called elastic or curved, do not have such a constraint at all. They rather have constraints from their physical model or other geometrical fitting functions to control points. All those types of transforms mentioned are illustrated in Figure 17.

(a)   (b)
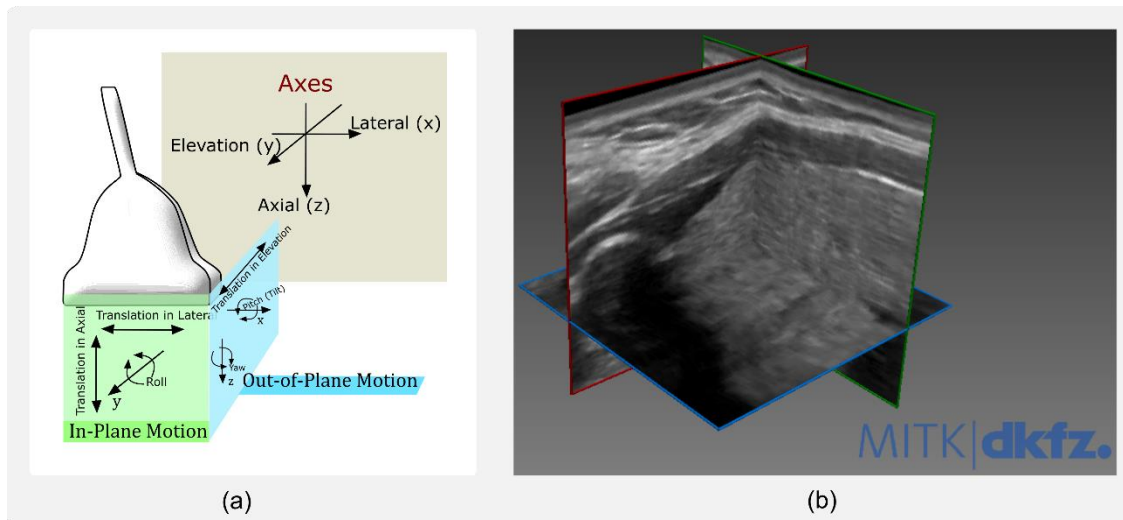
Figure 15: Ultrasound scan data in 3D (a) Illustration of scanning axes, in-plane and out-of-plane motion. Figure was previously published in (Cüneyitoğlu Özkul & Mumcuoğlu, 2018); (b) 3D Reconstruction of human thyroid using speckle tracking method, visualized using MITK, (2019).
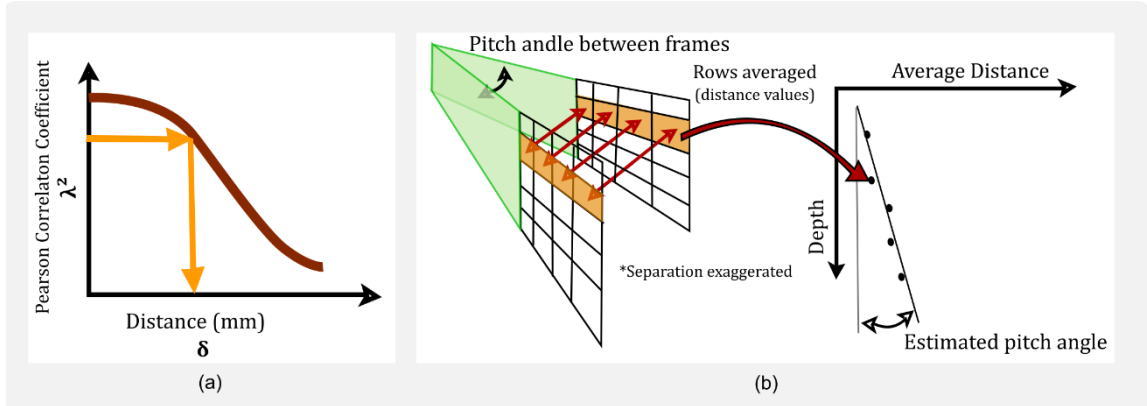
Figure 16: Speckle tracking scheme illustrated (a) Reading elevation estimate from speckle decorrelation curve; (b) Estimating pitch from the patches of the same rows. Yaw can be estimated from the patches of the same columns. Figures were previously published in (Cüneyitoğlu Özkul & Mumcuoğlu, 2018).

All of the transforms of source volume, mentioned here have the general form below, where $\vec{v}_t$ is target volume and $\vec{v}_s$ is the source volume in 3D vector notation from origin to center of the voxel and T is the transformation matrix:

$$\vec{v}_t = T\vec{v}_s. \tag{28}$$
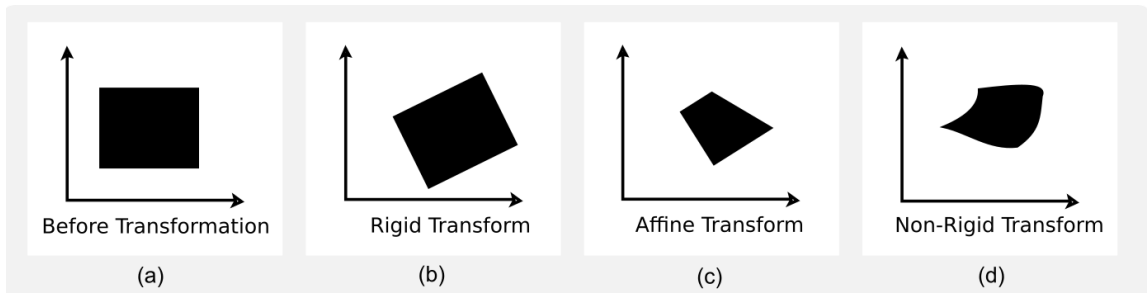
Figure 17: Types of transforms (a) Original image; (b) Result of rigid transformation; (c) Result of affine transform; (d) Result of non-rigid transform. Figures were previously published in (Cüneyitoğlu Özkul & Mumcuoğlu, 2018).

In ultrasonic imaging, a considerable amount of pressure is applied to tissue, in order to achieve good acoustic coupling, as stated in Section 1.2. For this reason, there is some amount tissue of tissue motion, due to the pressure applied. The layers of the tissue have highly varying amounts of stiffness (i.e. one layer may appear to be very soft and elastic and other may appear to be very dense and thick) combined with irregular geometry of tissue parts. Therefore, the subregions of ROI are compressed in a very complex manner,

25

depending on underlying tissue stiffness. Moreover, there is always slight motion due to patient movement and breathing. There can also be pulsatile motion, in case the ROI includes arteries.

In (Schneider et. al., 2012), for ultrasound, it is assumed that for a smaller field of interest, the transform can be considered as rigid. Since rigid transform has only few variables to determine, this is especially important for the real time applications. A rough estimate of symmetric matching is conducted based on the common features of source and target images and then, Random Sample Consensus (RANSAC) method is applied to obtain transformation matrix. This method (Fischler & Bolles, 1989), is based on geometry for removing outliers by applying least squares fit to randomly selected pairs of data. In the work of Banerjee et. al. (2015), no rotations are assumed for the search, only in-plane translations are considered as motion. In (Hossack et. al., 2002), a quaternion-based approach in 3D is applied to match two consecutive images based on image decorrelation. In (Vandewalle et. al., 2006), a rigid registration algorithm in frequency domain, based on Fourier transform properties on translation and rotation, for obtaining image shifts and rotations is proposed. The unaliased parts of the spectrum of the low-resolution images are used for registration.

Another interesting pair of studies involving rigid transformation (Treece et.al., 2002; Gee et.al., 2003), relates the amount of nonlinear warping of tissue to the motion of the scanning hand. In (Treece et.al., 2002), the optical tracker data is used to estimate out-of-plane motion under the assumption of the uniform elasticity of tissue during the scan. A rigid transform with rotation and translation is applied for in-plane motion. Making use of this, the probe pressure is corrected for each slide in elevation direction. In (Gee et.al., 2003), the orientation information obtained from the electromagnetic tracking device is used directly to correct the nonlinearity and then a rigid transform only including translation in 3 dimensions and assuming no rotation. This way, the time required for non-rigid transform that is computationally much more complex, is reduced.

In addition to rigid, affine transform based on similar points is a region of interest (ROI) called inliers are applied in Banerjee et.al. (2015). These inliers are selected as the points with minimum geometric distance when one-to-one correspondence between the points of selected regions of source and the target volume, the results are compared to the non-rigid registrations obtained from RANSAC (Fischler & Bolles, 1989) and elastix (Klein et. al., 2010). In (Krucker et. al., 2002), a sub-volume based, elastic transformation is applied (Liu et. al., 2013) with connectivity analysis with thin plate splines, which is a form of radial basis functions (Fitzpatrick et. al., 2008).

Insight Segmentation and Registration Toolkit (ITK) for medical applications is a cross platform software that has various registration methods in a built-in manner (Ibanez et.al., 2003) and further applications can be built upon the fundamentals presented by this package. To illustrate, elastix (Klein et.al., 2010), is an open source package for intensity-based registration, using ITK. A set of parametric non-rigid multiresolution, radial basis function based thin plate or B-spline approaches are available for input images. A physical

model related to the nature of the motion can be incorporated to the registration procedure. In the work of Blackall et.al. (2005), rigid registration is first applied according to the probe translation obtained from the optical tracker. After that, a non-rigid transform is applied for compensation of the respiratory motion model via B-splines. In (Lu et. al., 2010), a viscous fluid model is used for obtaining the displacement vector that employ conservation of mass, momentum and energy and form partial differential equations to be solved.

Block matching algorithm used in registration for medical applications is common (Cifor et.al., 2013; Banerjee et.al., 2015), for compensating the respiratory motion. A common block matching scheme contains a stationary and a moving window in for specific search purpose for the best match according to a predefined similarity metric. In (Mercier et.al., 2013), cross correlation with a 3D search window and is reported giving the best performance among all other metrics. In (Cifor et.al., 2013; Banerjee et.al., 2015), normalized cross correlation is used. Normalized mutual information metric is reported to be effective especially for volumes with small overlap (Cifor et.al., 2013; Banerjee et.al., 2015; Ijaz et.al., 2010). Mutual information is shown to be effective as a similarity measure for inter modality registration (Krucker et.al., 2002; Shekhar & Zagrodsky 2002), however it is costly to find joint histogram. Other metrics may be preferred for US to US registration. In (Ijaz et.al., 2010), another similarity metric called Kolmogorov's distance is used and compared with normalized mutual information. This is reported to be less effective compared to normalized mutual information. In this work, it is also stated that 32 histogram bins are the most efficient in calculating pdf for that particular application. Work by Morin et. al. (2015) employ Bilinear Deformable Block Matching scheme method used in elastography and bicubic interpolation to obtain sub-pixel accuracy.

In image processing and computer vision literature, a set of procedures are defined and very commonly used for finding the distinctive features that are resiliently invariant to changes of view in 3D, illumination and noise (Lowe, 2004). These features called SIFT features employ Difference of Gaussians which is in fact used as a band pass filter applicable to feature detection on varying scale spaces. SIFT features used in various 3D ultrasound volume registration studies (Ni et. al., 2009; Lu et. al., 2010; Schneider et. al., 2012). In (Ni et.al., 2009), the performance is improved by detecting both corners and blobs in the images. In (Schneider et.al., 2012), a feature symmetric matching with Euclidean norm of vector differences was used and RANSAC algorithm was implemented to remove outliers, using one scale space.

The Demons algorithm proposed by Thirion (1998), is a non-parametric, non-rigid registration method. In this method, the image displacement is modelled as a diffusion process based on optical flow methodology (Barron et. al., 1994) and this is introduced by regularization using simple Gaussian smoothing. In (Vercauteren et. al., 2009), the proposed method is improved further to provide an efficient non-parametric image registration algorithm based on diffeomorphic transformations. Having the diffeomorphic property means that the transformation operation (i.e. the operation applied in Equation (28)) and its inverse are smooth and differentiable.

In (Pennec et. al., 1999), the application of diffeomorphic demons algorithm, to medical field was examined in detail, especially in 3D ultrasound images. In this work, the main advantages of the of the algorithm was stated as being fast and effective. The improvement in segmentation performance was shown both on synthetic and real images. In selected works on ultrasound registration (Mellor & Brady, 2005; Liu et. al., 2013) variants of demons algorithm were proposed and implemented.

1.9. Bayesian Image Restoration

Image restoration, in general, aims to recover the effects of image degradation (blur and additive/multiplicative noise) that occurs in all imaging processes (Gonzalez & Woods, 2001). The blur may occur due to motion or due to imaging physics. As mentioned in section 1.5, the point spread function determines the imaging system resolution and therefore represents the image degradation. By applying various methods named as deconvolution in literature, the imaging blur is aimed to be reduced as much as possible (Campisi & Egiazarian, 2007).

There are blind and non-blind deconvolution methods in literature. In blind deconvolution, image degradation (PSF) is estimated simultaneously with the underlying tissue reflectivity. On the other hand, the non-blind deconvolution methods make use of estimated or measured PSF. Since the PSF is derived from the imaging system properties, generally more successful results are reported.

As a non-blind method, a typical image observation model can be expressed in matrix multiplication form using the following linear mathematical model similar to Equation (21):

$$\vec{y} = DB\,\vec{x} + \vec{n} \tag{29}$$

where $\vec{x}$ is the original high-resolution image, $\vec{y}$ is the observed image vector, B is the matrix modeling image degradation (resolution) in the form of convolution, D is the decimation matrix which represents high resolution (HR) to low resolution (LR) transformation, and $\vec{n}$ is the additive noise. For simplicity, the decimation and blur matrix in Equation (29) can be combined into a single matrix $A = DB$.

Bayesian image restoration is based on statistical modelling of the image formation process. Each pixel of the observed and ideal image is assumed to be a random variable, with the value drawn from a probability distribution. From the Bayes rule:

$$P(\vec{x}|\vec{y}) = \frac{P(\vec{y}|\vec{x})P(\vec{x})}{P(\vec{y})} \tag{30}$$

where the $P(\vec{x}|\vec{y})$ which is posterior image, given the prior $P(\vec{x})$ and the likelihood $P(\vec{y}|\vec{x})$. *Maximum likelihood* (ML) estimator is as follows:

$$\hat{x}_{ML} = argmax_{\vec{x}}P(\vec{y}|\vec{x}) \tag{31}$$

The likelihood function is assumed to be $(\vec{y} - h * \vec{x})$. When the values of this function are assumed to be drawn from a Gaussian distribution, the following expression can be formed, (Duda et. al., 2001):

$$P(\vec{y}|\vec{x}) = \frac{1}{\sqrt{2\pi}\,|C^{-1}|}\,exp^{-(\vec{y}-A\vec{x})^{T}C^{-1}(\vec{y}-A\vec{x})} \tag{32}$$

where C^{-1} is the inverse of sample autocorrelation matrix. The ML estimator can be expressed for Gaussian distributed likelihood function as follows:

$$\hat{\vec{x}}_{ML} = argmax_{\vec{x}}\left\{\frac{1}{\sqrt{2\pi}\,|C^{-1}|}\,exp^{-(\vec{y}-A\vec{x})^{T}C^{-1}(\vec{y}-A\vec{x})}\right\} \tag{33}$$

Since logarithm function is monotonically increasing, optima of the logarithm of any expression is the same as the optima of the original function. Therefore, maximizing the log likelihood instead of direct likelihood is a common practice (Duda et. al., 2001). The minus sign is eliminated by converting the maximization operation to minimization. Therefore, the ML estimate becomes (Elad & Feuer, 1997; Duda et. al., 2001):

$$\log(\hat{\vec{x}}_{ML}) = argmin_{\vec{x}}\{(\vec{y} - A\vec{x})^{T}C^{-1}(\vec{y} - A\vec{x})\}. \tag{34}$$

The output of this minimization operation is expected to deconvolve the observed image. However, ML Solution yields noisy results (Elad & Feuer, 1997; Duda et. al., 2001; Campisi & Egiazarian, 2007). For this case, when Bayes rule is considered, maximizing the posterior probability yields *Maximum a-Posteriori* (MAP) estimator:

$$\hat{\vec{x}}_{MAP} = argmax_{\vec{x}}P(\vec{y}|\vec{x})P(\vec{x}) \tag{35}$$

For selection of prior probability $P(\vec{x})$, *Markov Random Field* (MRF) assumption can be made (Rue & Held, 2005). This assumes the values of pixels in a defined neighborhood of one pixel (called cliques) are related locally. In this case, Gibbs distribution is obtained (Campisi & Egiazarian, 2007):

$$P(\vec{x}) = \frac{1}{Z}e^{-\gamma g(\vec{x})} \tag{36}$$

Here, $g(\vec{x})$ is named as *clique potential* and Z is a normalization coefficient. The clique potential can be defined as first norm (Michailovich & Adam, 2005; Michailovich & Tannenbaum; Alessandrini et. al., 2011):

$$g(\vec{x}) = \sum_{i=1}^{N}\sum_{j=1}^{8}\frac{|x_i - x_j|}{d_{i,j}} \tag{37}$$

where i index is for each pixel in the image, j is the neighbors of pixel i and $d_{i,j}$ stands for the distance between pixels i and j. This potential can be defined as second norm as well (Michailovich & Adam, 2005; Michailovich & Tannenbaum; Alessandrini et. al., 2011):

$$g(\vec{x}) = \sum_{i=1}^{N} \sqrt{\sum_{j=1}^{8} \frac{(x_i - x_j)^2}{d_{i,j}}} \tag{38}$$

Selection of either first or second norm as prior results in different restoration output. Second norm penalizes the local differences between pixels more, compared to first norm.

MAP estimate is obtained by involving $g(\vec{x})$ defined in Equation (38), as follows:

$$\hat{\vec{x}}_{MAP} = argmin_{\vec{x}}\{(\vec{y} - A\,\vec{x})^T C^{-1}(\vec{y} - A\,\vec{x}) + \lambda\,g(\vec{x})\}. \tag{39}$$

In here, λ is named as the prior coefficient and it determines the amount of regularization.

1.10. Super-Resolution Restoration

Super-resolution is restoring the information related to spatial frequencies higher than those readily available in the sampled image. The resolution of an imaging system depends on the diffraction phenomenon, which is explained briefly in Section 1.2. Super-resolution usually refers to recover information beyond diffraction limit of the imaging system. The minimum resolvable entity size is defined by the diffraction limit of the system and a system that is able to produce as good outputs as the theoretical limit defined by diffraction is called diffraction-limited, (Born & Wolf, 1999). In the case of ultrasound, the frames obtained represent the underlying anatomy, by noisy, blurred images with diffraction-limited resolution. In general, this limited resolution is referred to as *low-resolution* images and the *high-resolution* image is referred to an estimate of ideal image.

A general model for multi-image super-resolution can be stated as following (Elad & Feuer, 1997),

$$\vec{y}_k = D_k B_k T_k\,\vec{x} + \vec{n}_k \qquad\qquad 0<k<K \tag{40}$$

where $\vec{y}_k$ is the observed low-resolution image, D_k is a down-sampling matrix, B_k is a blurring matrix (that can be implemented in a space variant manner, if needed) as a result of PSF, T_k is a warping or transformation matrix which can either be rigid or non-rigid, $\vec{n}_k$ is imaging noise for kth observation and $\vec{x}$ the high-resolution image to be estimated (ideal image). This scheme is illustrated in Figure 18.

There are several ways to achieve multi-image super-resolution restoration according to the model proposed in Equation (40). The literature about ultrasound multi-image super-resolution is divided mainly into two main categories: *beamforming-based methods* and *motion-based methods*. Beamforming-based methods include obtaining different views from an ultrasound imaging in beamforming step. The selected ROI can be viewed many

times from varying angles by changing the active transducer elements and focusing scheme. This type of imaging requires access to beamforming scheme of the transducer, which was not available in our research.

Motion-based methods to make use of many noisy, blurred and low-resolution samples obtained from slightly different point of views. Such a set of images provide sufficient information for applying super-resolution (Elad & Feuer, 1997) were proven to be effective in video processing. A high-resolution image is to be obtained with the data provided from these samples.

Several other popular super-resolution algorithms are also present in literature, including (Papoulis, 1975; Gerchberg, 1974), Projection onto Convex Sets (POCS) (Youla, 1978), Iterative Back Projection (IBP) (Irani & Peleg, 1991), Robust Super Resolution (Zomet et. al., 2001), Normalized Convolution (Pham et. al., 2006). These algorithms make use of models different than Equation (40). The ultrasound applications of these methods are briefly mentioned in the following paragraphs.

1.10.1.   Beamforming Based Work. In this approach, the transformation matrix T_k in Equation (40) is determined for each view obtained from the applied focusing scheme. Depending on the transducer geometry, this matrix is calculated only once. In the work of (Taxt & Jirik, 2004), the first and the second harmonic signals were combined with the original image with a space variant deconvolution scheme in cepstral domain for PSF estimation. This estimate was then used for Wiener deconvolution. Second harmonic signal had less blur and noise and have different characteristics compared to first harmonic image, and had valuable information (Taxt & Jirik, 2004). Moreover, speckle pattern is different between two images which allows more efficient compounding results. The transducer elements in the probe were divided into two groups in receiving, which allowed imaging the slightly different directions.

O'Reilly & Hynynen (2013) applied super-resolution to aberration corrected low frequency (612 kHz center) intracranial ultrasound imaging, for better resolution of microbubbles in blood flow. Frames were obtained for different focal areas by systematically changing the transmit focus and a volume is reconstructed with 440 frames. 3D Gaussians were fitted to observed microbubbles within an uncertainty limit.

In (Ellis et. al., 2010), Diffuse Time-domain Optimized Near-field Estimator (dTONE) was used to model the scatterer points as diffuse sources. In this method, random hypothetical targets were assumed in the ROI. For each target, a hypothetical spatial impulse response was calculated and the results were involved in a MAP scheme by solving for real target positions and amplitudes, given the observed images. dTONE algorithm was proposed as an adaptive beamforming algorithm that was designed for medical ultrasound. Adaptive beamforming algorithms reduced the undesired effects of interference by weighting of the off-axis signals. The weighting and delaying scheme in dTONE was determined by the response obtained for each hypothetical target.

In (Labyed & Huang, 2013), the transducer elements' phase response was examined and a phase coherent pseudospectrum that reduces noise was calculated. Multiple Signal Classification (MUSIC) algorithm based on singular value decomposition of interelement response matrix, is applied. With the proposed phase coherent MUSIC method, the phase response of transducer elements was utilized to obtain super-resolved image. This phase response was obtained experimentally. In (Huang et. al., 2013), impressive results on breast microcalcifications with the proposed PC-MUSIC method were presented. In all of these works, the ultrasound probe was held stationary and no motion was considered.

In the studies (Clement & Hynynen, 2004; Clement et. al., 2005), a backprojected reconstruction method was proposed. First, an initial guess about the size and the location of the object to be imaged was made. The source's size, location, magnitude was inferred with an iterative procedure by convolving it with the undisturbed field that was measured a-priori. Many such guesses images were convolved with the prior measurement to form candidate images. The image having the spectrum that matched to the uncorrected image

most was accepted among all these candidate images, which was obtained by an optimization procedure. This method was applied to only objects at focus. The undisturbed beam and the transfer function were assumed to be known for the related frequencies. The slight movements between undisturbed and the observed images were corrected by autocorrelation. In the work of Tsakalakis (2015), a transducer array was designed in Field II simulator (Jensen & Svendsen, 1992; Jensen, 1996). Frenquency and spatial based multi-image super-resolution was applied to those synthetic images and improvement in image quality was reported.

A different point of view was proposed by Parker (2012), for digitally sampled ultrasound signals. An excitation pulse that was stable and invertible with respect to Z transform was used. This way, the received echoes were able to be inverse filtered by applying deconvolution. Initially, the results were tested on synthetic Field II images (Parker, 2012). This method was then applied to pulses in lateral direction only (Chen & Parker, 2016). Finally, the received signal was modelled as separable for axial and lateral directions and 2D stabilized inverses were defined under some assumptions (Chen & Parker, 2017). The improvement in resolution is notable, however, there is the drawback of increased speckle variance.

1.10.2.   Motion Based Works. Estimation of motion introduced by the freehand probe transformations or by tissue movement such as cardiac cycles or respiration, is an integrated part of this type of super-resolution approach (Irani & Peleg, 1991; Elad & Feuer, 1997). In the study of Nandi & Mukhopadhyay, (2011), the probe motion was simulated with a sine function. The proposed radial super-resolution algorithm was applied to polar images before scan conversion, corrupted with different types of noise.

The works of Morin et.al., (2015) a delicate motion estimation with bilinear deformable block matching, followed by interpolation to a high-resolution grid by cubic interpolation and deblurring was stated as a super-resolution approach. However, deblurring was not

implemented in the proposed paper. In Morin et.al., (2015) and Morin et.al., (2012), there was only registration and sub-pixel interpolation applied. The aim was to obtain high resolution data and contrast to noise ratio improvement. In (Morin et.al., 2013), a total-variation based minimization procedure was implemented. In this work, a space invariant blur function was stated to be used for simplicity.
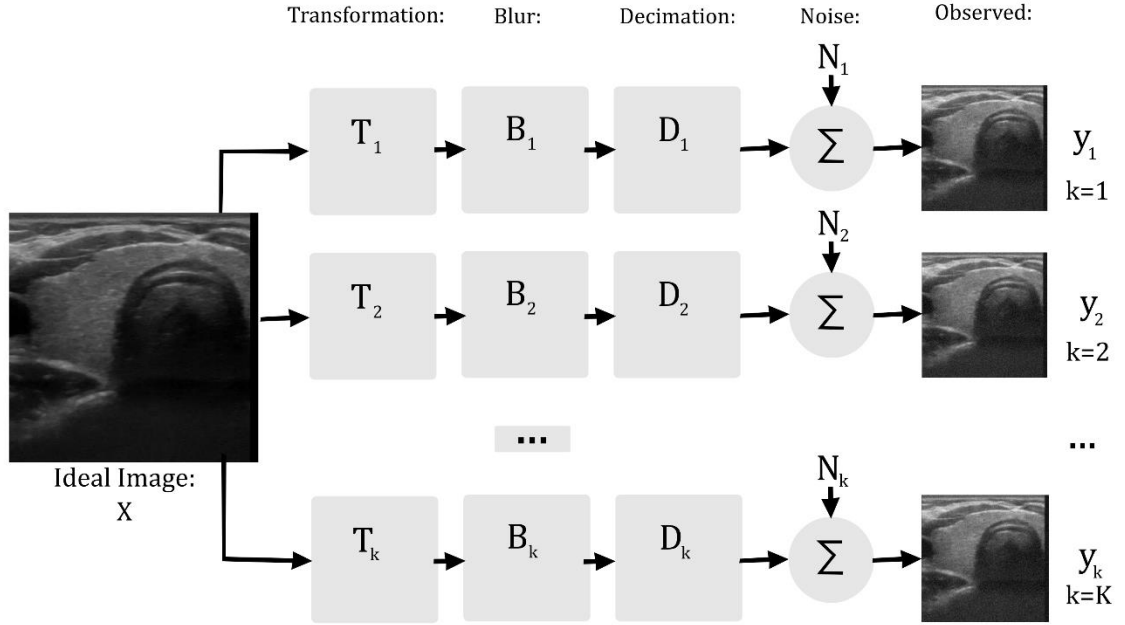
Figure 18: Super-resolution scheme with model presented in Equation (40). Figures were previously published in (Cüneyitoğlu Özkul & Mumcuoğlu, 2018).

Wu et. al. (2014), make use of normalized convolution applied to super-resolution (Pham et. al., 2006) which was a method based on projections onto a set of basis functions, mostly polynomials, for irregularly sampled data. Tissue was compressed and recorded frames are divided into patches for rigid registration in frequency domain by method of Vandewalle et.al. (2006). In this work, first frequency compounding, then super-resolution applied and this process was reversed. Overall improvements reported, both in terms of CNR and visually, with no significant difference in application order. Strain was measured from obtained videos and compared to motion estimation results from super-resolution.

Wang (2009), made use of robust super resolution method proposed by Zomet et.al. (2001). In these study, rigid registration by Vandewalle et.al., (2006) was used with

Gaussian kernel for deblurring. MAP approach was applied for $P(\vec{x}|\vec{y}_k)$ for k^{th} observation with Gaussian noise with zero mean. The ultrasound resolution cell was assumed equal at all depths. Synthetic images were created by convolution, one in vivo image shown for demonstration. Super-resoloution was shown to be effective on ultrasound images, compared to speckle filtering with reduced granularity in images.

There was some commercial interest in medical ultrasound super-resoloution as well. In Wang et. al. (2014) with the original assignee being Siemens Aktiengesellschaft, a wavelet based super-resoloution approach was patented to be useful in several modalities including ultrasound, MRI and CT in general. Wavelet representation of images provided sparsity and multiresolution by representing the signal in different wavelet bases. Ultrasound specific super-resolution patents by Hitachi Medical Corporation and Hitachi Aloka Medical (Kotaki et. al., 2011; Baba, 2013) proposed to make use of iterated backprojection in real time image formation.

Yang et. al. (2009), applied anisotropic diffusion (Perona & Malik, 1990) as regularization term for super-resolution. PSF was estimated with homomorphic transformation and then, a restoration scheme was applied. In Yang (2004), rigid registration and Huber Markov random fields for regularization were used. In (Yang et.al., 2006; Yang et. al., 2009) and in MIAMI Fuse software (Meyer et. al., 1997) affine and thin plate spline-based registration were preferred.

All of the above-mentioned medical ultrasound super-resolution studies are listed in Table 1. The related details of all the mentioned super-resolution methods are explained in Methods Chapter.

Table 1: Most of the works including super-resolution in medical ultrasound are listed.

	Data	SR Method	Probe Motion and Registration Algorithm	Blur Model and Deconvolution Scheme
Taxt & Jirik (2004)	3 clinical datasets with first & second harmonic images, obtained from kidney, heart, and pancreas	2D homomorphic PSF estimation, Wiener deconvolution	Through beamforming	PSF estimated in complex cepstrum , WF within each patch for first and second harmonics separately
Clement & Hynynen (2004), Clement et.al. (2005)	Phantom with nylon wire and human hair	Backprojected reconstruction method is proposed	Through beamforming, autocorrelation used for correction of undesired, slight movements	Transfer function for nondissipative, homogenous medium estimated
Ellis et. al. (2009) dTONE	Synthetic US images produced by DELFI ultrasound simulation tool, Ellis (2007), 100 realizations of white noise added	Proposed dTONE algortihm, based on a MAP estimation technique with a well-defined system model. Able to work with single realization of data.	Through beamforming	Diffuse target model in a 5×5 non-overlapping region
Parker (2012) Chen & Parker (2017, 2018)	Synthetic images with random scatterers resulting in Rayleigh statistics for conventional pulsed ultrasound	Inverse filter based approach is proposed	Through beamforming	Convolution model is not used, an invertible stable pulse is used for excitation

Table 2 - Continued: Most of the works including super-resolution in medical ultrasound is listed.

Reilly et. al. (2013), Hynynen et. al. (2013)	440 images captured through the ex-vivo human skull to form volume	Gaussian fitting, maximum pixel projection	Through beamforming	3D Gaussian
Tsakalakis (2015)	2D images, 3D volumes generated with Field II	Weighting based method proposed	Through beamforming	PSF calculated from Field II simulations
Yang (2004), Yang et. al. (2007), Yang et. al. (2009)	4 in-plane images with slight motion	Diffusion SR reconstruction, MAP based, pixel compounding	Only in-plane motion, rigid registration Yang (2004), Yang et. al. (2006) 3D registration MIAMI Fuse Meyer et.al. 1997, in Yang et. al. (2009)	PSF estimated with homomorphic transformation
Wang et. al. (2009)	Synthetic image created by convolution, one in vivo image shown for demonstration	MAP based with anisotropic diffusion term for regularization, Robust super-resolution, the method proposed by Zomet et.al. (2001)	Rigid registration, Vandewalle et. al. (2006)	Gaussian kernel
Nandi & Mukopadyay (2011a), (2011b)	Simulated motion with a sine function, polar images before scan conversion, corrupted with different types of noise	Radial superresolution (2011b)	Known motion for simulated images	Not mentioned
Kotaki et. al. (2011)	Presented as an invention applicable to real time scan conversion process	Iterated backprojection with stabilization terms	Any optical flow algorithm	Not mentioned
Morin et. al. (2012a), (2012b), (2013), (2015)	1-15 Synthetic images with Field II (2015), (2012a),(2013) 2-15 in vivo thyroid images with a malignant tumor delineated by a specialist (2015), (2012a)	Motion estimation followed by image reconstruction and deblurring (2015), (2012b)	Non-rigid: Bilinear Deformable Block Matching (2015), (2012a)	Found in an iterative manner with total variation minimization approach and alternating direction method of multipliers for solving the optimization equation (2012a),(2013)
Labyed, Huang et. al. (2013a) (2013b)	1-Tissue mimicking phantoms for measuring phase response and validating the proposed method, (2013a) 2-Clinical study on breast tissue with microcalcifications, (2013b)	Phase Coherent Multiple Signal Classification (PC-MUSIC Method) is proposed	No motion (Impulse response based approach)	Impulse response calculated for transducer elements' surfaces
Baba et. al. (2013)	Presented as an invention applicable to real time scan conversion process	Iterated backprojection	Cross-correlation based block matching between adjacent frames	Not mentioned
Wu et. al. (2014)	4 Frames are used to get HR image	Normalized convolution by Pham et.al. (2006)	Rigid registration, Vandewalle et. al. (2006)	Total variation based, Pham et.al. (2006)

1.11. Image Quality Assesment

There are two types of visual grading in the literature: *Visual Grading Analysis* (VGA) (Shin et. al., 2018; Månsson, 2000; Magnus et. al., 2008) and *Image Criteria* (IC) (Månsson, 2000). In both methods, the scores are summed and averaged. VGA contains some scale of points given to an image, whereas, IC involves yes/no questions only. VGA

can be conducted in a relative or absolute manner. In absolute VGA, the experts are randomly exposed to images and rate their quality with a scale (i.e. 1-5 from very bad to very good), (Shin et. al., 2018; Månsson, 2000; Magnus et. al., 2008). In relative VGA, an image is compared with a reference image using the following scale:

- Clearly inferior to (-2)
- Slightly inferior to (-1)
- Equal to (0)
- Slightly better than (+1)
- Clearly better than (+2)

For the same reference image, different algorithms and / or parameters can be applied and the results can be evaluated using ANOVA. In relative VGA, ROC curves can also be formed based on success rates (Magnus et. al., 2008).

In image criteria (IC) evaluation, yes/no questions are prepared for the image set. The obtained results are stated to be more reliable in terms of statistics (Månsson, 2000). As the sample size is increased, the results are guaranteed to approach to the mean.

The type of questions and the methodology is well-defined in CT or MR imaging. There are pages of EU guidelines or British standards available. However, for ultrasound imaging, although there are samples of such evaluations (Tinberg, 2000), to the best of our knowledge, there are no common standards defined.

1.12. Aims and Scope of the Thesis

In this thesis, the aim was to improve diagnostic ultrasound image quality, by means of Bayesian multi-image super-resolution. In order to back up the findings of the study, objective evaluation criteria such as improvement in contrast to noise ratio (CNR) was used. This is to be supported by analyses that reflect usefulness of the applied algorithms in clinic, such as VGA.

The blurring effect of imaging system was modelled as accurately as possible by measuring PSF. Examination of effects of spatial correlation is an essential part of this thesis. The spatial correlation is measured experimentally, and the statistics is assumed to be Gaussian. The other models that are mentioned above (Rayleigh, Rician, Nakagami, RiIG) assume the probability distribution of speckle to be independent and identically distributed (IID). Forming a model that involves correlation requires quite challenging set of mathematical operations. Gaussian distribution was used for simplicity.

Amount of speckle decorrelation was also measured in elevation direction and the result of this study was used to check in-plane assumption of multi-image data. In this thesis, the methods mentioned were applied to 2D images only, in order to observe the effect of

spatial correlation in single-image Bayesian restoration and multi-image Bayesian super-resolution.

The success rates were especially focused on for targets of various sizes. This is an important aspect, since the tissue that is required to be imaged usually contains targets of various size and echogenicity. For this reason, a controlled testing and objective evaluation scheme was implemented. Later on, the results were backed up by radiologists' evaluations as well.

CHAPTER 2

2. METHOD

2.1. Data Collection

All the B-Mode ultrasound data was collected from Department of Radiology, TOBB-ETÜ Hospital. In this work, 2D image processing using in-plane images was implemented. Collected images were used for measuring the system parameters such as PSF and autocorrelation matrix.

2.1.1. Image Parameters. All of the 2D ultrasound images were acquired from GE Logiq P6 ultrasound system, using 11L linear probe and the focal depth adjusted to 20 mm. All of the targets were selected as superficial tissue, for simplicity and preliminary validation. Acquired images were from 40x40 mm area, but depending on ROI, images were clipped (i.e. parts with no data). Images approximately around 200x200 pixels were processed. When the ultrasound image scale was converted into pixels, one pixel corresponded to 90 µm in axial and lateral directions. All the relevant details related to image acquisition are listed in Table 2.

Table 3: Imaging System Parameters

GE Logiq P6	
Probe:	11L
Type:	Linear
Focal Depth:	20 mm
Imaging Area:	40x40 mm
Processed Image Size:	200 x 200 px. (approx.)
Format:	wmv
Frame Rate:	30 fps
Centre Frequency:	13 Mhz

2.1.2. In-Plane Movement and 2D Data Collection. For 2D multi-image super-resolution, in-plane assumption was made, therefore the acquired images were supposed to remain in-plane, as much as possible. The probe was moved laterally to be in-plane axis. Consecutive video frames were collected with freehand motion (5 images from ROI selected from cine loop). To avoid motion blur and not to violate the in-plane assumption, the freehand movement was slow and controlled. The in-plane assumption was verified using speckle-tracking methods. The details can be found in Section 2.2.

2.1.3. Tissue-Mimicking Phantom Data. For PSF measurement, "Multi-purpose multi-tissue" CIRS-040GSE tissue-mimicking resolution phantom was used (Figure 19). Later on, for objective evaluation of some algorithms, CIRS-044 tissue-mimicking resolution phantom was available (Figure 20). Tissue-mimicking phantoms are usually made of Zerdine material (Zerhouni & Rachedine, 1990). Speed of sound is 1540 m/s for this material. The resulting US image is speckled and quite realistic.

These particular box-shaped phantoms are usually used for periodic checking and calibrating the resolution of ultrasound machines that are used in clinic. They have geometric targets with various echogenicity and size, placed in known locations. As observed in Figure 19b and Figure 20b, the echogenicity of the background is very heterogenous like real tissue and its mean value varies considerably.
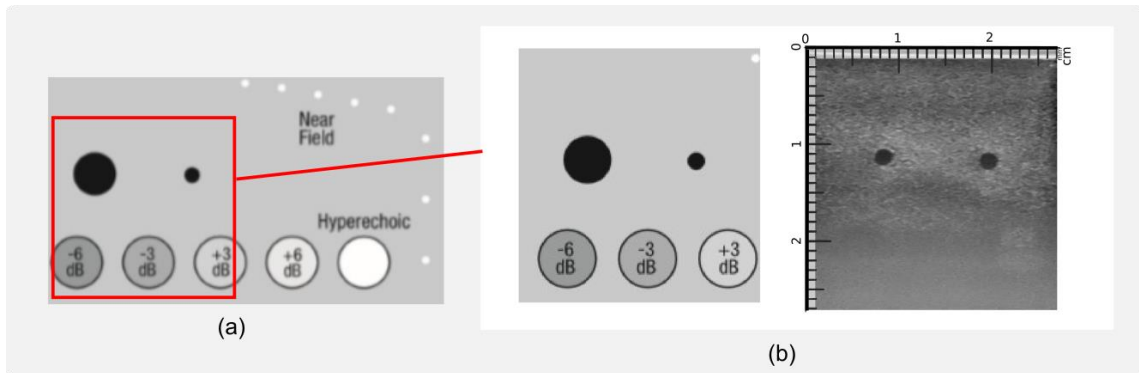
Figure 19: Tissue-mimicking resolution phantom CIRS 040GSE (a) Drawing of all imaged area from CIRS Tissue Simulation & Phantom Technology (2019); (b) Selected 300x300 pixels (27x27 mm) region from acquired images. The radii of the anechoic targets are stated to vary along elevation, this is why the target to the left side differs from drawing.

Both of the phantoms contain high echogenicity (>15 dB) nylon wires of 80 µm diameter (seen on Figure 20b). Anechoic targets appearing as black circular shaped in Figure 19b in CIRS 040GSE phantom are stepped cylinders. Their diameters vary between 1.3 - 10.0 mm. The anechoic and hyperechoic targets in CIRS 044 (Figure 20b) have 2 mm diameter.

In addition to tissue-mimicking resolution phantoms, data was also collected from multi-modality biopsy and sonographic trainer breast phantom (CIRS 073). Sample images obtained from this phantom are illustrated in Figure 21. It contains hyperechoic spherical (Figure 21a), 10-15 anechoic cystic (Figure 21b) spiculated targets and 100-300 micrometer microcalcifications (Figure-21c).
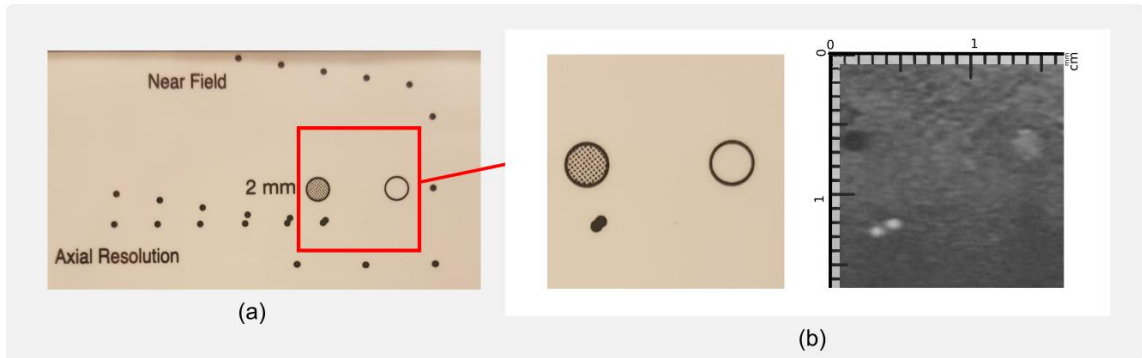
Figure 20: Tissue-mimicking resolution phantom CIRS 044 (a) Picture of imaged area; (b) Selected 180x180 pixels (16.2x16.2 mm) region.
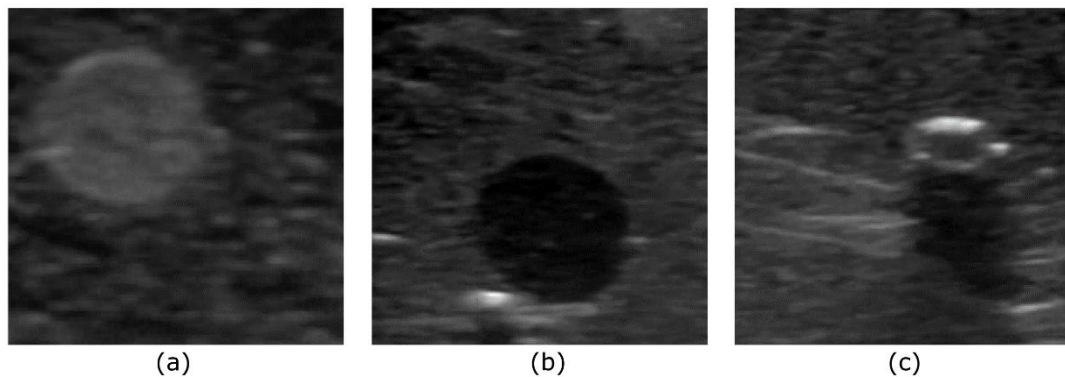
Figure 21: Tissue-mimicking breast phantom CIRS 073 (a) Hyperechoic spherical; (b) 10-15 anechoic cystic; (c) 100-300 micrometer microcalcifications.

2.1.4.   Human Data. Informed consent from all volunteers and written permission of TOBB-ETÜ Hospital was taken for all of the mentioned work. The 2D scanned body parts are listed as follows:

- Thyroid with moderate Hashimoto's thyroiditis condition
- Glands with systemic lupus erythematosus
    o Submandibular gland
    o Parotid glands
    o Lymph nodule

41

- Healthy hand tendon

The images are presented in Figure 22.
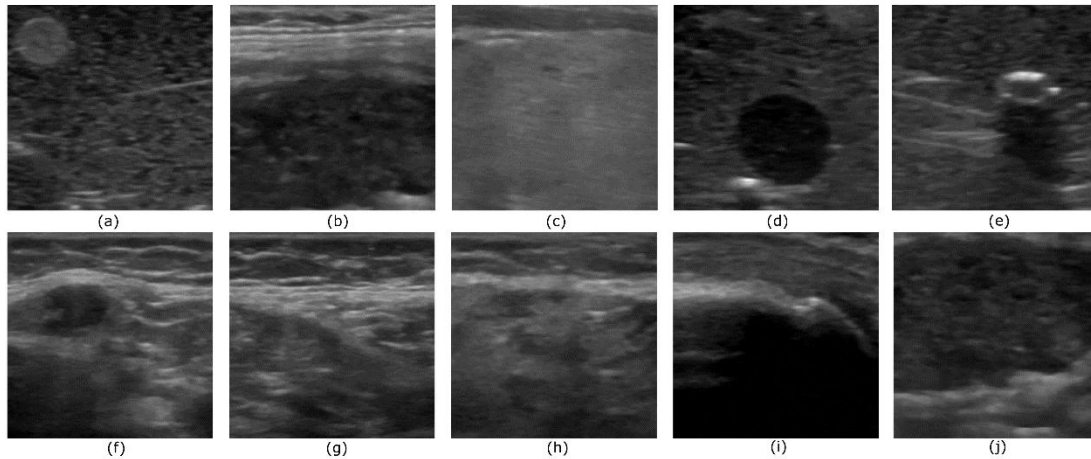
Figure 22: B-Mode images collected from volunteers (a-d-e) Breast phantom; (b-c-j) Human thyroid; (f) Human lymph nodule; (g) Human submandibular gland; (h) Human parotis gland; (i) Human hand tendon.

2.1.5.   Data Preparation. The recorded videos contain ruler and gray level scale information. 450x450 pixel B-mode image area with tissue data was extracted from recorded videos. Video frames contain red, green and blue channels which have the same value; therefore, the output image is always a gray level tone and the color information is redundant. The channel information was compressed into one gray level value. The acquired wmv data is signed integer [0,255], this was converted to floating point data in the range [0,1] with single precision. The 2D image data was saved as MATLAB® matrices with appropriate naming convention.

2.2. Speckle Tracking

In order to implement the speckle tracking scheme mentioned in subsection 1.7.2, a precise mechanical setup was designed. This setup was used to scan the tissue-mimicking phantom along elevation. After this step, the decorrelation curve was measured.

2.2.1.   1D Scanning Mechanical Setup. In order to measure the system specific decorrelation and estimate resolution cell size in elevation, a robust mechanical setup with one degree of freedom was used. This system was first designed as a solid model (in Solidworks® 2008). Shown in Figure 23a, probe holder part (marked red) was manufactured using 3D printer.

The overall system was designed to minimize the moment arm between the actuator and the touching point of the phantom with the surface of the transducer probe where the force was applied. The accuracy of 10 μm was a challenging task, and could be easily lost due to mechanical vibrations with movement. The unwanted mechanical vibrations were mostly expected to occur due to improper mounting. In order to reduce friction, the bridge height could be adjusted easily with T-shaped nuts sliding inside sigma profile canals. The overall assembling was made with spring nuts which also improved rigidity. MODESIS company also provided extensive aid on manufacturing process. The manufactured system is shown in Figure 23b. Overall setup installed in TOBB-ETÜ Hospital Radiology service is shown in Figure 24.
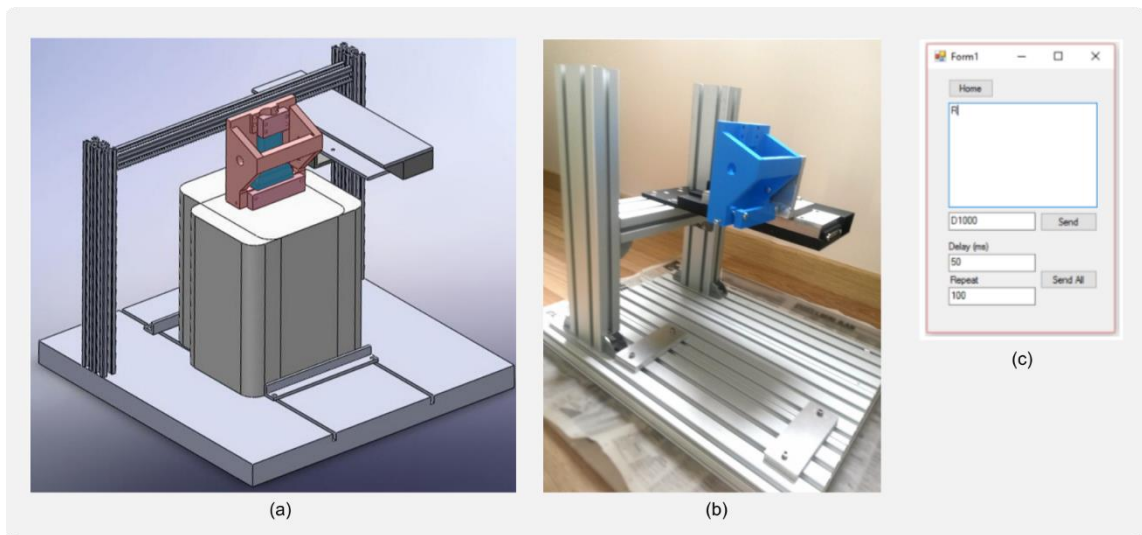
Figure 23: The designed system for 1D scanning (a) Computer aided design of 1D scanning system in Solidworks® 2008 environment – Red part: 3D printed probe holder, blue part: ultrasound probe, white box: bounding box for tissue-mimicking phantom; (b) Manufactured and assembled system; (c) Simple control interface program written in C#.

Ultrasound probe was mounted rigidly on the setup. The system was controlled by a software interface (shown in Figure 23c) that moves the probe at given constant intervals in milliseconds. The precise linear actuator made calibration moves with the limit switch at home position (0 position) at each data acquisition sequence. The moves for calibration were oscillatory (back and forth) around the 0 position and the actuator movement converged to the desired position.

The mechanical setup was able to produce precise motion of 10 μm which allows to plot a finer correlation graphic. The data from the ultrasound system was recorded as video. The calibration movement mentioned above was distinct in the videos. After the calibration move, the constant step movements with 10 μm step size started. Since there

43

was no absolute position, the video frames were extracted as soon as the constant movement was started. The frame rate was 30 for the ultrasound system and was given constant intervals of 100 ms, there were 3 frames obtained for each position.
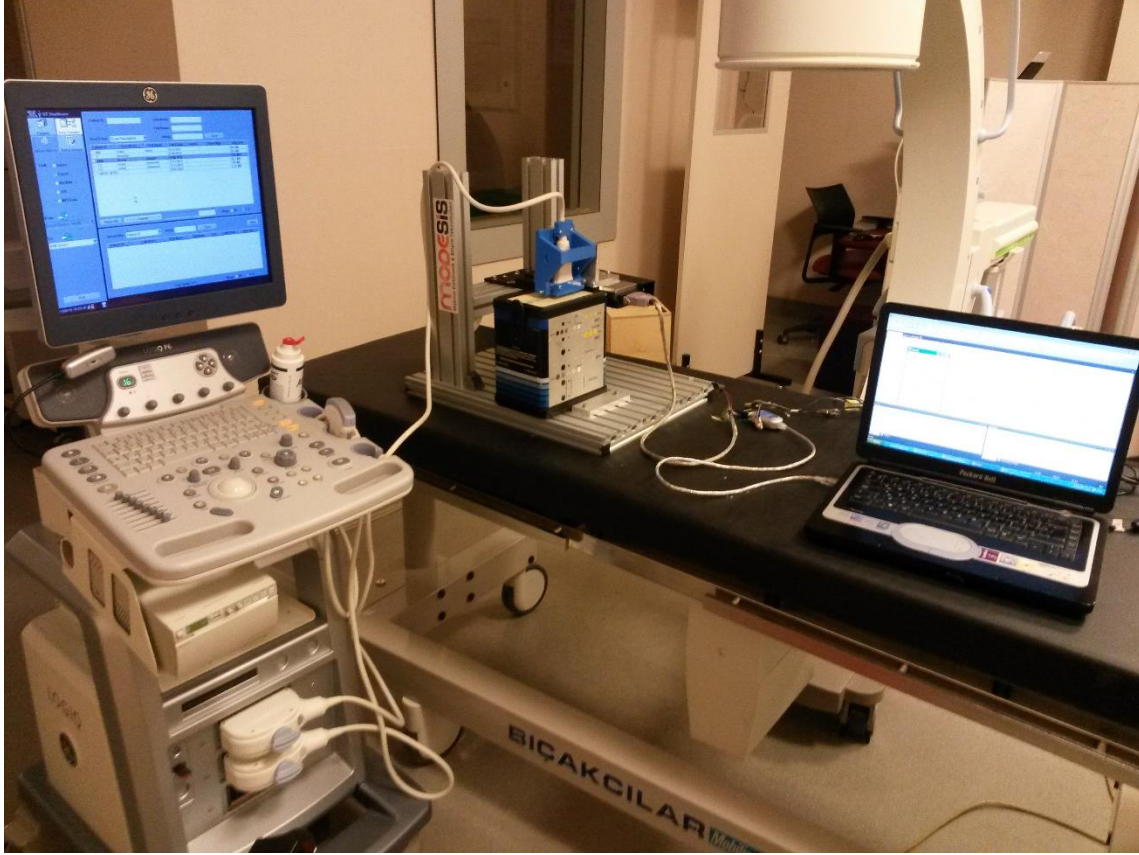
Figure 24: 1D Mechanical scanning setup installed in TOBB-ETÜ Hospital, Department of Radiology.

2.2.2. Algorithms and Measurements. As stated previously, the correlation of consecutive frames was estimated via the Pearson correlation coefficient, given in Equation (27).

There is also a theoretical model available for expressing the correlation of two consecutive slices. Since the correlation of two frames is due to speckle, the correlation coefficient is stated to be expressed using Rayleigh statistics (Wagner et. al., 1983; Gee et. al., 2006). The theoretical Rayleigh correlation is found by:

$$\lambda^2 = \exp^{\left(\frac{-\delta^2}{\sigma^2}\right)} \tag{42}$$

In this expression, λ^2 stand for the theoretical correlation value, δ is the distance between consecutive frames and σ is the resolution cell size.

If the distance between measurements is fixed and known, with equating the sample correlation value obtained from equation (27) to λ^2 value in equation (42), the resolution cell size (σ) that varies with depth can also be estimated. 50x50 patches were extracted (as shown in Figure 25) from the data collected from speckle-only areas of the tissue-mimicking phantom, using the above-mentioned 1D mechanical scanning setup (from 6.75 mm to 24.75 mm depth). The average of 5 patches were used for measurement of correlation for each row. The decorrelation measured at every 10 μm with respect to first frame is plotted in Figure 26. The average resolution cell size σ was found to be 0.26 mm. The Rayleigh correlation corresponding to this σ is shown with dark blue solid line in Figure 26.

In (Afsham et. al., 2014), the theoretical correlation in elevation from a more complicated data model called "Rician of Inverse Gaussian distribution" was derived, which was claimed to fit ultrasound data better. Their results seem considerably better compared to other works in literature. This model had been discussed and examined for some time in earlier stages of the thesis, but a simpler model was found to be adequate, for both speckle tracking and restoration purposes.
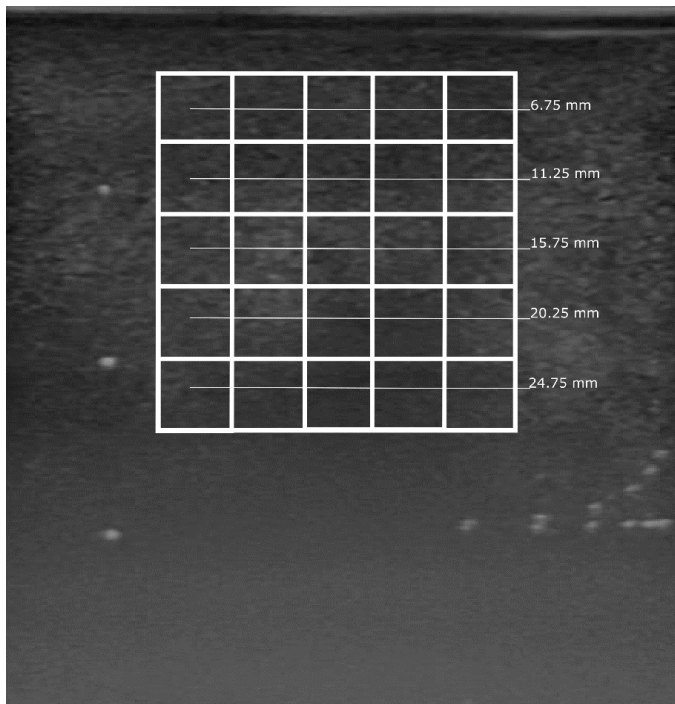
Figure 25: Patches extracted from speckle-only areas of the tissue-mimicking phantom.

2.3. Bayesian Restoration and Super Resolution

In this work, single-image Bayesian restoration and multi-image Bayesian super-resolution methods were implemented on 2D B-mode ultrasound. In this procedure, correlated Gaussian assumption was used for noise (speckle). A single-image Bayesian restoration scheme (BR-CG) as well as a Bayesian multi-image super-resolution restoration scheme are proposed (BSRR-CG).
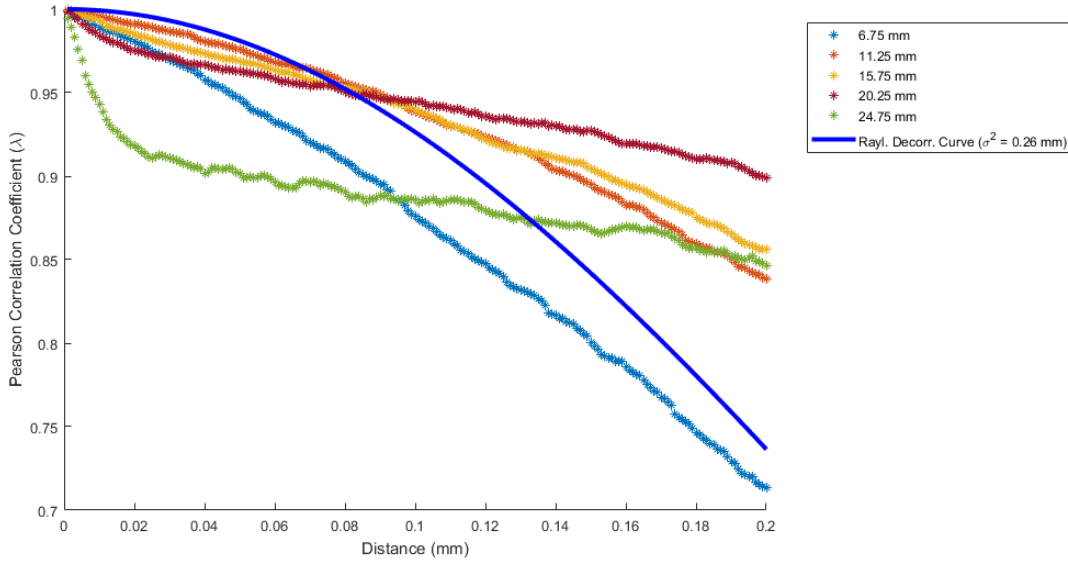
Figure 26: Speckle decorrelation curve measured for Logiq P6 system, using the 1D mechanical scanning setup.

2.3.1. Single-Image Restoration. The image model given in Equation (29) can be implemented using a Bayesian scheme. BR-CG method can be implemented using an appropriate C matrix for spatial correlation. In this work, the spatial correlation was assumed to be Gaussian and measured experimentally as sample autocorrelation matrix, as details explained in Section 2.4. Gaussian probability density function in Equation (32) is compared to the sample histogram of ultrasound speckle acquired from B-mode imaging system. It was considered due to its simplicity for modelling spatial correlation, although it does not fit exactly (shown in Figure 27). The results were compared to BR-UG method, the case with no spatial correlation (C matrix being identity).

2.3.2. Multi-Image Super-Resolution Restoration. As mentioned in Section 2.1, there were multiple images acquired from ROI for both in-plane and out-of-plane movement of

46

the ultrasound probe. In order to implement a multi-image scheme, the K observations are inserted into matrix form and the following expression is obtained (Elad & Feuer, 1997):

$$\begin{bmatrix} \vec{y}_1 \\ \vec{y}_2 \\ ... \\ \vec{y}_K \end{bmatrix} = \begin{bmatrix} D_1 B_1 T_1 \\ D_2 B_2 T_2 \\ ... \\ D_K B_K T_K \end{bmatrix} \vec{x} + \begin{bmatrix} \vec{n}_1 \\ \vec{n}_2 \\ ... \\ \vec{n}_K \end{bmatrix} = \begin{bmatrix} A_1 \\ A_2 \\ ... \\ A_K \end{bmatrix} \vec{X} + \begin{bmatrix} \vec{n}_1 \\ \vec{n}_2 \\ ... \\ \vec{n}_K \end{bmatrix} \quad 0 < k < K \quad (41)$$

where the number of rows is K times that of the single-image case and $A = D_k B_k T_k$ for simplicity.

In Section 1.10, multi-image Bayesian super-resolution works using the model in Equation (39) were mentioned. The spatial correlation of speckle was not involved in those works. In this study, using identity C matrix method is abbreviated as BSRR-UG and compared to proposed method with spatial correlation involved, namely the BSRR-CG method. The minimization problem stated in Equation (39) was solved for multiple images.

2.4. Application of the Methods

In order to implement Equation (39), measurement of imaging system blur and autocorrelation are required. The details regarding those measurements are stated in the following paragraphs. Then, the optimization scheme is explained.

2.4.1. Measurement of Point Spread Function. PSF was estimated using the tissue-mimicking phantom by implementing the *image observation method* (Gonzalez & Woods, 2001). A small sub-image was extracted from tissue-mimicking phantom with the known simple structure (80 µm diameter hyperechoic nylon wire with point cross-section, see Section 2.1 for details). The PSF was assumed to be invariant along the image and through the depth. Its Fourier transform $H_s(u, v)$ was estimated by

$$H_s(u, v) = \frac{G_s(u,v)}{\hat{F}_s(u,v)} \quad (42)$$

using Fourier transform $G_s(u, v)$ of the observed degraded image. The ideal image estimate was $\hat{F}_s(u, v)$ which was expected to be one-pixel dot with amplitude higher than 15 dB) and this was converted back to spatial domain.

The cross sections from resulting PSF is shown in Figure 28. FWHM is marked with blue lines. It is observed that the tails do not approach to zero. Assumed PSF is marked using

47

red lines. Red lines along axial are 4 pixels away from peak. Red lines along lateral are 9 pixels away from peak. This corresponds to 0.72 mm extent of PSF along axial and 1.62 mm extent along lateral. Trimming the PSF sharply is expected to result in heavy artifacts in deconvolution operation. The end values of the assumed PSF are approximately 1/3 of the peak value. The effect of longer extent or filling the end of PSF smoothly was examined briefly using the image restoration code. No significant change was observed between restoration results with slightly different PSFs (PSF with longer extent and with smooth ending to zero value). For this reason, the observed PSF with the given extent was taken as is.

Along elevation, there are no structure changes for imaging, since the nylon point targets are in fact cylindrical. For this reason, a Gaussian PSF shape is estimated based on correlation measurement in elevation. PSF extent along elevation is estimated as 37 pixels (3.33 mm). The 3D point spread function estimate is visualized as a 3D volume in Figure 29, using MITK, (2019).
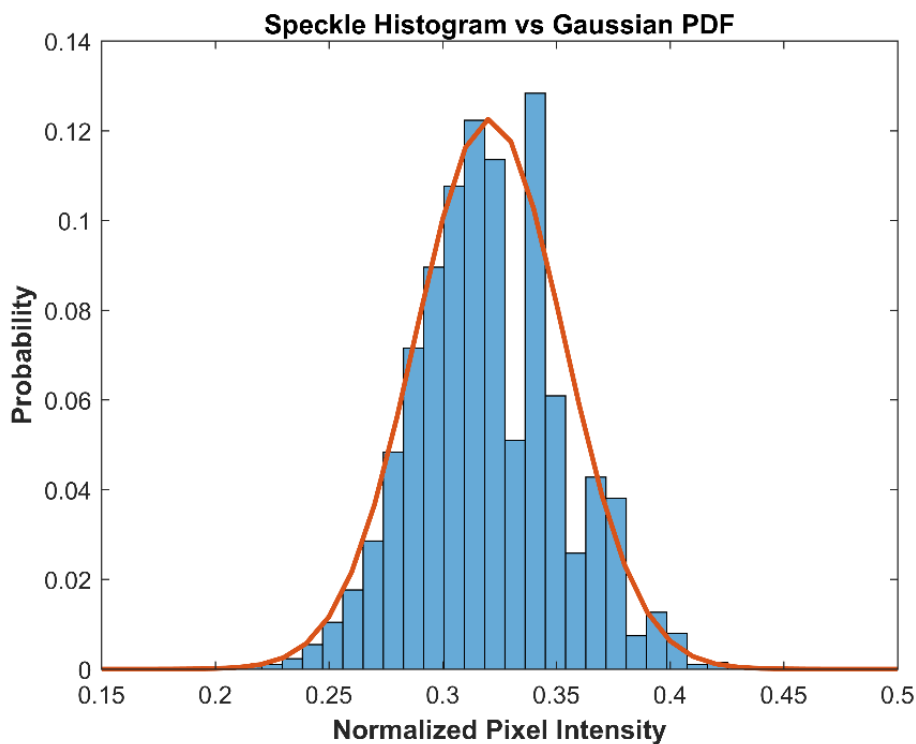
Figure 27: Histogram of speckle from tissue-mimicking breast phantom compared to Gaussian PDF (μ=0.32, σ=0.03).
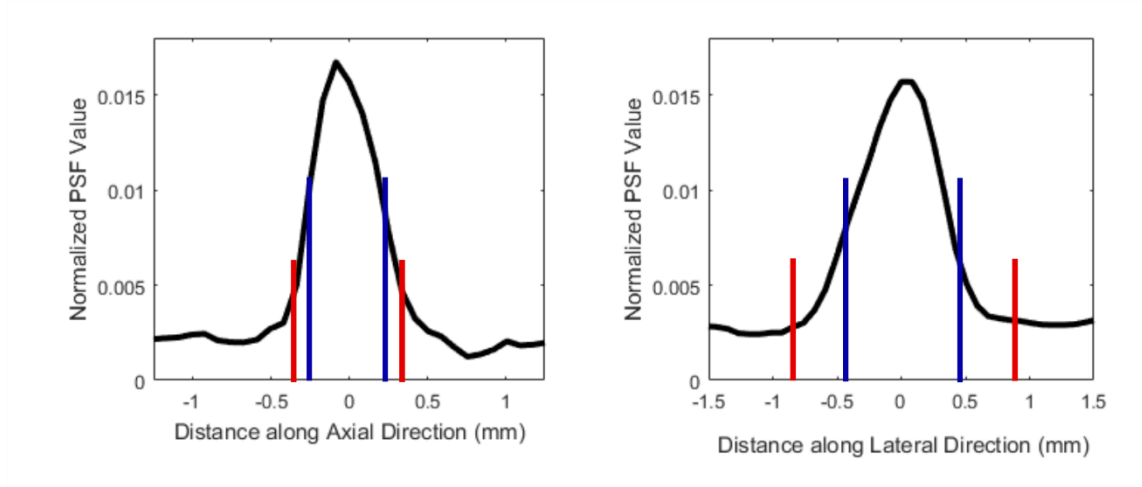
Figure 28: Cross sections from the PSF estimates. Along axial and lateral directions, image observation method using tissue-mimicking phantom data was used. Blue lines mark FWHM and red lines mark the extent of the PSF.

2.4.2. Measurement of Autocorrelation Matrix. The elements of autocorrelation matrix for a volume *I* of size *MxN* can be measured from samples by the following expression:

$$R_{p,q} = \frac{1}{M}\frac{1}{N} \sum_{i=1}^{M}\sum_{j=1}^{N}(I(i,j) - \mu)(I(i+p,j+q) - \mu) \tag{43}$$

for each shift *p, q* and put into raster scanned pixel order representation. 98 non-overlapping patches were used for more accurate estimation. Maximum correlation lengths (10% of the peak) were calculated as *3* pixel shifts along axial direction and *8* pixels along lateral direction, respectively.

If a *2* pixel shift is assumed along axial and lateral directions, a sample *5x5* correlation matrix $R_{i,j}$ is represented in spatial coordinates as follows:

$$R_{p,q} = \begin{bmatrix} R_{(-2,-2)} & R_{(-1,-2)} & R_{(0,-2)} & R_{(1,-2)} & R_{(2,-2)} \\ R_{(-2,-1)} & R_{(-1,-1)} & R_{(0,-1)} & R_{(1,-1)} & R_{(2,-1)} \\ R_{(-2,0)} & R_{(-1,0)} & R_{(0,0)} & R_{(1,0)} & R_{(2,0)} \\ R_{(-2,1)} & R_{(-1,1)} & R_{(0,1)} & R_{(1,1)} & R_{(2,1)} \\ R_{(-2,2)} & R_{(-1,2)} & R_{(0,2)} & R_{(1,2)} & R_{(2,2)} \end{bmatrix} \tag{44}$$

The images are represented as vectors in Equation (40). The corresponding autocorrelation matrix *C* in Equation (40) is to be represented in raster scanned order. The *C* matrix is formed in a symmetric, banded structure using the shift indices:

$$C = \begin{bmatrix} R_{(0,0)} & R_{(1,0)} & R_{(2,0)} & R_{(1,-2)} & R_{(-1,-1)} & R_{(1,0)} & ... & 0 & 0 \\ R_{(0,-1)} & R_{(0,0)} & R_{(1,0)} & R_{(2,0)} & R_{(1,-2)} & R_{(-1,-1)} & R_{(1,0)} & ... & 0 \\ R_{(0,-2)} & R_{(0,-1)} & R_{(0,0)} & R_{(1,0)} & R_{(1,0)} & 0 & 0 & ... & 0 \\ ... & ... & ... & R_{(0,0)} & ... & ... & ... & ... & ... \\ 0 & ... & R_{(-2,-2)} & R_{(-2,-1)} & ... & ... & ... & R_{(0,0)} & R_{(0,1)} \\ 0 & 0 & ... & R_{(-2,-2)} & R_{(-2,-1)} & ... & ... & ... & R_{(0,0)} \end{bmatrix} \qquad (45)$$

2.4.3. Regularization. Markov Random Field (MRF) assumption (Rue & Held, 2005) was made for the acquired B-mode images and Gibbs prior was used. As mentioned in Section 2.3, second norm was preferred for clique potential, since it suppresses the noisy effect of outliers. The prior term penalizes squared intensity difference between the center pixel (i) and its 8 neighbors in 2D, where d is the distance between the neighboring (i^{th} and j^{th}) pixels.
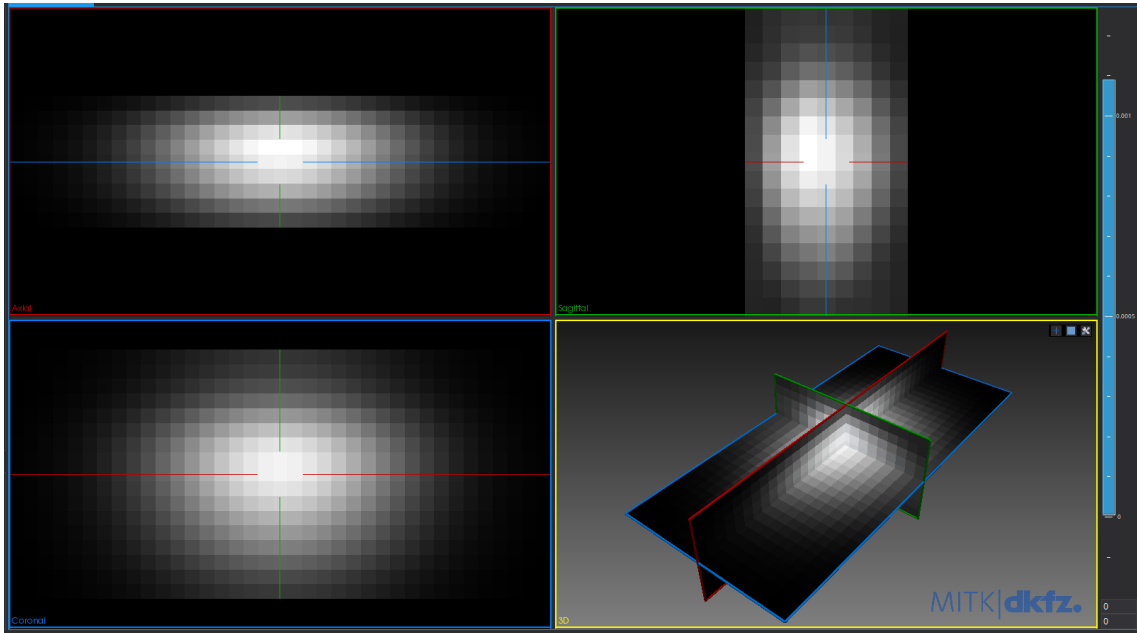
Figure 29: Visualization of 3D PSF using MITK. Along elevation, a Gaussian PSF shape was assumed.

2.4.4. Estimation of Transformation. Multi-image super-resolution requires estimation of displacement matrix T. Various rigid, affine and non-rigid methods were mentioned in above paragraphs (Section 1.8). Among those, rigid registration in frequency domain by (Vandewalle et. al., 2006), block matching and landmark based SIFT (Lowe, 2004) was

examined at preliminary trials. As stated in Section 1.8, the tissue motion may be very complex due to varying tissue stiffness, patient motion and pulsation of arteries. Rigid registration did not yield adequate accuracy. Standard block matching algorithm (as explained in Section 1.8) using mean square error and various sizes of search windows and mean square error as similarity metric was implemented. The resulting displacement field was quite inconsistent with the transducer movement, again due to complex tissue motion. A sample displacement field is visualized in Figure 30 for block size equal to 30 pixels and search window size equal to 15 pixels for an image size of 234 x 250 pixels. Displacement estimation on shallower parts are consistent with the transducer motion. However, estimated movement of each block for the deeper tissue appears to be tangled.

Considering these results, more sophisticated schemes (mentioned in Section 1.8) listed in literature, such as the work of Cifor et.al. (2013), Banerjee et.al. (2015), Morin et.al. (2015) should be implemented to acquire improved results. This requires condensed research on the image registration subject. This kind of direction was considered out of the scope of the thesis. Implementing SIFT features was also evaluated as being very computationally costly.

(a)   (b)   (c)
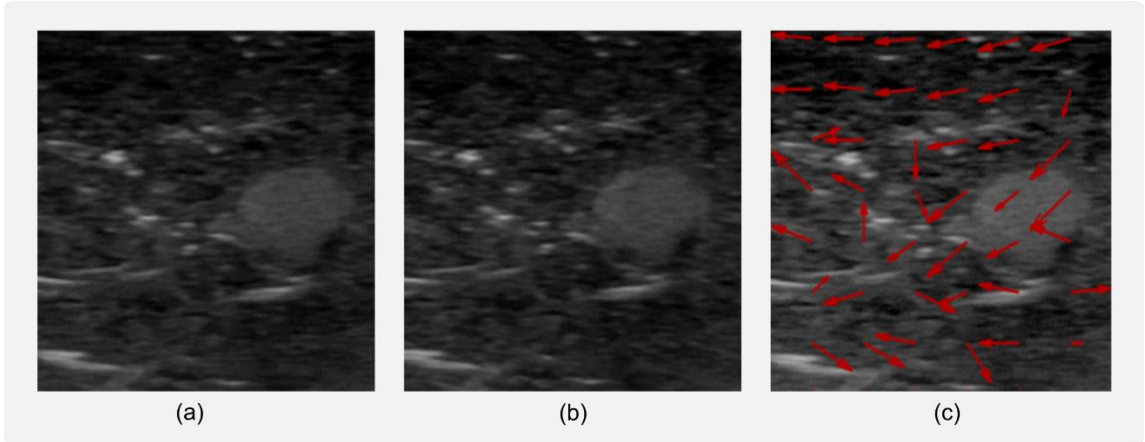
Figure 30: Estimation of transducer movement using block matching (block size: 30 pixels, search window size: 15 pixels, image size: 234x250) (a) Source image; (b) Target Image; (c) Estimated displacement vector for each block visualized using red arrows.

After evaluating the alternatives briefly, diffeomorphic demons algorithm proposed by Vercauteren et. al. (2009), based on (Thirion, 1998) was used in this study. This method is very fast (1.21 seconds for a 360x360 image) as a build-in MATLAB® (2017a) function and found quite efficient for registration purpose. The displacement field v_k of the kth image was estimated as follows

$$v_k = \frac{(\vec{y}_k - \vec{y}_1)\nabla \vec{y}_k}{\|\nabla \vec{y}_k\|^2 + (\vec{y}_k - \vec{y}_1)^2} \tag{46}$$

where $\nabla \vec{y}_k$ represent the gradient of $\vec{y}_k$ and $\|\nabla \vec{y}_k\|^2$ is the second norm of the gradient image. The difference between fixed and moving images was minimized with an iterative procedure.

2.4.5.   *Optimization.* BR-UG, BR-CG, BSRR-UG, BSRR-CG methods were implemented using a gradient descent-based method. Gradient descent optimization can be formulated as follows:

$$\vec{x}_{new} = \vec{x} - \alpha \nabla \vec{x} . \tag{47}$$

In here, α is the step size and ∇ stands for the derivative operation. Optimal step size can be obtained with line search at each iteration. Cost function in Equation (39) is calculated for $\vec{\alpha} = \{-1,0,1\}$ and its minima is found by quadratic fitting. This yields the optimal step size, α_{opt}. Using this step size, the ideal image estimate is updated using $\vec{x}_{new} = \vec{x} - \alpha_{opt} \nabla \vec{x}$.

The derivative of the likelihood function was obtained analytically. The derivative of the Gibbs prior was obtained numerically in 2D by implementing finite differences. The derivative is expressed as follows:

$$\nabla \vec{x} = A^T (\vec{y} - A \vec{x})^T C^{-1} (\vec{y} - A \vec{x}) + \nabla g(\vec{x}). \tag{48}$$

When Gibbs distribution stated in Equation (38) using second norm is assumed, by minimizing the following cost function, the ideal image estimate $\vec{x}$ can be obtained:

$$argmin_{\vec{x}} \left((\vec{y} - A \vec{x})^T C^{-1} (\vec{y} - A \vec{x}) + \lambda \sum_{i=1}^{N} \sum_{j=1}^{8} \frac{(x_i - x_j)^2}{d_{ij}} \right) \tag{49}$$

λ controls the relative weight of the two terms and N is the total number of image pixels. The optimization procedure was stopped when cost function did not decrease anymore.

For implementing BR-CG and BSRR-CG methods, the inverse matrix operation for non-identity C in Equation (39) is required. This operation is not directly tractable since it demands very large memory ($N^2 x N^2$ matrix for NxN image). Since C matrix is banded and sparse, matrix multiplication can be applied via circular shifting. An inner optimization scheme can be implemented by assigning $\vec{a} = C^{-1}(\vec{y} - A \vec{x})$, and finding vector $\vec{a}$ by means of iteratively minimizing $\|C\vec{a} - (\vec{y} - A \vec{x})\|_2^2$ by using gradient-descent algorithm. A similar approach was followed in Tilley et. al. (2015).

As observed, there are zero values which correspond to points beyond correlation length in Equation (45). This sparsity is used to avoid unnecessary multiply by zero operation. The autocorrelation Circular shifting was implemented on GPU (CUDA, NVIDIA GTX 1050) with considerably less computational burden. Correlation between images was not considered for multi-image super-resolution restoration.

The sample cross section of autocorrelation of the residual $(\vec{y} - A\vec{x})$ and decorrelated residual $C^{-1}(\vec{y} - A\vec{x})$ is shown in Figure 31. The correlation was observed to be reduced.

NVIDIA GTX 1050 has *2 GB* memory and *640* cores. The processed images were stored as *float* type variables which allocate 4 bytes in memory for each pixel, in C++ context. The correlation operation was implemented using *32* grids, *16* blocks. The operation was implemented in *16* parts. This meant that the optimisation operations could be implemented *16* times faster by using a higher capacity GPU with full parallelisation. This would result in a calculation time of under two minutes.
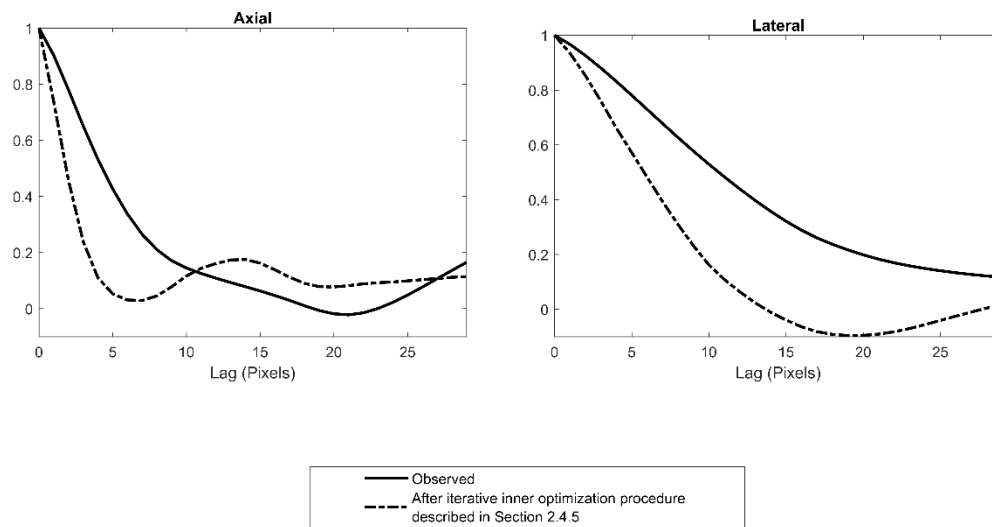
Figure 31: Autocorrelation was observed to be reduced by the inner optimization scheme mentioned in Optimization section (2.4.5).

2.5. Generation of Synthetic Phantoms

An image processing algorithm generally has a set of parameters that yields optimum output and a parameter optimization scheme is required for acquiring the most efficient results from an algorithm. In case of Bayesian restoration methods mentioned, it is the prior coefficient λ in Equation (39). In order to implement such parameter optimization procedure, a synthetic phantom with known geometric targets was used. In (Morin et. al., 2015; Baselice et. al., 2018; Wang et. al., 2009) Field II ultrasound image (Jensen & Svendsen, 1992; Jensen, 1996) was used for this purpose.

In this study, for implementation of algorithms an image with different sized targets (1-2 mm in lateral and 0.5-1.5 mm in axial) (Figure 32) was created. These targets were convolved with the measured system PSF. After that, randomly generated correlated noise was added. For super-resolution methods, the targets and the same random set of scatterers

53

were rigidly transformed within a small range: (axial: 0.057±0.0205 mm, lateral: 0.3825±0.0946, roll: 0.5375±0.1750) to obtain five ideal images. Finally, the resulting ideal images were convolved with the PSF and noise was added. Samples of synthetic speckle and the speckle from tissue-mimicking phantom are shown Figure 33, and the statistics are tabulated in Table 3 to demonstrate their similarity.
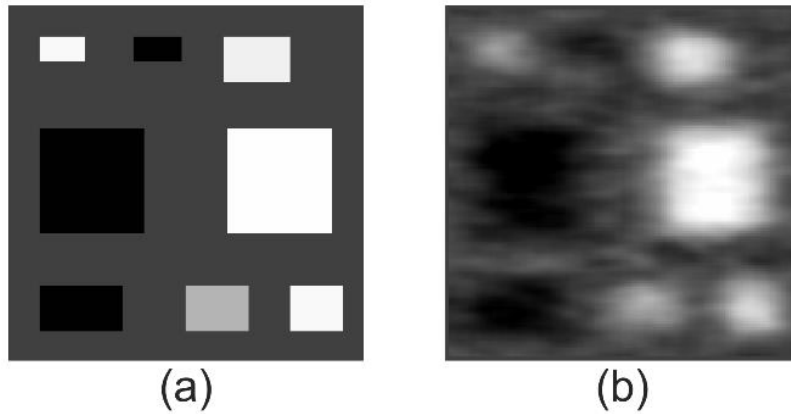
Figure 32: 2D Synthetic phantom (a) Ideal image; (b) Synthetically generated phantom image
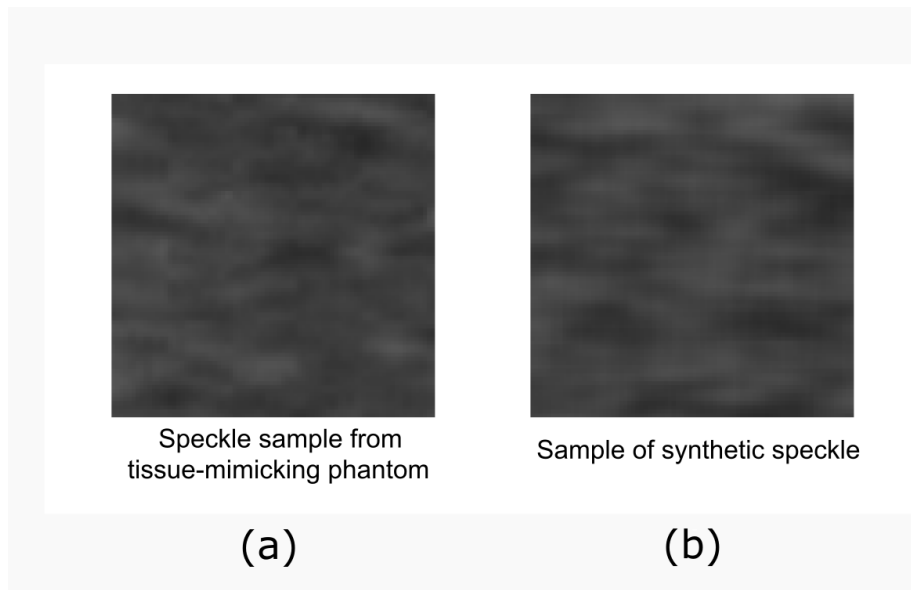
Figure 33: Visual comparison of tissue-mimicking phantom speckle (a) to synthetically created speckle; (b) Statistics are given in Table 3.

Table 4: Statistics of the real and synthetic speckle (256x256 pixels)

	Standard Dev.	Min.Value	Max.Value
Real Speckle	0.032	-0.122	0.135
Synthetic Speckle	0.033	-0.112	0.139

2.6. Comparative Study

In this work, comparative study on 2D data was conducted. For objective evaluation and VGA, the performance of BR-CG and BSRR-UG were compared to common speckle filtering methods (WF, BF, AD).

The important algorithm parameter is the diffusion coefficient κ for AD. In original paper, there were two functions offered as diffusion model. The first option was stated to favor high contrast edges over low contrast ones and the second one was to favor larger regions over smaller ones. For both options, using 8 neighbors, κ was scanned between [0.0025, 0.2000] with an interval of 0.0025.

WF was implemented using MATLAB® (2017a) built-in deconvwnr function. As an input, PSF and noise to signal ratio (NSR) is required to be fed. NSR was supplied to the script in a range of [0.00, 0.50], with an interval of 0.01.

Code from Mathworks (Lanman, 2018) was used for implementing BF. Three parameters need to be adjusted for this algorithm. First one (*w*), is the half-size of the filter window (approx. size of the PSF). The second one is the standard deviation of the spatial domain (*l*) scanned in the range 2-50, since it is related with the minimum target size (22 pixels in lateral and 11 pixels in axial). Finally, standard deviation of the intensity domain was required to be selected and this value was taken as 0.0325, according to the standard deviation of speckle (Table 1).

For all the Bayesian methods implemented (BR-UG, BR-CG, BSRR-UG and BSRR-CG), the only parameter for optimization is the coefficient of the prior term (λ), in Equation (39). Higher values of λ results in suppressing the speckle better but at the same time smoothing the image, including edges. On the other hand, low λ values result in deconvolution being more dominant (edges are sharpened, and speckle is emphasized).

2.7. Objective Evaluation

Objective evaluation using mathematical measures is essential in optimal parameter selection and evaluation of the output of image processing algorithms. For this purpose, well-accepted metrics in literature were used.

2.7.1. *Peak Signal to Noise Ratio (PSNR).* In the case of phantom images, x_i, the ideal image with geometric targets (Figure 32a) was known and the amount of error of estimated $\hat{x}_i$ from ground truth as mean square error (MSE) could be measured:

$$MSE = \frac{1}{N}\sum_i^N (\hat{x}_i - x_i)^2 \tag{50}$$

PSNR is based on mapping the mean square error to decibel scale:

$$PSNR = 10log\frac{255}{MSE} [dB] \tag{51}$$

2.7.2. *Constrast to Noise Ratio (CNR).* Contrast to noise ratio (CNR) is another common measure for evaluation (Baselice et. al., 2018; Morin et. al., 2015; Yang et. al., 2009; Wang et. al., 2009):

$$CNR = \frac{|\mu_i - \mu_o|}{\sqrt{\sigma_i^2 + \sigma_o^2}} \tag{52}$$

where μ_i and μ_o are the mean values and σ_i^2 and σ_o^2 variances of pixels inside and outside of interest respectively. In this expression, the term in the numerator ($|\mu_i - \mu_o|$), stands for contrast. The term in the denominator ($\sqrt{\sigma_i^2 + \sigma_o^2}$) is for measuring the amount of noise.

2.7.3. *Normalized Information Density (NID).* The normalized information density (NID) (Üstüner & Holley, 2003), is another objective evaluation metric that is expressed with the following terms:

$$NID = \frac{1}{2S\sigma_s^2} \tag{53}$$

where σ_s^2 is the variance of the speckle and S is the average speckle size, found by the following formula:

$$S = \int_{+\infty}^{-\infty} \Upsilon(\xi)d\xi \tag{54}$$

where Υ is the peak normalized autocovariance function (for fully developed speckle).

2.8. Implementation of VGA

In this study, VGA (described in Section 1.11) was implemented to get an initial clinical response from radiology experts. Clinically relevant questions were prepared with the help of radiology experts. Outputs of the seven methods (AD, BF, WF, BR-UG, BR-CG, BSRR-UG, BSRR-CG) were presented randomly at the same scene with the observed images. A browser-based interface (Figure 34) with radio buttons assigned to each score was prepared for this purpose. The interface program was prepared using node.js and JavaScript. The questions were recorded and read from a text file. The output was logged automatically to a text file. The text files were generated for each radiologist number selected in the beginning of the program (as shown in Figure 34a).

Opinions of five radiology experts were collected. Appropriate monitors (approved for medical standards) were used. The details of implementation of VGA are presented in section 3.3 with the selected cases. The rest of the cases are presented in Appendix I along with average scores per method.

5 radiology experts were asked to evaluate 10 images by answering 13 questions that are relevant to diagnostic purposes. The questions were also prepared by radiology experts. The participants were asked to score the algorithm output images with respect to the raw image by:

- The observability of granular coarsening for thyroid gland and breast phantom,
- The sharpness of contour for cystic and hyperechoic nodular structures in breast phantom and lymph nodule,
- The contour quality of thyroid gland,
- The observability of heterogenicity for submandibular and parotid glands,
- The observability of microcalcifications for breast phantom,
- Peripheral tissue contour and homogeneity for hand tendon,
- The sharpness of subcutaneous fat tissue for lymph nodule

The sequence of images was presented in the same random order and with no consecutive appearance of the same cases. The experts who were involved in the study had little or no prior opinion about the effect of the algorithms applied. They were not notified about which image processing algorithm was applied to each image. The questions that correspond to some selected cases are presented in section 3.3. The rest of the questions for the cases are presented in Appendix I. The questions were addressed in Turkish, however, their translation to English is also presented in the related sections.

Age of radiologists involved in evaluation is 49.8 ± 10.2, and years of experience is 19.6 ± 9.0. The monitors used for evaluation of the images were approved for medical standards

and regularly used for radiological examination. The average overall evaluation time of radiologists for 70 cases (10 images x 7 methods) was about 30 minutes.
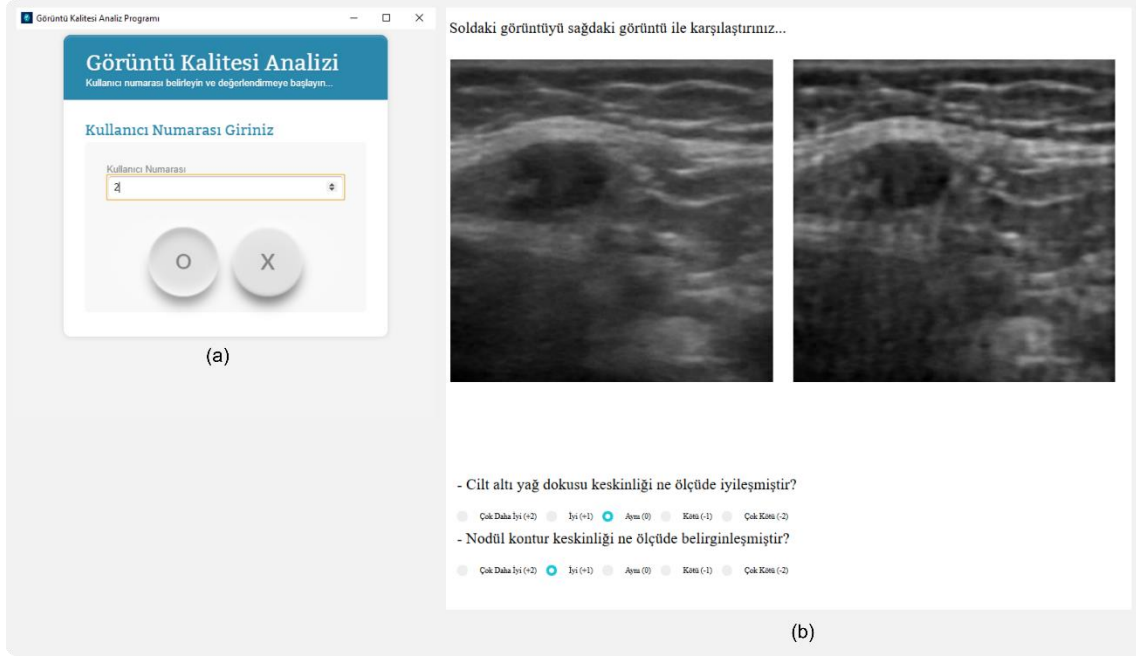
Figure 34: Browser based interface designed for image quality assessment study (a) Starting the program by setting the user number; (b) Processed image (right) is compared to the reference image (left). Clinically relevant questions were prepared, the scores were selected by using radio buttons.

CHAPTER 3

3. RESULTS

3.1.   Synthetic Phantom and Parameter Optimization

Synthetic phantom study was conducted to determine the optimal values of algorithm parameters. The parameters for the selected algorithms are explained in section 2.6 in detail.

Optimal parameter selection is essential to establish the balance between regularization effect and edge sharpening. One such example is presented for BSRR-CG algorithm in Figure 35. For the given input image, the output is observed to change dramatically for λ values. For each algorithm, each metric (PSNR, CNR and NID) was calculated for a set of parameters within a meaningful interval, as shown in Figures 36-42. These intervals are given in Table 4, in the first column. According to those values, Figure 35c ($\lambda=0.00$) correspond to ML estimate, Figure 35d ($\lambda=0.09$) correspond to optimal value, Figure 35e ($\lambda=1.00$) correspond to smoothing more than necessary.

The parameters to be optimized for the selected algorithms are listed as follows:

> **AD:** Diffusion coefficient (κ)
>   Diffusion model (*Option 1 / Option 2*)
> **BF:** Half-size of the filter window (w)
>   Standard deviation of the spatial domain (l)
> **WF:** Noise to signal ratio *(NSR)*
> **BR-UG:** Prior coefficient (λ)
> **BR-CG:** Prior coefficient (λ)
> **BSRR-UG:** Prior coefficient (λ)
> **BSRR-CG:** Prior coefficient (λ).

When the Figures 36-42 were examined, there are peaks observed at different points for PSNR, CNR and NID. Parameter optimization is challenging since there is more than one alternative and a consistent selection should be made. Peak NID values usually appeared to be between peak CNR and PSNR values. Peak CNR values tended to favor sharper edged results while peak PSNR appeared for lower smoother images. For AD and BF,

there was more than one parameter to be optimized. Therefore, all of the values described in section 2.6 were examined.

NID metric is stated to be independent of object size (Üstüner & Holley, 2003). This is very important, especially for real tissue where the target size varies considerably. Considering these advantages of NID, the parameter that resulted in highest NID was selected. According to Table 4, BSRR-CG yielded highest NID, however difference is small compared to the rest of the results of the other methods.

Table 5: Algorithm run times for all the methods are presented in Table 5, for processing a 300×300 image. As observed, the BSRR-CG run time was considerably longer, compared to other methods (19.3 min), this is due to inner optimization scheme, explained in Subsection 2.4.5. Table 5: Optimal parameters for each method on a realistic synthetic phantom were obtained for the given metrics (third, fourth and fifth columns). The best values among all algorithms for each metric are shown with bold face.

Methods	Optimal parameters (For maximum NID value)	PSNR	CNR	NID
Observed Image	-	17.04	0.40	0.33
AD	$K=0.0225$, 8 neighbor, opt.1	17.05	0.42	0.33
BF	$w=28$, $l=30$, $\sigma_{spe}=0.035$	17.07	0.42	0.33
WF	$NSR=0.04$	17.78	0.47	0.44
BR-UG	$\lambda=0.009$	18.03	0.49	0.54
BR-CG	$\lambda=0.009$	18.00	0.48	0.54
BSRR-UG	$\lambda=0.10$	**18.08**	**0.50**	0.51
BSRR-CG	$\lambda=0.09$	17.66	0.46	**0.58**

Table 6: Algorithm run times for 300x300 images.

	AD	BF	WF	BR-UG	BR-CG	BSRR-UG	BSRR-CG
Algorithm Run Time (sec)	0.30	3.34	0.09	0.90	16.7	14.3	1154.4 (19.23 min.)

(a) (b) (c) (d) (e)
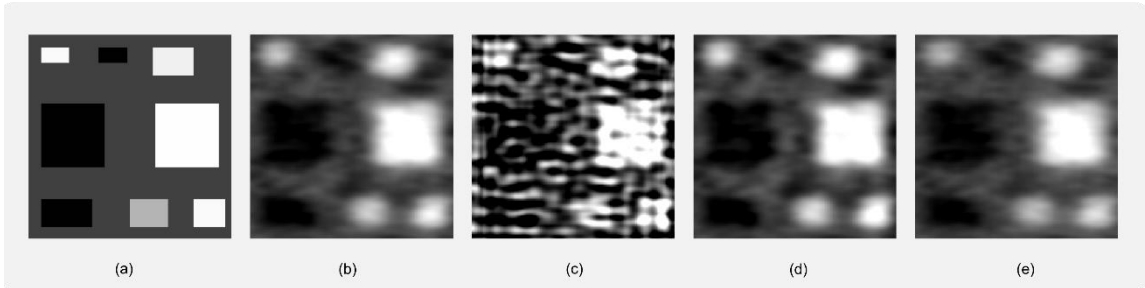
Figure 35: Parameter optimization scheme on synthetic phantom (a) Ideal image; (b) Observed image; (c) BSRR-CG result for $\lambda=0.00$ (Corresponds to ML estimator); (d) BSRR-CG result for $\lambda=0.09$; (e) BSRR-CG result for $\lambda=1.00$.

3.2. Objective Evaluation

CNR measurements on 2 mm hyperechoic and cystic targets and two high echogenicity nylon wires close to each other were conducted. The background of tissue-mimicking phantom is quite heterogenous with varying intensity. A healthy measurement for average speckle size was not available. For this reason, NID could not be used on the tissue-mimicking phantom.

The CNR measurements are listed in Table 7 and processed images are presented in Figure 44. Although AD yielded highest CNR results for 2 mm targets (11.6% for cystic target and 16.9% for hyperechoic target); the smaller targets (nylon wires) were suppressed as if they were noise.

BF had the best results for nylon wires, but it failed to improve CNR for the 2 mm hyperechoic target. In BF, contrast improvement was not obtained, this may be due to the fact that there is no deconvolution model involved in this method. BF resulted in insignificant improvement for cystic target (3.5%).

In case of BR-CG to BR-UG, there was no significant advantage observed. Both methods improved contrast ($|\mu_i - \mu_o|$) for 2 mm targets; at the same time they increased the standard deviation of speckle. Therefore overall, these methods failed to improve CNR.

Similar to BR-UG and BR-CG, WF and BSRR-UG improved contrast but emphasized the speckle, as observed in Figure 44. Again, due to increase in standard deviation of noise, CNR was not increased.

BSRR-CG method resulted in consistent (5-10%) CNR improvements for all tissue-mimicking phantom targets (Table 7). Noise suppression and contrast improvement were observed simultaneously. The rest of the methods failed to improve CNR consistently for varying targets. This may be listed as a prominent property of the proposed BSRR-CG method.

Table 7: The CNR measurements are tabulated. AD yielded highest CNR results for 2 mm targets; however smaller targets such as nylon wires were suppressed. BF had the highest results for nylon wire targets, however, did not show such performance for 2 mm hyperechoic targets. Best CNR results value shown in bold face. BF and Bayesian methods perform better for smaller targets. WF and Bayesian methods improve contrast, but, at the same time, increase standard deviation of noise (except BSRR-CG). They result in poor CNR improvement for larger targets. The improvement of BSRR-CG is consistent.

Methods	CNR (2 mm Cystic target)	CNR (2 mm Hyperechoic target)	CNR (Nylon wires with high echogenicity)
Observed Image	1.91	1.82	2.59
AD	**2.13 (11.6%)**	**2.12 (16.9%)**	2.52 (-2.7%)
BF	1.97 (3.5%)	1.62 (-10.9%)	**2.75 (6.4%)**
WF	1.70 (-10.9%)	1.59 (-12.4%)	2.22 (-14.4%)
BR-UG	1.88 (-1.3%)	1.64 (-9.8%)	2.65 (2.5%)
BR-CG	1.77 (-7.4%)	1.72 (-5.3%)	2.67 (3.3%)
BSRR-UG	1.90 (-0.3%)	1.75 (-3.6%)	2.60 (0.3%)
BSRR-CG	2.02 (6.2%)	2.00 (9.9%)	2.72 (5.3%)
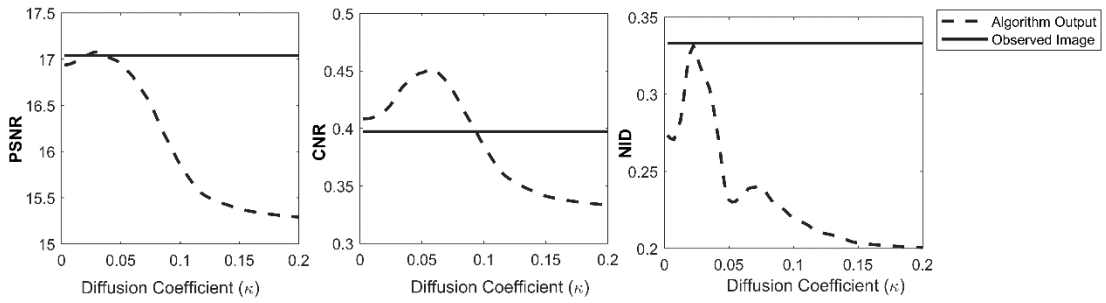
Figure 36: Parameter optimization for AD, using synthetic phantom with respect to objective evaluation metrics.
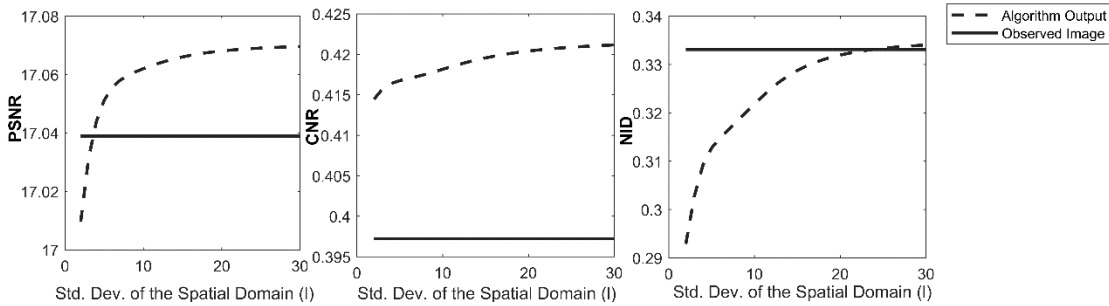
Figure 37: Parameter optimization for BF, using synthetic phantom with respect to objective evaluation metrics.
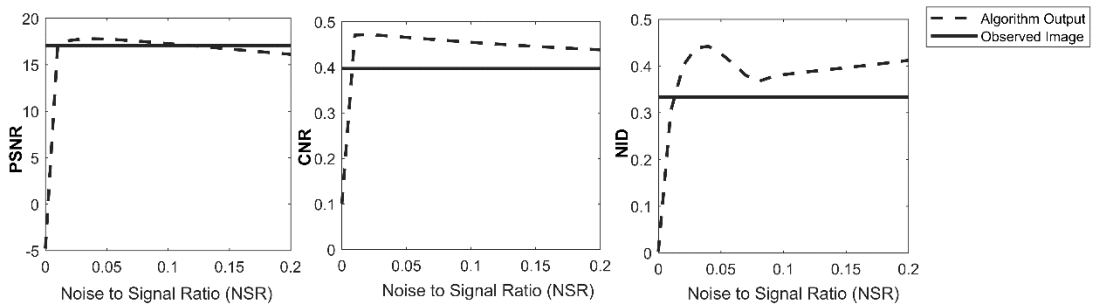
Figure 38: Parameter optimization for WF, using synthetic phantom with respect to objective evaluation metrics.
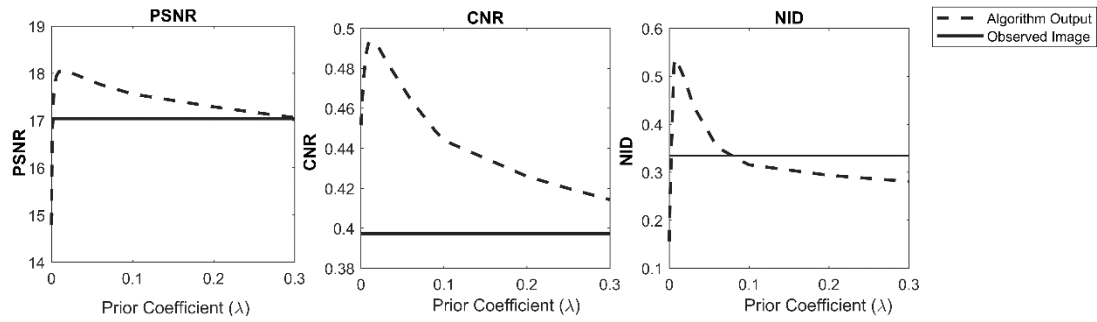
Figure 39: Parameter optimization for BR-UG, using synthetic phantom with respect to objective evaluation metrics.
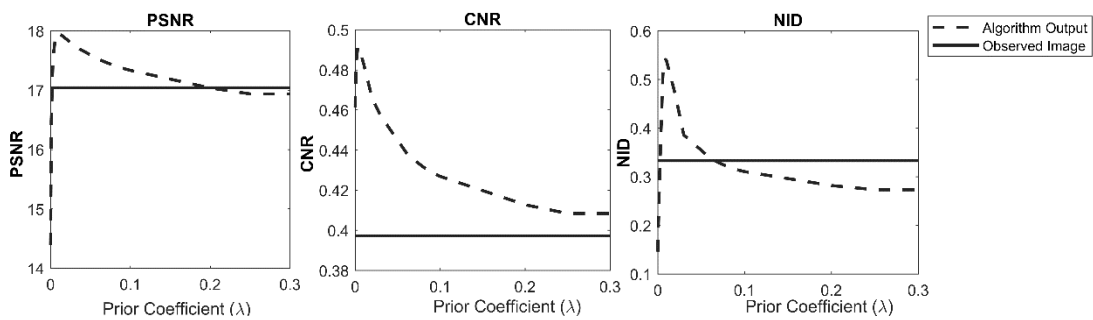
Figure 40: Parameter optimization for BR-CG, using synthetic phantom with respect to objective evaluation metrics.
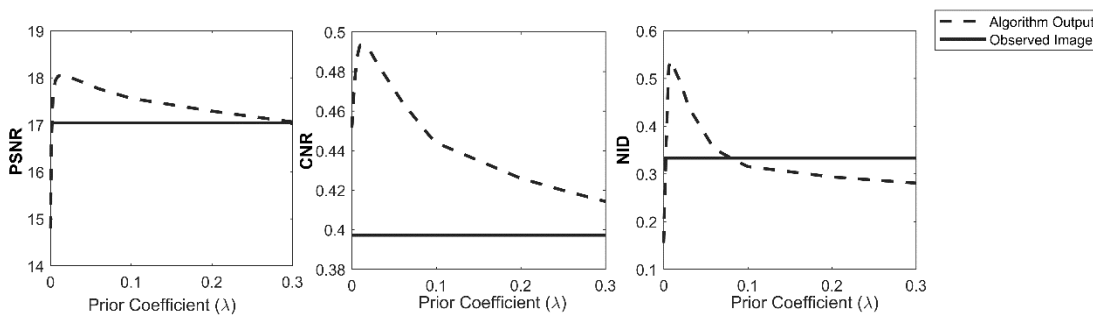
Figure 41: Parameter optimization for BSRR-UG, using synthetic phantom with respect to objective evaluation metrics.
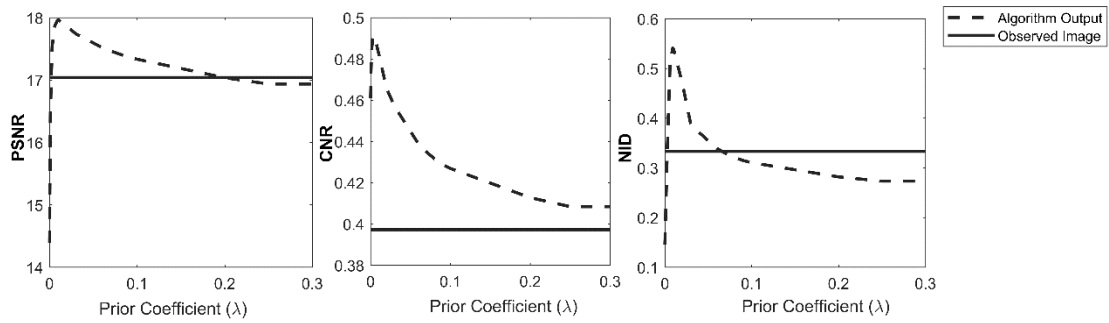
Figure 42: Parameter optimization for BSRR-CG, using synthetic phantom with respect to objective evaluation metrics.
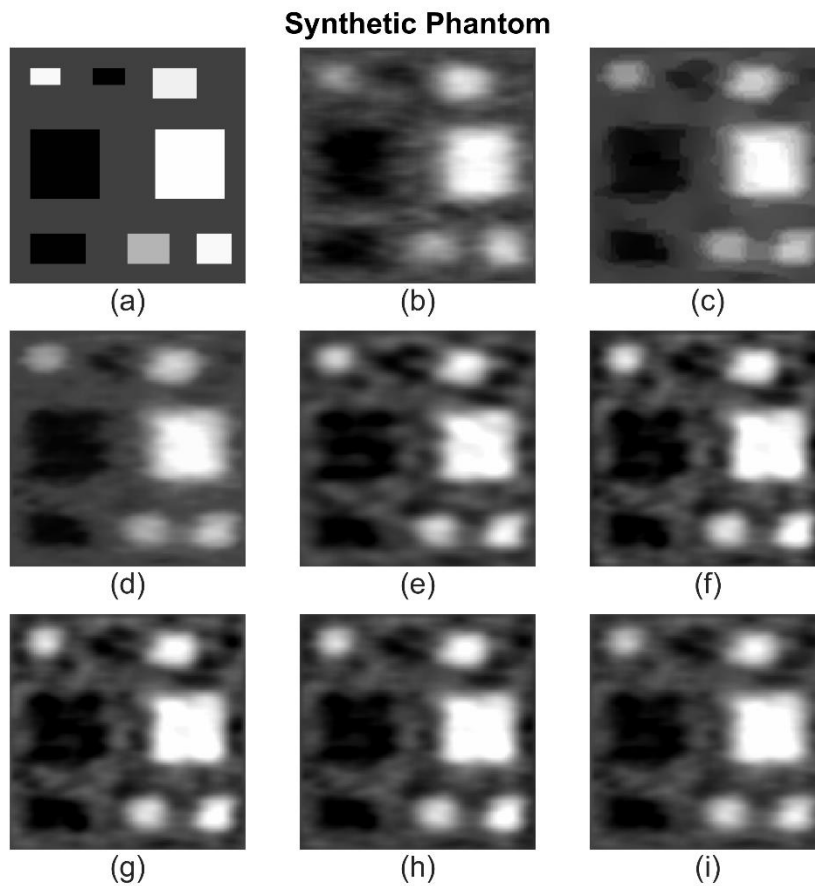
Figure 43: Synthetic phantom study results using the parameters in Table 4 (HR image size: 300x300 pixels) (a) Ideal image; (b) Synthetic phantom image (The effects of system blurring, and speckle involved); Results of restoration (c) AD; (d) BF; (e) WF; (f) BR-UG; (g) BR-CG; (h) BSRR-UG; (i) BSRR-CG.
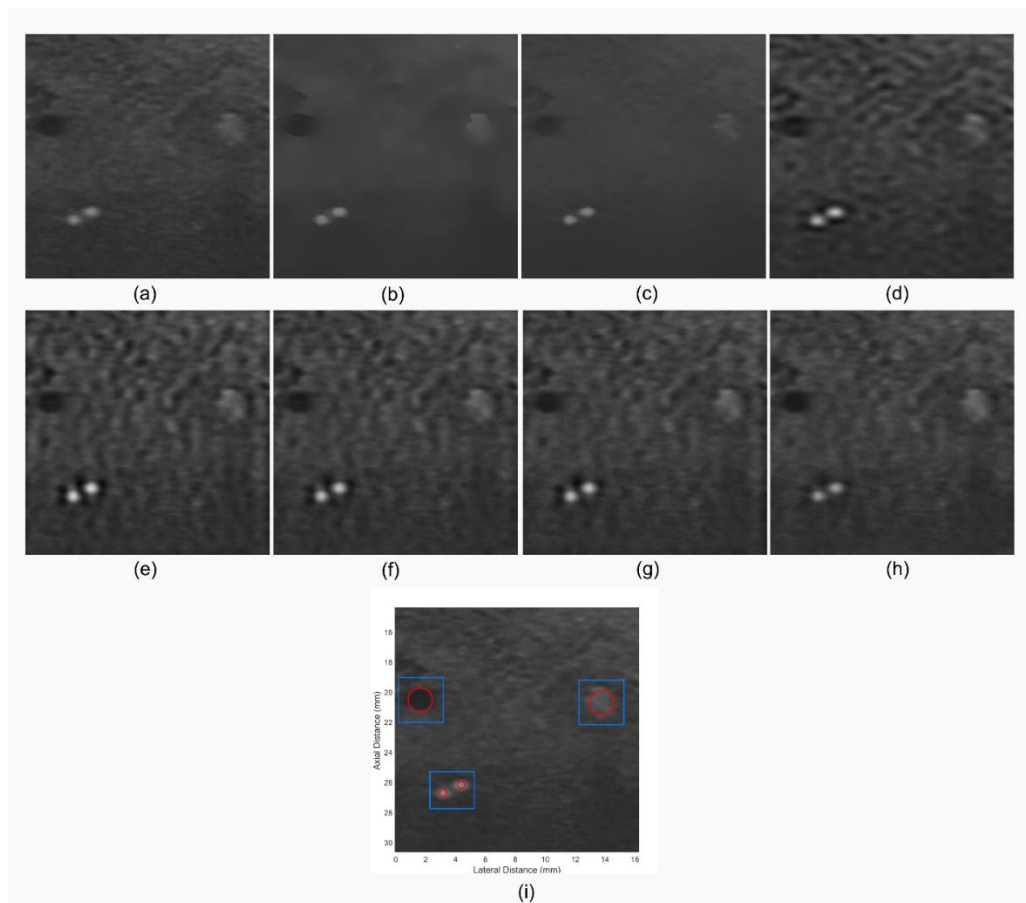
Figure 44: Algorithms applied on tissue-mimicking resolution phantom images (HR image size: 400x400 pixels). There are 2 mm cylindrical cystic target, 2 mm cylindrical, high echogenicity target and 2 nylon wires with very echogenicity higher than 15 dB. The algorithms are applied using the parameters in Table 4; (a) Observed image; Restoration results of (b) AD; (c) BF; (d) WF; (e) BR-UG; (f) BR-CG; (g) BSRR-UG; (h) BSRR-CG; (i) Areas marked for CNR measurement. Inside of inclusion are marked with red contours, outside of inclusion are marked with blue contours.

3.3. VGA and Radiologist Evaluations

Ten images in total were processed for this study and these were presented to radiologists as ten cases. Two of them are presented in Figure 46-47 and the rest of them are presented in APPENDIX A. The questions asked and the average of scores are given right after the corresponding figure.

Individual radiologist scores as well as the average score are presented in Table 7. As observed in this table, BSRR-CG had highest scores from two radiologists (0.69 and 1.00). BSRR-CG and BSRR-UG took equal scores from one radiologist (0.46). BSRR-UG had highest score from one radiologist (1.00) and BSRR-CG followed it with the closest score (0.85). AD had highest score from one radiologist (2.00).

The bin counts of each score given to each method for all 13 questions are given in Figure 45. The preferences of individual radiologists vary. In general, counts of negative scores of the BSRR-UG and BSRR-CG methods were low. BF and WF generally received mixed scores. The perception of all the Bayesian methods was either neutral or positive in general.

As observed (Table 7), the scores of AD was negative in general, except for one radiologist. The radiologist who favored AD most was observed to generally give good scores on images that had higher levels of speckle suppression. The other four radiologists commented that they preferred images that look similar to original and with sharpening of smaller details as much as possible, rather than images with high speckle suppression.

Emphasis on granular coarsening is stated to have clinical importance by radiology experts. Granular coarsening is observed in breast phantom and thyroid images for the given images. BSRR-UG and WF was observed to perform best results for these cases.

For questions related to sharpening of edges (sharpening of nodule contours, clarity of cyst, sharpness of subcutaneous tissue), BF and BSRR-CG was observed to yield highest scores. Heterogeneity is an important feature for gland images. BSRR-UG, BSRR-CG was observed to perform better than other methods in those cases.

Table 8: VGA results are tabulated for each method and each radiologist over 13 questions (in the range [-2, 2]). Highest values are shown in bold face. The last column stands for the average scores.

Methods	Rad. 1	Rad. 2	Rad. 3	Rad. 4	Rad. 5	Avg. Score
AD	-2.00	**2.00**	-1.69	-1.15	-1.00	-0.77
BF	-0.85	1.84	-0.76	-0.23	0.23	0.05
WF	-0.15	1.69	0.53	0.08	0.00	0.43
BR-UG	0.08	1.46	0.23	0.38	0.39	0.51
BR-CG	-0.30	1.23	0.38	0.08	0.39	0.36
BSRR-UG	**0.46**	1.23	**1.00**	0.31	0.69	0.74
BSRR-CG	**0.46**	1.15	0.85	**0.69**	**1.00**	**0.83**
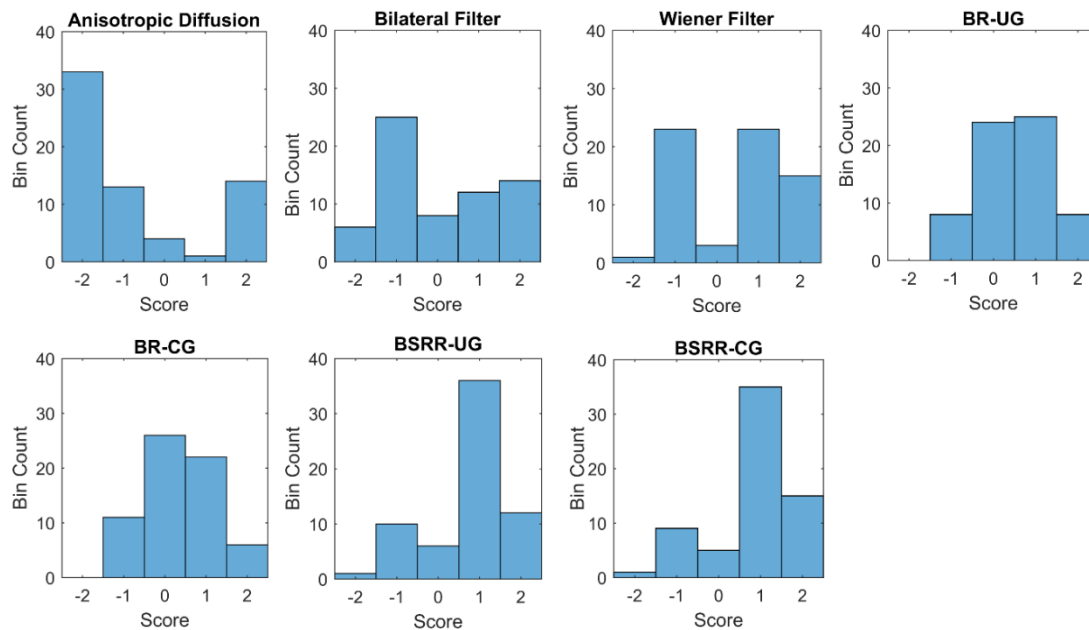
Figure 45: Bin counts for scores were obtained from radiology experts' answers (presented above) for the evaluated methods, using VGA. The highest number of positive scores was for BSRR-CG. The opinion was mixed about AD and BF.

Case 2 - Human Thyroid
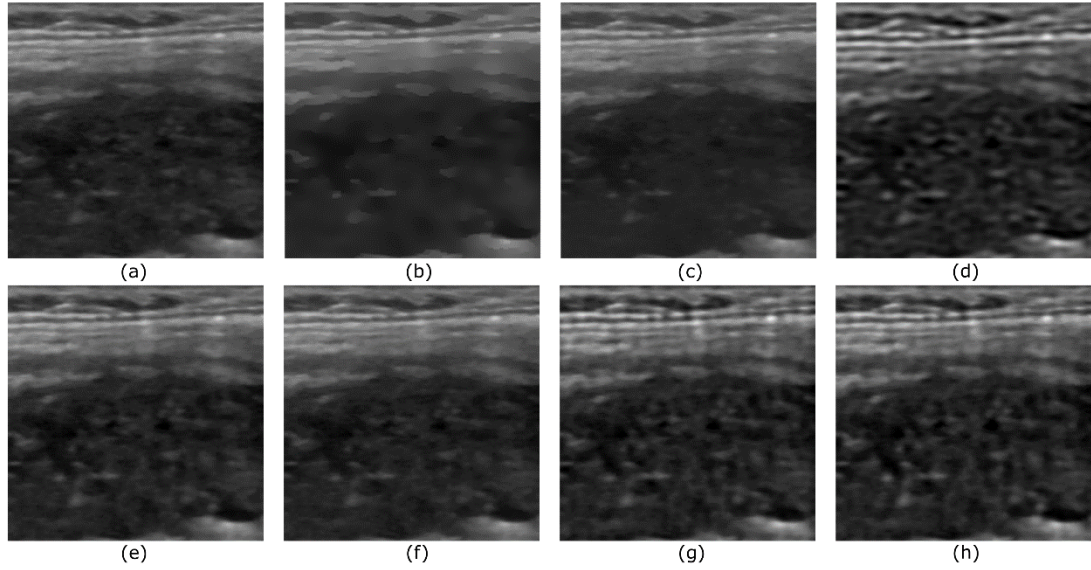
Figure 46: Restoration results of human thyroid image (HR image size: 440x440 pixels), using the parameters in Table-4 (a) Observed image; Restoration results of (b) AD; (c) BF; (d) WF; (e) BR-UG; (f) BR-CG; (g) BSRR-UG; (h) BSRR-CG.

Case 2 - Question 1:

Eng: How do you score the amount of increase in thyroid contour image quality?
Tr: Tiroid konturu görüntü kalitesi ne ölçüde artmıştır?

Average Scores:

AD	BF	WF	BR-UG	BR-CG	BSRR-UG	BSRR-CG
-0.8	0.4	0.8	**1.2**	0.4	0.6	**1.2**

Case 6 – Human Lymph Nodule
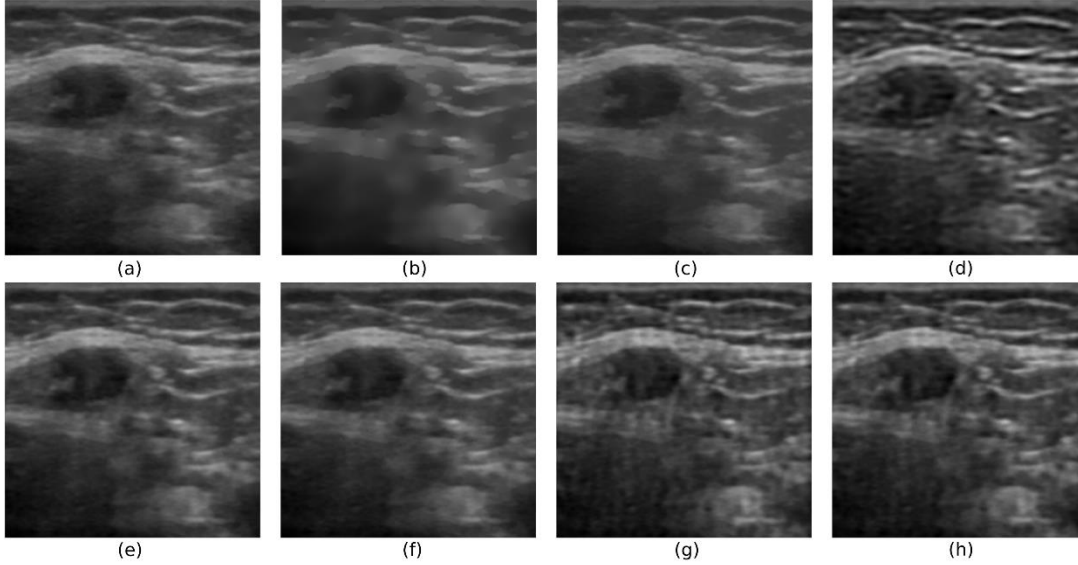
Figure 47: Case 6 - Restoration results of human lymph nodule (volunteer with systemic lupus erythematosus), using the parameters in Table-4 (HR image size: 510x510 pixels) (a) Observed image; Restoration results of (b) AD; (c) BF; (d) WF; (e) BR-UG; (f) BR-CG; (g) BSRR-UG; (h) BSRR-CG.

Case 6 - Question 1:

Eng: How do you score the amount of improvement of sharpness of subcutaneous tissue?
Tr: Cilt altı yağ dokusu keskinliği ne ölçüde iyileşmiştir?

Average Scores:

AD	BF	WF	BR-UG	BR-CG	BSRR-UG	BSRR-CG
-1.0	0.2	0.0	0.8	0.2	0.6	**1.6**

Case 6 - Question 2:

Eng: How do you score the amount of increase in sharpening of the nodule contour?
Tr: Nodül kontur keskinliği ne ölçüde belirginleşmiştir?"

Average Scores:

AD	BF	WF	BR-UG	BR-CG	BSRR-UG	BSRR-CG
-1.0	0.0	0.4	0.8	0.2	0.4	**1.6**

CHAPTER 4

4. CONCLUSION

4.1. Summary of the Work

In this thesis, ways to improve B-mode ultrasound image quality were sought. The effects of imaging system blur and spatial correlation were incorporated into the restoration model. Both the imaging system PSF and the autocorrelation matrix were measured experimentally. Bayesian approach was implemented for single-image restoration (BR-UG, BR-CG) and multi-image super-resolution restoration (BSRR-UG, BSRR-CG). This way, statistics of ultrasound B-mode data were incorporated into the model. Using an imaging system model, synthetic phantom images were generated. These images were used for parameter optimization. To find the optimal regularization coefficient, various metrics such as NID, CNR and PSNR were evaluated.

A brief speckle-tracking study was conducted placing and fixing the ultrasound probe on a precise 1D mechanical arm. Speckle decorrelation curve was formed for the imaging system. This curve was then used for checking the in-plane assumption of multiple images collected for super-resolution methods.

Data was collected from tissue-mimicking resolution phantoms, breast phantom and samples from volunteers (with informed consent). Human data was collected from various superficial tissue, thyroid and other glands around neck and hand tendon. Tissue-mimicking resolution phantom data was used to measure CNR for targets with various sizes and echogenicities.

For comparative evaluation, common methods for image quality improvement (AD, BF and WF) were selected and implemented. The same procedure for parameter optimization was implemented for these methods. CNR values were compared with the proposed methods. Samples from tissue-mimicking breast phantom and superficial tissue images from volunteers were used for VGA.

The proposed BSRR-CG method may have potential for clinical applicability. The findings of the study (results of objective evaluation and VGA) are presented in the Discussion Section, in detail, along with the possible clinical usage options. Then, in Conclusion and Future Work Section, a set of possible further studies related to this work are examined and discussed.

4.2. Discussion

Spatial correlation in ultrasound images was examined in a very limited number of studies in literature. In addition to that, it is noticed that the effect of target size and the change in objective evaluation metrics with varying target size were not comprehensively examined. In (Wang, 2009), in-plane multi-image super-resolution was conducted and CNR, MSE was measured solely on Field II images. In (Dai et. al., 2009), an intima region was segmented and CNR was measured. In Yang et.al (2007, 2009), cystic regions from tissue-mimicking breast phantom was used for CNR measurement.

In this study, CNR results acquired from a tissue-mimicking resolution phantom revealed that the proposed BSRR-CG method results in consistent improvements for varying target sizes. Most of the other methods yield successful results for a particular size (i.e. larger or smaller), and yield unsuccessful results for the rest. This inconsistency is a drawback for clinical applications since the target size varies considerably.

In the works of Parker (2012), Parker and Chen, (2016, 2017), an increase in contrast was emphasized, however, the increase of variance of noise was not examined. As the amount of deconvolution is increased, the increase in noise variance is inevitable. Therefore, some regularization term has to be introduced, and its coefficient is to be selected carefully (considering this trade-off between sharpening of the edges, contrast enhancement and increase in noise variance, due to high frequency emphasis of deconvolution operation). This is also demonstrated in Figure 35. Using a ML estimator, the edges can be recovered very effectively, yet the noise gets emphasized. Speckle shrunk in high amounts; however, it became spiky and its variance was increased. Among similar studies in literature, a detailed parameter selection scheme similar to ours was not mentioned in such detail.

Another contribution of this study was the evaluations done by the radiology experts using VGA. There are a very limited number studies that examine expert response to the restored / filtered images. Clinically relevant questions were used for evaluations and the restored images were evaluated for a variety of clinical cases.

Both objective evaluations and VGA showed that single-image Bayesian restoration methods (BR-CG and BR-UG) did not result in noticeable improvements. On the other hand, involving spatial correlation in multi-image super-resolution resulted in considerable improvements for all metrics. Both BSRR-UG and BSRR-CG resulted in contrast enhancement. As mentioned in the above paragraphs, the noise variance is usually increased when the deconvolution operation is conducted. In case of BSRR-CG, the noise variance increased less than BSRR-UG. This results in higher CNR results. The radiologists' evaluations (VGA results) showed that this trait of BSRR-CG was noticeable.

BR-CG and BSRR-CG methods were implemented using a mid-range GPU (NVIDIA GTX 1050). As stated in Section 2.4, using a higher capacity GPU, full parallelisation can

be possible, reducing the estimated calculation time to under two minutes (16 times faster).

4.3. Conclusion and Future Work

In this study, the improvement of 2D B-mode ultrasound image quality was evaluated from many aspects, in a Bayesian framework. A meticulous literature survey on ultrasound deconvolution, multi-image super-resolution and spatial correlation was conducted. It should be considered that the methods proposed were applied as post-processing operations. A further improvement would be to apply the methods in real-time, as a part of image acquisition process.

Another improvement would be achieved by using IQ data instead of B-Mode data (which is acquired after envelope detection, log-compression and scan conversion operations). IQ data would fit the proposed linear model better and the underlying physics in image formation process.

The method proposed here can be extended to other image settings and to deeper tissue by using a depth-dependent PSF. One such method is to apply depth dependent deconvolution, such as the one proposed by Adam and Michailovich, (2001). The methods proposed can also be extended to other imaging systems and probes. This can be done by updating the PSF and correlation matrix. The methods described in Section 2.4 can be implemented for this purpose or other methods for measuring PSF and autocorrelation may be used. The results of an earlier study (Şener et.al., 2016) showed that an approximately selected PSF and correlation matrix can result in considerable improvements in image restoration.

All the methods mentioned can also be extended to 3D by replacing images with volumes. Only requirement to extend the models to 3D is to consider the increased computing demand. 3D data has many advantages over 2D cross-sections. However, it is quite costly and low resolution, when acquired using 2D transducer arrays. Acquiring volume data from freehand 2D cross sections and 1D probes using a tracking sensor or by implementing speckle tracking scheme would be a strong alternative to 2D arrays, since 2D arrays available in current technology are low resolution. However, it is quite challenging to properly reconstruct the exact volume because of the drift due to measurement errors. Moreover, 3D registration of two reconstructed volumes is another interesting yet difficult problem to be solved.

The proposed BSRR-CG method yielded a consistent improvement for various targets and tissue, while other methods that were involved in the comparative study lacked such consistency. This consistency is considered to be a useful property for real-life cases. Further investigation is essential to determine the extent of the contribution of this method for clinical applications more accurately. The number of experts involved in the study should be larger.

Acquisition of multiple images from the same imaging plane is a challenging problem due to tissue motion. Irregular force on probe, tissue movement due to pulsation of large arteries and cardiac related input, motion due to breathing, and its effects on image should all be examined in detail. In this work, very small movement of probe was forced while collecting freehand data. Non-rigid image registration between each frame was implemented to compensate for motion. More effective methods such as respiratory or ECG gating can be coupled with the current scheme for a better compensation performance.

REFERENCES

Achim, A., A. Bezerianos, and P. Tsakalides. 2001. "Novel Bayesian multiscale method for speckle removal in medical ultrasound images." *IEEE Transactions on Medical Imaging* 20: 772-783.

Adam, D, and O Michailovich. 2001. Wavelet depulsing of ultrasound echo sequences . US Patent US7025724B2. 05 27.

Afsham, N., A. Rasoulian, M. Najafi, P. Abolmaesumi, and R. Rohling. 2015. "Nonlocal means filter-based speckle tracking." *IEEE Transcations on Ultrasounics, Ferroelectrics and Frequency Control* 1501-15.

Afsham, N., M. Najafi, P. Abolmaesumi, and R., Rohling. 2014. "A Generalized correlation-based model for out-of-plane motion estimation in freehand ultrasound." *IEEE Transactions on Medical Imaging* 33: 186-99.

Alessandrini, M., S. Maggio, J. Porée, L. De Marchi, N. Speciale, E. Franceschini, O. Bernard, and Basset O. 2011. "A Restoration framework for ultrasonic tissue characterization." *IEEE Transactions on Ultrasonics, Ferroelectrics, Frequency Control* 58-11: 2344-2360.

Baba (Hitachi Aloka Medical), H. 2013. Ultrasound diagnostic device and ultrasound image super-resolution image generation method. WO Patent WO 2013150917 A1. 10 10.

Banerjee, J., C. Klink, E.D. Peters, W.J. Niessen, A. Moelker, and T. Van Walsum. 2015. "Fast and robust 3D ultrasound registration – Block and game theoretic matching." *Medical Image Analysis* 20: 173–183.

Barlett, M.S. 1955. *An Introduction to Stochastic Processes.* New York: Cambridge University Press.

Barron, J. L., D. J. Fleet, and S. S., Beauchemin. 1994. "Performance of Optical Flow Techniques." *International Journal of Computer Vision* 12 (1): 43-77.

Baselice, F., G. Ferraioli, A.C. Johnsy, Pascazio V., and G. A Schirinzi. 2015. "Bayesian method for speckle reduction in single look SAR images." *IEEE International Symposium On Geoscience And Remote Sensing.* 26-31. doi:10.1109/IGARSS.2015.7326307.

Baselice, F., G. Ferraioli, A.C. Johnsy, Pascazio V., and G. Schirinzi. 2015. "Speckle reduction based on Wiener filter in ultrasound images." *Annual International Conference of the IEEE Engineering in Medicine and Biology Society.* 3065-3068.

Baselice, F., G. Ferraioli, M. Ambrosanio, V. Pascazio, and G. Schirinzi. 2018. "Enhanced wiener filter for ultrasound image restoration." *Computational Methods Programs Biomedicine* 153: 71-81.

Bharti, P., D. Mittal, and R. Ananthasivan. 2017. "Computer-aided Characterization and Diagnosis of Diffuse Liver Diseases Based on Ultrasound Imaging: A Review." *Ultrasonic Imaging* 39: 33 –61.

Blackall, J.M., G.P. Penney, A.P. King, and D.J. . Hawkes. 2005. "Alignment of sparse freehand 3-d ultrasound with preoperative images of the liver using models of respiratory motion and deformation." *IEEE Transactions on Medical Imaging* 24: 1405-1416.

Blume, M., D. Zikic, W. Wein, and N., Navab. 2007. "A new and general method for blind shift-variant deconvolution of biomedical images." *International Conference on Medical Image Computing and Computer-Assisted Intervention.* 743–750.

Born, M., and E. Wolf. 1999. *Principles of Optics.* 7. New York: Cambridge University Press.

Burckhardt, C.B. 1978. "Speckle in ultrasound B-mode scans." *IEEE Transactions on Sonics and Ultrasonics* 25: 1-6.

Campisi, P., and K. Egiazarian. 2007. *Blind Image Deconvolution, Theory and Applications.* Florida: CRC Press.

Chen, J.F., J.B. Fowlkes, P.L. Carson, and J.M. Rubin. 1997. "Determination of scan-plane motion using speckle decorrelation: theoretical considerations and initial test." *International Journal of Imaging Systems Technology* (38-44) 8.

Chen, S., and K. J., Parker. 2017. "Enhanced axial and lateral resolution using stabilized pulses." *Journal of Medical Imaging* 4:(2).

Chen, S., and Parker K. J. 2016. "Enhanced resolution pulse-echo imaging with stabilized pulses." *Journal of Medical Imaging* 3(2).

Cifor, A., L. Risser, D. Chung, E.M. Anderson, and J.A. Schnabel. 2013. "Hybrid feature-based diffeomorphic registration for tumor tracking in 2-D liver ultrasound images." *IEEE Transactions on Medical Imaging,* 32: 1647-1656.

CIRS., Inc. 2019. "CIRS Tissue Simulation & Phantom Technology." 01 11. http://www.cirsinc.com/products/all/67/multi-purpose-multi-tissue-ultrasound-phantom/.

Clement, G.T., and K. Hynynen. 2004. "Superresolution Ultrasound for Imaging and Microscopy." *IEEE Ultrasonics Symposium.* 1832-1835.

Clement, G.T., J. Huttunen, and K. Hynynen. 2005. "Superresolution ultrasound imaging using back-projected reconstruction." *Journal of Acoustical Society of America* 118: 3953-3960.

Cüneyitoğlu Özkul, Mine, and Ünal Erkan Mumcuoğlu. 2018. "Ultrasonik Tıbbi Görüntülemenin Temelleri ve Görüntü." In *Biyomedikal Mühendisliği ve Uygulamaları*, edited by Onur Koçak and Osman Eroğul. Ankara: Elektrik Mühendisleri Odası.

Dai, Y., B. Wang, and D.C. Liu. 2009. "A fast and robust super resolution method for intima reconstruction in medical ultrasound." *The 3rd IEEE International conference on bioinformatics and biomedical engineering.* 1-4.

Duda, R.O., P.E. Hart, and D.G. Stork. 2001. *Pattern Classification.* New York: Wiley.

Dutt, V. 1995. "Statistical Analysis of Ultrasound Envelope." *PhD Thesis, Mayo Graduate School, Biomedical Imaging.*

Elad, M., and A. Feuer. 1997. "Restoration of a single superresolution image from several blurred, noisy, and undersampled measured images." *IEEE Transactions on Image Processing* 6: 1646-1658.

Ellis, M.A., F. Viola, and W.F. Walker. 2010. "Super-resolution image reconstruction using diffuse source models." *Ultrasound in Medicine & Biology* 36: 967-977.

Eltoft, T. 2006. "Modeling the amplitude statistics of ultrasonic images." *IEEE Transactions on Medical Imaging* 25 (2): 229–240.

Eltoft, T.,. 2005. "The Rician inverse Gaussian distribution: a new model for non-Rayleigh signal amplitude statistics." *IEEE Transactions on Image Processing* 14: 1722-1735.

Fischler, M.A., and R.C. Bolles. 1989. "Random sample consensus: a paradigm for model fitting with applications to image analysis and automated cartography." *Communications of the ACM* 24: 381-395.

Fitzpatrick, J.M., D.L.G. Hill, and Maurer Jr. C.R. 2008. "Chapter 8." In *Image Registration, Handbook of medical imaging*, by J.M., Sonka, M. Fitzpatrick. Washington: SPIE Press.

Garra, B.S. 2005.

Gee, A.H., G.M. Treece, R.W. Prager, C.J.C. Cash, and L. Berman. 2003. "Rapid registration for wide field of view freehand three-dimensional ultrasound." *IEEE Transactions on Medical Imaging* 22: 1344-1357.

Gee, A.H., R. James Housden, P. Hassenpflug, G.M. Treece, and R.W. Prager. 2006. "Sensorless freehand 3D ultrasound in real tissue: speckle decorrelation without fully developed speckle." *Medical Image Analysis* 10: 137-149.

Gerchberg, R. 1974. "Super-resolution through error energy reduction." *Optical Acta: Journal of Modern Optics* 21: 709–720.

Gonzalez, R.C., and R.E. Woods. 2001. *Digital image processing.* 2. New Jersey: Prentice Hall.

Goodman, J.W. 1996. "Introduction to Fourier Optics." United States of America: McGraw-Hill.

Goodman, J.W. 2007. "Speckle Phenomena in Optics: Theory and Applications." Colorado: Roberts and Company Publishers.

Harris, E.J., N.R. Miller, J.C. Bamber, J.R. Symonds-Tayler, and P.M. Evans. 2010. "Speckle tracking in a phantom and feature-based tracking in liver in the presence of respiratory motion using 4D ultrasound." *Physics in Medicine & Biology* 55: 3363-3380.

Hartov, A., K. Paulsen, S. Ji, K. Fontaine, M.L. Furon, A. Borsic, and D. Roberts. 2010. "Adaptive spatial calibration of a 3d ultrasound system." *Medical Physics* 37: 2121-2130.

Hossack, J.A., T.S. Sumanaweera, S. Napel, and J.S. Ha. 2002. "Quantitative 3-d diagnostic ultrasound imaging using a modified transducer array and an automated image tracking technique." *IEEE Transactions on Ultrasonics, Ferroelectrics, and Frequency Control.*

Huang, L., Y. Labyed, K. Hanson, D. Sandoval, J. Pohl, and M. Williamson. 2013. "Detecting breast microcalcifications using superresolution ultrasound imaging: a clinical study." *Proceedings SPIE 8675, Medical Imaging 2013: Ultrasonic Imaging, Tomography, an.*

Huang, Q.H., and Y.P. Zheng. 2008. "Volume reconstruction of freehand three dimensional ultrasound using median filters." *Ultrasonics* 48: 182-192.

Huang, Q.H., Y.P. Zheng, M.H. Lu, and Z.R., Chi. 2005. "Development of a portable 3d ultrasound imaging system for musculoskeletal tissues." *Ultrasonics* 43: 153-163.

Huang, Q.H., Z. Yang, W. Hu, L.W. Jin, G. Wei, and X. Li. 2013. "Linear tracking for 3-D medical ultrasound imaging." *IEEE Transanctions on Cybernetics,* 43: 1747-1754.

Ijaz, U.Z., R.W. Prager, A.H. Gee, and G.M. Treece. 2010. "Optimization strategies for ultrasound volume registration." *Measurement Scienece & Technology* 21: 8.

Irani, M., and S. Peleg. 1991. "Improving resolution by image registration." *CVGIP: Graphical Models and Image Processing archive* 53: 231-239.

Irani, M., and S. Peleg. 1991. "Improving resolution by image registration." *CVGIP: Graphical Models and Image Processing* 53: 231-239.

Jakeman, E., and P.N. Pusey. 1978. "Significance of K Distributions in Scattering Experiments." *Physical Review Letters* 40: 546-550.

Jensen, J.A. 1996. "Field: A Program for Simulating Ultrasound Systems." *10th Nordic-Baltic Conference on Biomedical Imaging Published in Medical & Biological Engineering & Computing, Supplement 1, Part 1.* 351-353.

Jensen, J.A. 2002. "Ultrasound Imaging and its modeling." Edited by M., Kuperman, W.A., Montagner, J.-P., Tourin, A. Fink. Springer Verlag.

Jensen, J.A., and N.B. Svendsen. 1992. "Calculation of pressure fields from arbitrarily shaped, apodized, and excited ultrasound transducers." *IEEE Transactions on Ultrasonics, Ferroelectrics, Frequency Control* 39: 262-267.

Jensen, J.A., J. Mathorne, T. Gravesen, and B. Stage. 1993. "Deconvolution of in-vivo ultrasound B-mode images." *Ultrasonic Imaging* 15(2): 122-133.

Klein, S., M. Staring, K. Murphy, M.A. Viergever, and J.P. Pluim. 2010. "elastix: a toolbox for intensity-based medical image registration." *IEEE Transactions on Medical Imaging* 29: 196-205.

Klein, T.J. 2012. "Statistical Image Processing of Medical Ultrasound Radio Frequency Data." *PhD Thesis Munich Technical University, Faculty of Informatics.*

Kotaki, G., A. Miyamoto, and K. Nakahira. 2011. " ", , US Patent: 20130090560 A1. Ultrasound image reconstruction method, device therefor, and ultrasound diagnostic device.

Krucker, J.F., G.L. LeCarpentier, J.B. Fowlkes, and P.L.. Carson. 2002. "Rapid elastic image registration for 3-D ultrasound." *IEEE Transactions on Medical Imaging* 21: 1384-1394.

Kuan, D., A. Sawchuck, T. Strand, and P. Chavel. 1985. "Adaptive noise smoothing filter for images with signal-dependent noise." *IEEE Transactions on Pattern Analysis and Machine Intelligence* 165-177.

Labyed, Y., and L. Huang. 2013. "Super-resolution ultrasound imaging using a phase-coherent MUSIC method with compensation for the phase response of transducer elements." *IEEE Transactions on Ultrasonics, Ferroelectrics, and Frequency Control* 60: 1048-1060.

Lanman, D. 2018. *Bilateral filtering, MathWorks File Exchange. Version 1.0.0.0.* . Accessed 11 12, 2018. https://www.mathworks.com/matlabcentral/fileexchange/12191-bilateral-filtering?s_tid=prof_contriblnk .

Laporte, C., and T. Arbel. 2011. "Learning to estimate out-of-plane motion in ultrasound imagery of real tissue." *Medical Image Analysis* 15: 202-213.

Lee, J.S. 1980. "Digital image enhancement and noise filtering by use of local statistics." *IEEE Transactions on Pattern Analysis and Machine Intelligence* 165-168.

Li, M. (Siemens Medical Systems). 1995. System and method for 3-D medical imaging using 2-D scan data. US Patent 5582173 A. 11 28.

Liu, Y., H.D. Cheng, J. Huang, Y. Zhang, X. Tang, and J. Tian. 2013. "An effective non-rigid registration approach for ultrasound image based on "demons" algorithm." *Journal of Digital Imaging* 26 (3): 521-529.

Loupas, T., W. Mcdicken, and P. Allen. 1989. "An adaptive weighted median filter for speckle suppression in medical ultrasound images." *IEEE Transactions on Circuit Systems* 36: 129-135.

Loupas, T., W. Mcdicken, and P. Allen. 1989. "An adaptive weighted median filter for speckle suppression in medical ultrasound images." *IEEE Transactions on Circuit Systems* 36: 129-135.

Lowe, D.G. 2004. "Distinctive Image Features from Scale-Invariant Keypoints." *International Journal of Computer Vision* 60: 91-110.

Lu, X., S. Zhang, W. Yang, and Y. Chen. 2010. "SIFT and shape information incorporated into fluid model for non-rigid registration of ultrasound images." *Computer Methods and Programs in Biomedicine,* 100: 123–131.

Lu, X., S. Zhang, W. Yang, and Y. Chen. 2010. "SIFT and shape information incorporated into fluid model for non-rigid registration of ultrasound images." *Computer Methods and Programs in Biomedicine* 100: 123–131.

Magnus, B., S. Asplund, and L. Månsson. 2008. "VGC analysis: Application of the ROC methodology to visual grading tasks." *Proceedings of SPIE.*

Månsson, L.G. 2000. "Methods for the evaluation of image quality: a review." *Radiation Protection Dosimetry* 90: 89–99.

MathWorks. 2016. "MATLAB 2016a."

Mellor, M., and M. Brady. 2005. "(2005). Fluid Registration of Ultrasound using Multi-scale Phase Estimates. 10.5244/C.19.86." *Proceedings of the British Machine Vision Conference.* Oxford, UK.

Mercier, L., D. Araujo, Haegelen C., R.F. Del Maestro, K. Petrecca, and D.L. Collins. 2013. "Registering Pre- and Postresection 3-Dimensional Ultrasound for Improved Visualization of Residual Brain Tumor." *Ultrasound in Medicine & Biology* 39: 16-29.

Meyer, C.R., J.L. Boes, B. Kim, P.H. Bland, K.R. Zasadny, P.V. Kison, K. Koral, K.A. Frey, and R.L. Wahl. 1997. "Demonstration of accuracy and clinical versatility of mutual information for automatic multimodality image fusion using affine and thin-plate spline warped geometric deformations." *Medical Image Analysis* 1: 195–206.

Michailovich, O., and D. Adam. 2005. "A novel approach to the 2-d blind deconvolution problem in medical ultrasound." *IEEE Transactions on Medical Imaging* 24-1: 86–104.

Michailovich, O., and D., Adam. 2004. "Phase unwrapping for 2-D blind deconvolution of ultrasound images." *IEEE Transanctions on Medical Imaging* 23: 7–25.

Michailovich, O., and Tannenbaum. 2007. "A Blind deconvolution of medical ultrasound images: a parametric inverse filtering approach." *IEEE Transactions on Image Processing* 16-12: 3005–3019.

MITK. 2019. *Deutsches Krebsforschungszentrum.* 02 02. Accessed 05 01, 2019. http://www.mitk.org/wiki/The_Medical_Imaging_Interaction_Toolkit_(MITK).

Morin, R., A. Basarab, M. Ploquin, and D. Kouamé. 2012. "Alternating direction method of multipliers framework for super-resolution in ultrasound imaging." *9th IEEE International Symposium on Biomedical Imaging (ISBI).* 1595-1598.

Morin, R., A. Basarab, S. Bidon, and D. Kouamé. 2015. "Motion estimation-based image enhancement in ultrasound imaging." *Ultrasonics* 60: 19-26.

Morin, R., S. Bidon, A. Basarab, and D. Kouamé. 2013. "Semi-blind deconvolution for resolution enhancement in ultrasound imaging." *20th IEEE International Conference on Image Processing (ICIP).* 1413-1417.

Nakagami, N. 1960. "The m-distribution, a general formula for intensity distribution of rapid fadings." By W.G. Hoffman. Oxford: Pergamon.

Nakagami, N. 1960. "The m-distribution, a general formula for intensity distribution of rapid fadings." Edited by W.G. Hoffman. *Statistical Methods in Radio Wave Propagation* (Pergamon.) 47. doi:10.1016/B978-0-08-009306-2.50005-4.

Nandi, D., and S. Mukhopadhyay. 2011. "Performance of the SR algorithm for scan lined embedded in noise." *International Journal of Biomedical Engineering and Consumer Health Informatics* 3: 61-71.

Nandi, D., and S. Mukhopadhyay. 2011. "Super-resolution on Data Acquired in Polar Format." *International Journal of Biomedical Engineering and Consumer Health Informatics* 4: 63-73.

Ni, D., Y.P. Chui, X. Yang, J. Qin, T.T. Wong, S.S. Ho, and P.A. Heng. 2009. "Reconstruction of volumetric ultrasound panorama based on improved 3D SIFT." *Computerized Medical Imaging and Graphics* 33: 559-566.

Ni, D., Y.P. Chui, X. Yang, J. Qin, T.T. Wong, S.S. Ho, and P.A. Heng. 2009. "Reconstruction of volumetric ultrasound panorama based on improved 3D SIFT." *Computerized Medical Imaging and Graphics* 33: 559-566.

O'Donnel, M. 1999. "Class Notes - University of Michigan."

O'Reilly, M.A., and K. Hynynen. 2013. "A super-resolution ultrasound method for brain vascular mapping." *Medical Physics* 40: 110701.

Papoulis, A. 1975. "A new algorithm in spectral analysis and band-limited extrapolation." *IEEE Transactions on Circuits and Systems* 22: 735– 742.

Papoulis, A. 2002. "Probability, Random Variables, and Stochastic Processes." New York: McGrawHill.

Parker, K.J. 2012. "Superresolution imaging of scatterers in ultrasound B-scan imaging." *Journal of Acoustical Society of America* 131: 4680-4689.

Pennec, X., P. Cachier, and N. Ayache. 1999. "Understanding the "Demon's Algorithm": 3D Non-rigid Registration by Gradient Descent." *Medical Image Computing and Computer-Assisted Intervention – MICCAI'99: Second International Conference, September 19-22.* Cambridge, UK. 597-605.

Perona, P., and J. Malik. 1990. "Scale-space and edge detection using anisotropic diffusion." *IEEE Transactions on Pattern Analysis and Machine Intelligence* 12: 629–639.

Pham, T.Q., L.J. Van Vliet, and K. Schutte. 2006. "Robust fusion of irregularly sampled data using adaptive normalized convolution." *EURASIP Journal on Applied Signal Processing.* 1-12.

Pham, T.Q., L.J. Van Vliet, and K. Schutte. 2006. "Robust fusion of irregularly sampled data using adaptive normalized convolution." *EURASIP Journal on Applied Signal Processing* 1-12.

Pižurica, A., W. Philips, I. Lemahieu, and M. Achero. 2003. "A Versatile Wavelet Domain Noise Filtration Technique for Medical Imaging." *IEEE Transactions on Medical Imaging* 22: 323-331.

Rivaz, H., E.M. Boctor, G. Fichtinger, and G. (The Johns Hopkins University) Hager. 2008. Robust and accurate freehand 3D ultrasound. US Patent 8559685 B2. 08 21.

Rohling, R.N., A.H. Gee, and L. Berman. 1998. "Automatic registration of 3-d ultrasound images." *Ultrasound in Medicine & Biology* 24: 841-854.

Rue, H., and L. Held. 2005. *Gaussian Markov random fields: theory and applications.* Boca Raton: CRC Press.

Schneider, R.J., D.P. Perrin, N.V. Vasilyev, G.R. Marx, P.J. Del Nido, and R.D. Howe. 2012. "Real-time image-based rigid registration of three-dimensional ultrasound." *Medical Image Analysis* 16: 402-414.

Şener, E., Ü.E. Mumcuoğlu, and S. Hamcan. 2016. "Bayesian segmentation of human facial tissue using 3D MR-CT information fusion, resolution enhancement and partial volume modelling." *Computational Methods and Programs In Biomedicine* 124: 31–44.

Shekhar, R., and V. Zagrodsky. 2002. "Mutual information-based rigid and nonrigid registration of ultrasound volumes." *IEEE Transactions on Medical Imaging* 21: 9-22.

Shekhar, R., and V. Zagrodsky. 2002. "Mutual information-based rigid and nonrigid registration of ultrasound volumes." *IEEE Transactions on Medical Imaging* 21: 9-22.

Shin, J., Y. Chen, H. Malhi, F. Chen, and J. Yen. 2018. "Performance Evaluation of Adaptive Imaging Based on Multiphase Apodization with Cross-correlation: A Pilot Study in Abdominal Ultrasound." *Ultrasonic Imaging.*

Shung, K., M.B. Smith, and B.M.W. Tsui. 1992. *Principles of Medical Imaging.* San Diego, California: Academic Press.

Soergel, U. 2010. *Radar Remote Sensing of Urban Areas. Remote Sensing and Digital Image Processing.* Springer Science & Business Media.

Solberg, O.V., Lindseth F., L.E. Bø, S. Muller, J.B. Bakeng, G.A. Tangen, and T.A. Hernes. 2011. "3D ultrasound reconstruction algorithms from analog and digital data." *Ultrasonics* 51: 405-419.

Sudarshan, V.K., M.R. Mookiah, U.R. Acharya, V. Chandran, F. Molinari, and H. Fujita. 2016. "Application of wavelet techniques for cancer diagnosis using ultrasound images: A Review." *Computers in Biology and Medicine* 69: 97-111.

Szabo, T.L. 2004. *Diagnostic ultrasound imaging: Inside out.* 1. London: Elsevier Academic Press.

Taxt, T., and R. Jirik. 2004. "Superresolution of ultrasound images using the first and second harmonic signal." *IEEE Transactions on Ultrasonics, Ferroelectrics, and Frequency Control* 51: 163 -175.

Tay, P.C., C.D. Garson, S.T. Acton, and J.A. Hossack. 2010. "Ultrasound Despeckling for Contrast Enhancement." *IEEE Transactions on Image Processing* 1847-60.

Thirion, J.-P. 1998. "Image matching as a diffusion process: An analogy with Maxwell's demons." *Medical Image Analysis* 243–260.

Tilley II, S., H.J. Siewerdsen, and J.W. Stayman. 2015. "Model-based Iterative Reconstruction for Flat-Panel Cone-Beam CT with Focal Spot Blur, Detector Blur, and Correlated Noise." *Physics in medicine and biology* 61: 296-319.

Tinberg, A. 2000. "Quantifying the quality of medical x-ray images. An evaluation based on normal anatomy for lumbar spine and chest radiography." *PhD Thesis.*

Tomasi, C., and R. Manduchi. 1998. "Bilateral filtering for gray and color images." *In Proceedings of 6th International Conference on Computer Vision (ICCV '98).* Bombay. 839–846.

Toonkum, P., N.C. Suwanwela, and C. Chinrungrueng. 2011. "Reconstruction of 3D ultrasound images based on Cyclic Regularized Savitzky-Golay filters." *Ultrasonics* 51: 136-147.

Treece, G.M., R.W. Prager, A.H. Gee, and L. Berman. 2002. "Correction of probe pressure artifacts in freehand 3D ultrasound." *Medical Image Analysis* 6: 199-214.

Tsakalakis, M. n.d. "2015." *PhD Thesis, Design of a novel low-cost portable, 3D Ultrasound System with extended imaging capabilities for point-of-care applications.*

Tsuzurugi, J., and M. Okada. 2002. "Bayesian image restoration under spatially correlated noise-statistical-mechanical approach." *Proceedings of the 9th International Conference on Neural Information Processing, ICONIP '02.* 2419- 2423. doi:10.1109/ICONIP.200.

Tuthill, T.A., R.H. Sperry, and K.J. Parker. 1988. "Deviations from Rayleigh statistics in ultrasonic speckle." *Ultrasonic Imaging* 81-89.

Üstüner, K.F., and Holley G.L. 2003. "Ultrasound Imaging System Performance Assessment." *AAPM Annual Meeting.* August.

Vandewalle, P., S. Susstrunk, and M. Vetterli. 2006. "A frequency domain approach to registration of aliased images with application to super-resolution." *Journal of Applied Signal Processing* 2006: 1-14.

Vanithamani, R., and G. Umamaheswari. 2014. "Speckle reduction in ultrasound images using Neighshrink and bilateral filtering." *Journal of Computer Science* 10: 623- 631. doi:10.3844/jcssp.2014.623.631.

Vercauteren, T., X. Pennec, A. Perchant, and N. Ayache. 2009. "Diffeomorphic Demons: Efficient Non-parametric Image Registration." *NeuroImage* 45 (1): 61-72.

Wagner, R.F., W.S. Stephen, J.M. Sandrik, and H. Lopez. 1983. "Statistics of speckle in ultrasound B-scans." *IEEE Transactions on Sonics and Ultrasonics* 30: 156-163.

Wang, B., T. Cao, Y. Dai, and D.C. Liu. 2009. "Ultrasound speckle reduction via super resolution and nonlinear diffusion." *Computer vision – ACCV.* 130-139.

Wang, B., T. Cao, Y. Dai, and Liu D.C. 2010. "Ultrasound Speckle Reduction via Super Resolution and Nonlinear Diffusion." *Computer Vision – ACCV 2009, Volume 5996 of the series Lecture Notes in Computer Science.* 130-139.

Wolf, I., M. Vetter, I. Wegner, T. Bottger, M. Nolden, M. Schobinger, M. Hastenteufel, T. Kunert, and H.P. Meinzer. 2005. "The medical imaging interaction toolkit." *Medical Image Analysis* 9: 594-604.

Wu, G., J. Zhang, and R. Gonzalez. 2005. "Decision under risk." In *Blackwell Handbook of Judgment and Decision Making*, edited by D Koehler and N Harvey, 299-423. London: Wiley-Blackwell.

Wu, M.J., J. Karls, S. Duenwald-Kuehl, Jr. R. Vanderby, and W. Sethares. 2014. "Spatial and frequency-based super-resolution of ultrasound images." *Computer Methods in Biomechanics and Biomedical Engineering: Imaging & Visualization* 2: 146- 156.

Yang, Z., S.P. Sinha, R.C. Booi, M.A. Roubidoux, B. Ma, and J.B. Fowlkes. 2009. "Breast Ultrasound Image Improvement By Pixel Compounding of Compression Sequence." *IEEE Transactions on Ultrasonics, Ferroelectrics, and Frequency* 56: 465-473.

Yang, Z., T.A. Tuthill, D.L. Raunig, and M.D. Fox. 2007. "Pixel compounding: resolution-enhanced ultrasound imaging for quantitative analysis." *Ultrasound in Medicine & Biology* 33: 1309-1319.

Yoon, C., G.D. Kim, Y. Yoo, T.K. Song, and J.H. Chang. 2013. "Frequency equalized compounding for effective speckle reduction in medical ultrasound imaging." *Biomedical Signal Processing and Control* 8: 876–887.

Yoshikawa, H., T. Azuma, and T. Hayashi. 2006. Ultrasonic diagnostic apparatus",. US Patent 20090306505 A1.

Youla, D.C. 1978. "Generalized image restoration by the method of alternating orthogonal projections." *IEEE Transactions on Circuits Systems* 25: 694-702.

Zerhouni, M.B., and M. Rachedine. 1990. Ultrasonic calibration material and method. US Patent US5196343A.

Zhao, N., A. Basarab, D. Kouamé, and J-Y. Tourneret. 2016. "Joint segmentation and deconvolution of ultrasound images using a hierarchical." *IEEE Transactions on Image Processing* 25-8: 3736-3750.

Zheng, J., J.A. Fessler, and H.P. Chan. 2018. "Detector Blur and Correlated Noise Modeling for Digital Breast Tomosynthesis Reconstruction,." *IEEE Transactions on Medical Imaging* 37: 116-127.

Zomet, A., A. Rav-Acha, and S. Peleg. 2001. "Robust super-resolution." *in Proceeding of the Int.Conf. on CVPR.* 645-650.

APPENDICES

APPENDIX A

QUESTIONS & RADIOLOGIST SCORES
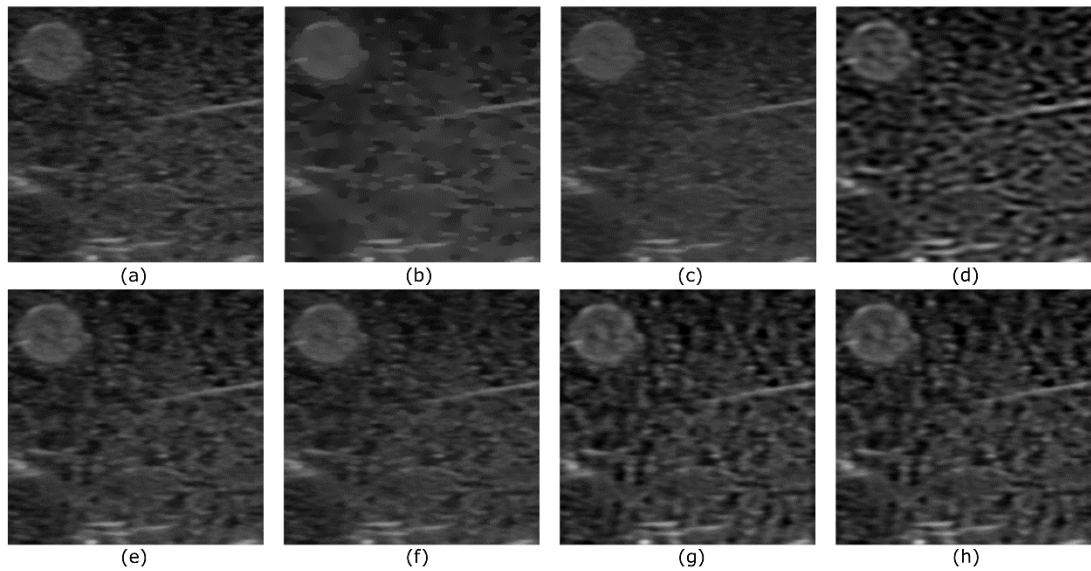
Case 1 - Breast Phantom Hyperechoic Target

Figure 48: Case 1 - Restoration results of breast phantom hyperechoic target, using the parameters in Table-4 (HR image size: 400x400 pixels) (a) Observed image; Restoration results of (b) AD; (c) BF; (d) WF; (e) BR-UG; (f) BR-CG; (g) BSRR-UG; (h) BSRR-CG.

Case 1 - Question 1

Eng: How do you score the amount of improvement in granular coarsening?
Tr: Granüler kabalaşma ne ölçüde belirginleşmiştir?

Average Scores:

AD	BF	WF	BR-UG	BR-CG	BSRR-UG	BSRR-CG
-0.8	-0.4	0.8	0.4	0.8	**1.4**	1.0

Case 1 - Question 2:

Eng: How do you score the amount of increase in sharpening of the nodule contour?
Tr: Nodül kontur keskinliği ne ölçüde belirginleşmiştir?"

Average Scores:

AD	BF	WF	BR-UG	BR-CG	BSRR-UG	BSRR-CG
0.2	**0.6**	0.0	-0.4	0.2	**0.6**	-0.2

Case 2 - Human Thyroid

This case is presented in section 3.3.
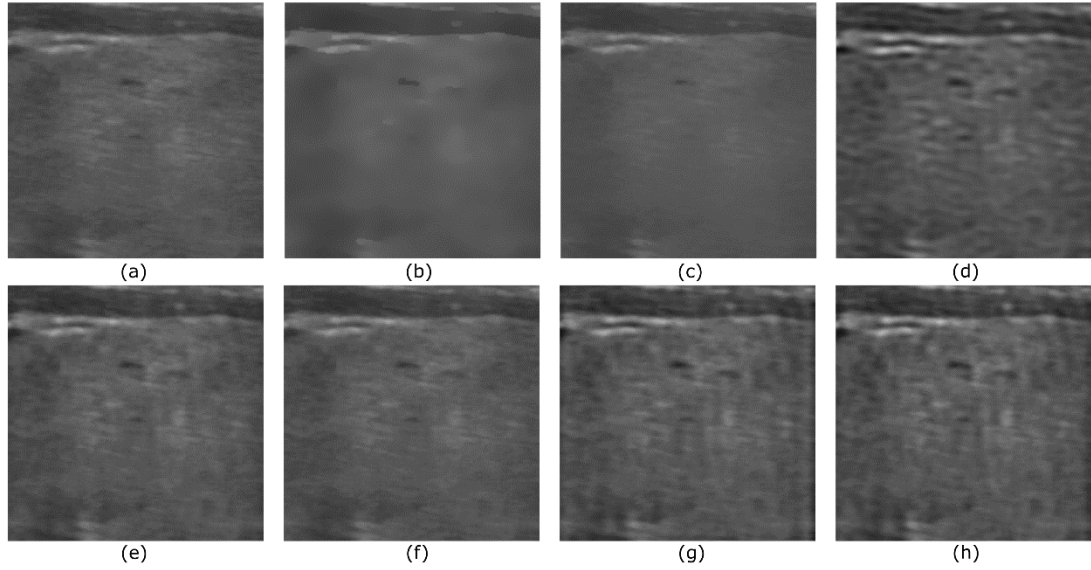
Case 3 – Human Thyroid

Figure 49: Case 3 - Restoration results of human thyroid image, using the parameters in Table-4 (HR image size: 400x400 pixels) (a) Observed image; Restoration results of (b) AD; (c) BF; (d) WF; (e) BR-UG; (f) BR-CG; (g) BSRR-UG; (h) BSRR-CG.

Case 3 - Question 1:

Eng: How do you score the amount of improvement in granular coarsening?
Tr: Granüler kabalaşma ne ölçüde belirginleşmiştir?

Average Scores:

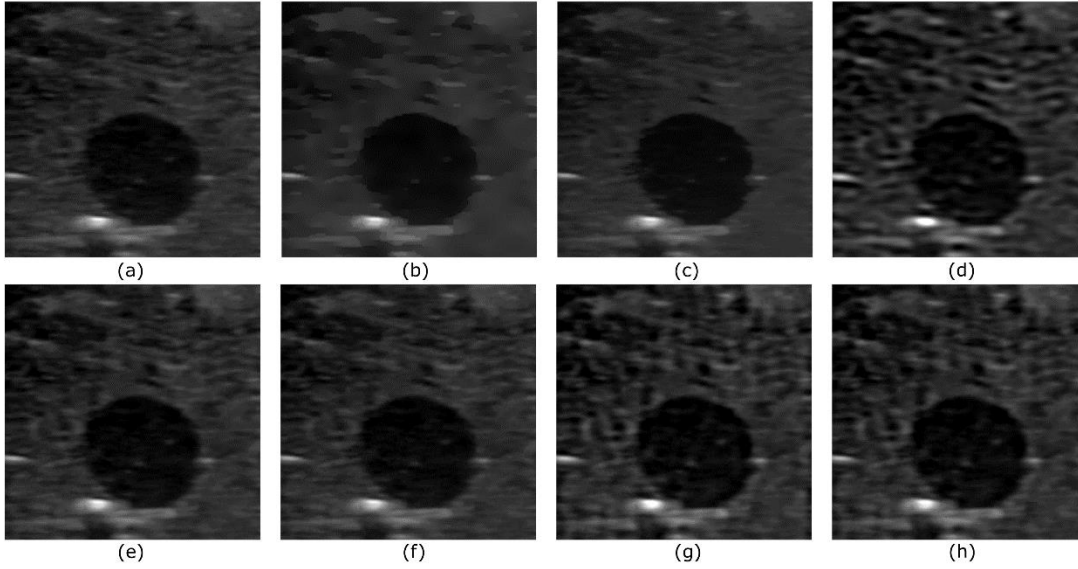| AD	BF	WF	BR-UG	BR-CG	BSRR-UG	BSRR-CG
-1.2	-1.2	0.6	0.4	0.4	**1.2**	0.6

Case 4 – Breast Phantom Hypoechoic Target

Figure 50: Case 4 - Restoration results of breast phantom hyperechoic target, using the parameters in Table-4 (HR image size: 400x400 pixels) (a) Observed image; Restoration results of (b) AD; (c) BF; (d) WF; (e) BR-UG; (f) BR-CG; (g) BSRR-UG; (h) BSRR-CG.

Case 4 - Question 1:

Eng: How do you score the amount of improvement of the clarity of the cyst?
Tr: Kist ne ölçüde belirginleşmiştir?

Average Scores:

AD	BF	WF	BR-UG	BR-CG	BSRR-UG	BSRR-CG
-0.4	0.6	0.6	0.0	0.2	0.2	**0.8**

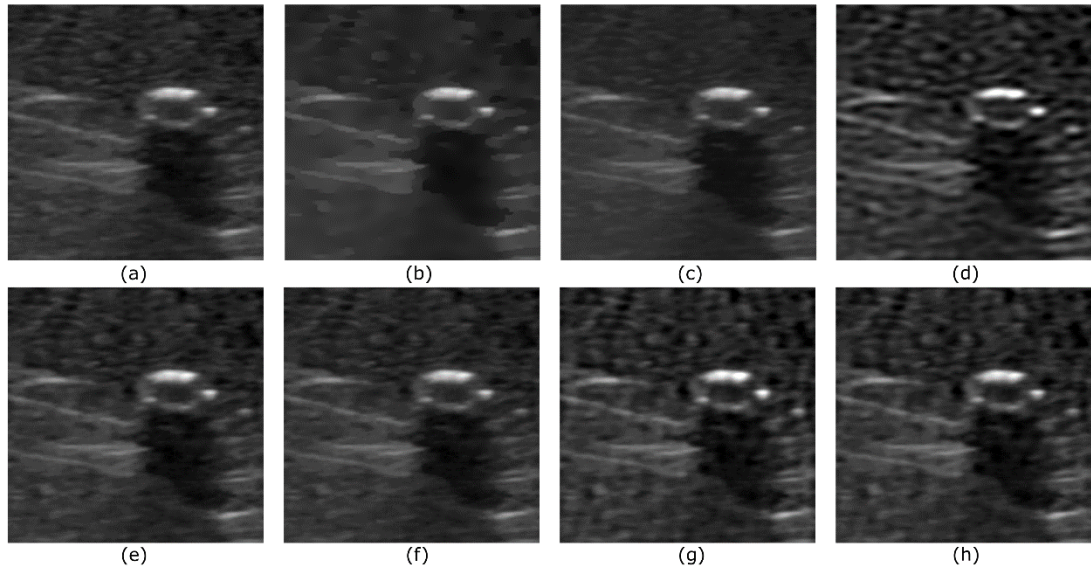**Case 5 – Breast Phantom Microcalcifications**

Figure 51: Case 5 - Restoration results of breast phantom microcalcification, using the parameters in Table-4 (HR image size: 400x400 pixels) (a) Observed image; Restoration results of (b) AD; (c) BF; (d) WF; (e) BR-UG; (f) BR-CG; (g) BSRR-UG; (h) BSRR-CG.

Case 5 - Question 1:

Eng: How do you score the amount of improvement in observability of the microcalcifications?
Tr: Mikrokalsifikasyonların gözlemlenebilirliği ne kadar artmıştır?

Average Scores:

AD	BF	WF	BR-UG	BR-CG	BSRR-UG	BSRR-CG
0.0	0.4	0.8	0.4	0.2	**1.2**	0.8

Case 6 – Human Lymph Nodule

This case is presented in section 3.3.

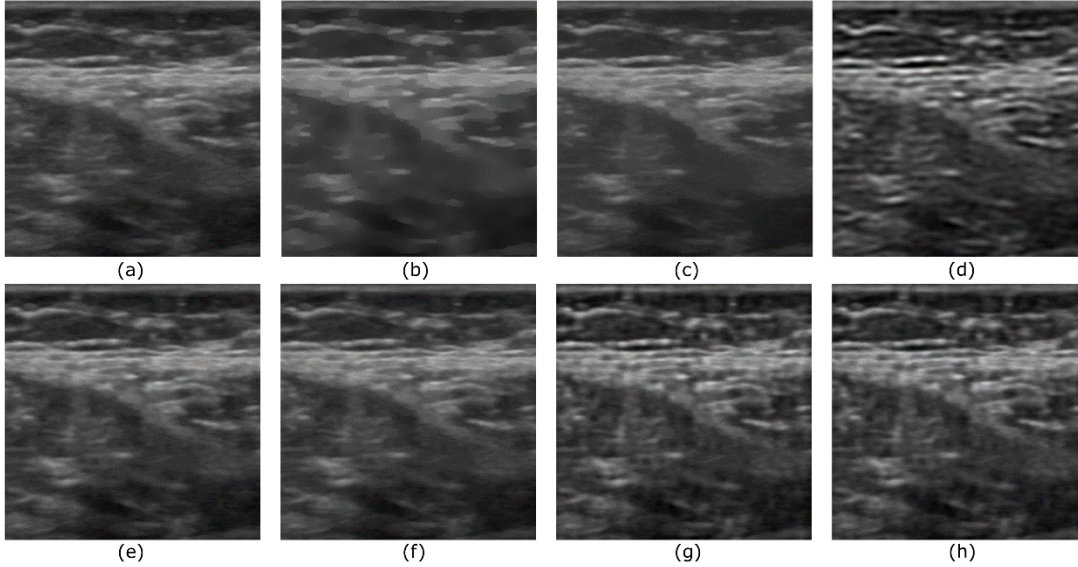## Case 7 – Human Submandibular Gland

Figure 52: Case 7 - Restoration results of human submandibular gland (volunteer with systemic lupus erythematosus), using the parameters in Table-4 (HR image size: 510x510 pixels) (a) Observed image; Restoration results of (b) AD; (c) BF; (d) WF; (e) BR-UG; (f) BR-CG; (g) BSRR-UG; (h) BSRR-CG.

Case 7 - Question 1:

Eng: How do you score the amount of increase in observability of heterogeneity in submandibular gland?
Tr: Submandibular bezdeki heterojenite gözlemlenebilirliği ne kadar artmıştır?

Average Scores:

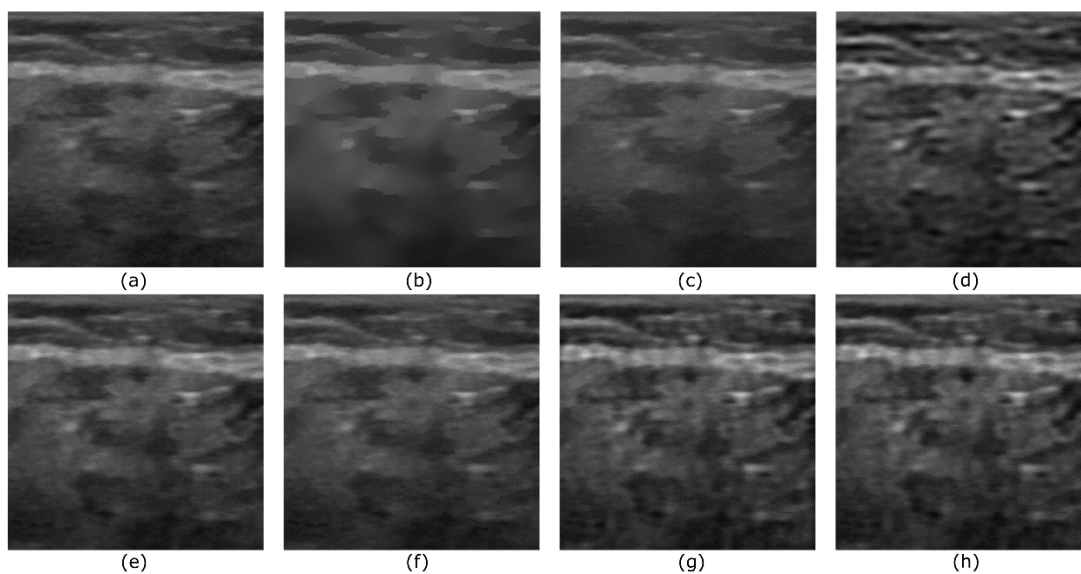| AD	BF	WF	BR-UG	BR-CG	BSRR-UG	BSRR-CG
-1.2	-0.4	0.0	**1.2**	0.8	0.8	**1.2**

Case 8 – Human Parotis Gland

Figure 53: Case 8 – Restoration results of human parotis gland (volunteer with systemic lupus erythematosus), using the parameters in Table-4 (HR image size: 400x400 pixels) (a) Observed image; Restoration results of (b) AD; (c) BF; (d) WF; € BR-UG; (f) BR-CG; (g) BSRR-UG; (h) BSRR-CG.

Case 8 – Question 1:

Eng: How do you score the amount of increase in observability of heterogeneity in parotis gland?
Tr: Parotis bezindeki heterojenite gözlemlenebilirliği ne kadar artmıştır?

Average Scores:

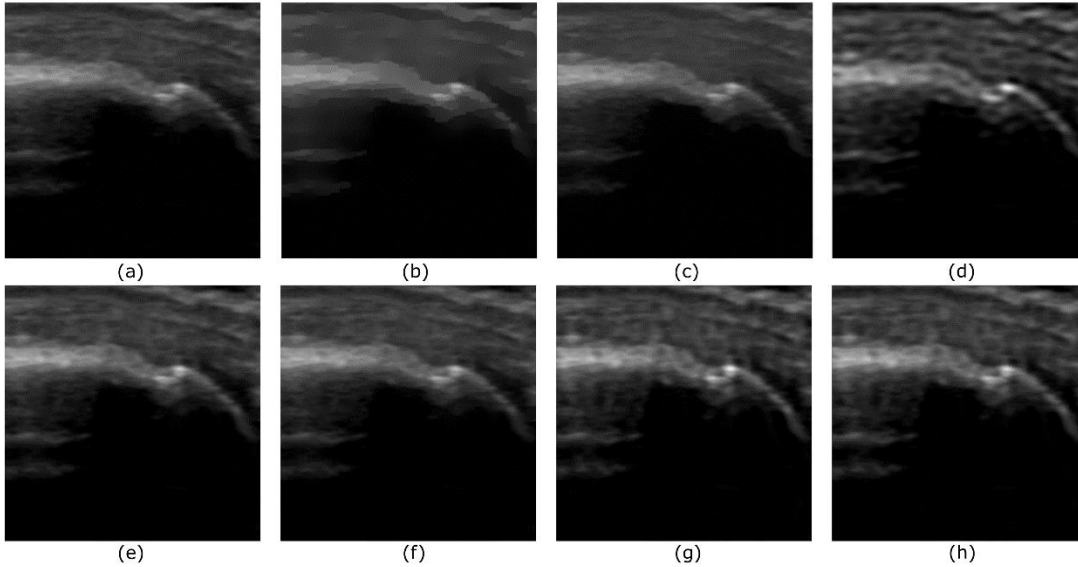| AD	BF	WF	BR-UG	BR-CG	BSRR-UG	BSRR-CG
-1.2	-0.2	-0.4	0.6	0.6	**1.0**	0.8

Case 9 – Human Hand Tendon

Figure 54: Case 9 - Restoration results of human healthy human tendon (hand), using the parameters in Table-4 (HR image size: 400x400 pixels) (a) Observed image; Restoration results of (b) AD; (c) BF; (d) WF; (e) BR-UG; (f) BR-CG; (g) BSRR-UG; (h) BSRR-CG.

Case 9 – Question 1:

Eng: How do you score the amount of increase clarity of the tendon peripheral tissue transition?
Tr: Tendon çevre doku geçişi ne ölçüde belirginleşmiştir?

Average Scores:

AD	BF	WF	BR-UG	BR-CG	BSRR-UG	BSRR-CG
-0.8	0.4	0.8	0.2	0.2	**1.2**	0.4

Case 9 – Question 2:

Eng: How do you score the amount of increase in homogeneity of the tendon?
Tr: Tendon homojenitesi ne ölçüde artmıştır?

Average Scores:

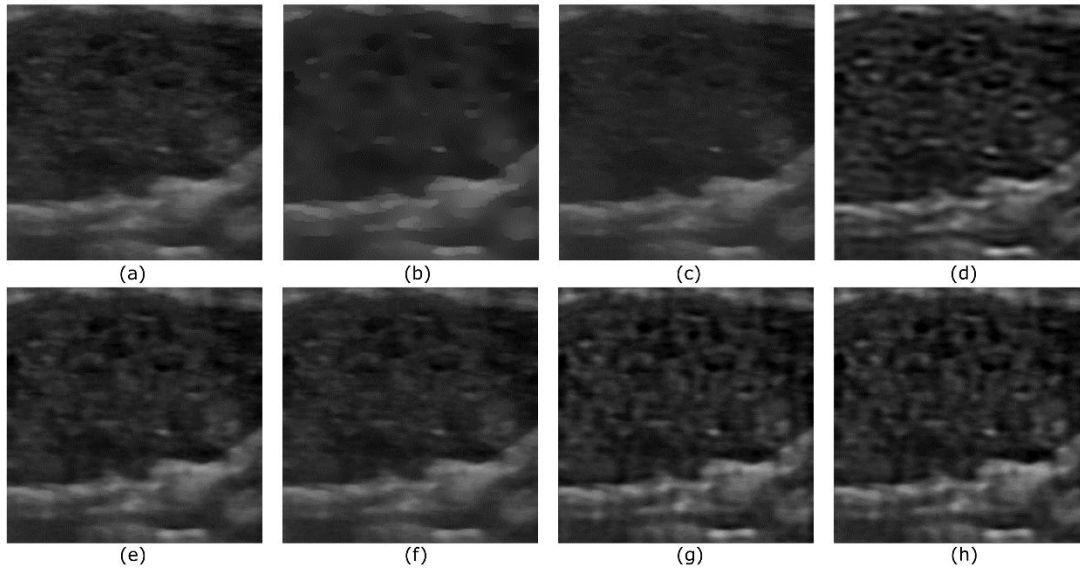| AD	BF	WF	BR-UG	BR-CG	BSRR-UG	BSRR-CG
-0.8	0.2	0.0	**0.4**	0.2	-0.2	0.0

Figure 55: Case 10 - Restoration results of human thyroid image, using the parameters in Table-4 (HR image size: 400x400 pixels) (a) Observed image; Restoration results of (b) AD; (c) BF; (d) WF; (e) BR-UG; (f) BR-CG; (g) BSRR-UG; (h) BSRR-CG.

Case 10 – Question 1:

Eng: How do you score the amount of improvement in granular coarsening?
Tr: Granüler kabalaşma ne ölçüde belirginleşmiştir?

Average Scores:

AD	BF	WF	BR-UG	BR-CG	BSRR-UG	BSRR-CG
-1.0	0.0	**1.2**	0.6	0.2	0.6	1.0

<div align="center">**CURRICULUM VITAE**</div>

PERSONAL INFORMATION

Surname, Name: Mine Cüneyitoğlu Özkul

Nationality: T.C.

Date and Place of Birth:

Marital Status: Married (1 Child)

Phone: 90 312 427 06 73 (118)

email: mine.cuneyitoglu@metu.edu.tr

EDUCATION

Degree	Institution	Year of Graduation
MS	METU Dept. of Mechanical Eng.	2012
BS	METU Dept. of Mechanical Eng.	2009
High School	İzmir Konak Anadolu Lisesi	2003

WORK EXPERIENCE

Year	Place	Enrollment
2018-Present	Teknolus Energy Ltd.	Systems Engineer & Project Manager
2017-2018	TÜBİTAK 1001 Project **116E570** - *Sosyal Gözbakışı İçin Çoklu Gözizleme Platformu (METU Informatics Institute, Dept. of Cognitive Science - Yrd. Doç. Dr. Cengiz Acartürk)*	Scholarship Student: Software Development

2013-2016	TÜBİTAK Öncelikli Alanlar Bursu	Scholarship Student: PhD. Thesis Studies
2010-2012	ROKETSAN A.Ş.	Embedded Systems Software Engineering, Software Development on Real Time Operating Systems
2009-2012	TÜBİTAK 1001 Project **110E120** - *Kıvrak Bacaklı Robotlarda Gürbüz Görsel Algının Işitsel Algı Desteğinde Geliştirilmesi Ve Otonom Navigasyon Amaçlı Uygulanması (METU Dept. of Electrical and Electronics Engineering - Assoc. Dr. Afşar Saranlı)*	Scholarship Student: Mechanical Design Tasks, Ms Thesis on Acoustic Signal Processing *(Supervisor: Assoc. Dr. Yiğit Yazıcıoğlu - METU Dept. of Mechanical Engineering, Co-Supervisor: Assoc. Dr. Afşar Saranlı, METU Dept. of Electrical and Electronics Engineering)*
2009-2010	METU Dept. of Mechanical Engineering	Teaching and Research Assistant
2009	TÜBİTAK 1001 Project **105K127** - *Çok Maksatlı Ulusal İnsansız Sualtı Aracı Projesi (METU Dept. of Electrical and Electronics Engineering – Prof. Dr. Kemal Leblebicioğlu)*	Scholarship Student: Mechanical Design Tasks

FOREIGN LANGUAGES

Native Turkish, Advanced English (YDS - 90)